THE INFLUENCE OF THERMAL EFFECTS ON STRUCTURAL HEALTH MONITORING OF ATTRIDGE DRIVE OVERPASS

A Thesis

Submitted to the College of Graduate Studies and Research

in Partial Fulfillment of the Requirements

for the Degree of Master of Science

in the Department of Civil Engineering

University of Saskatchewan

Saskatoon, Canada

By

Tuan Pham

PERMISSION TO USE

In presenting this thesis in partial fulfillment of the requirements for a postgraduate degree from the University of Saskatchewan, I agree that the libraries of this University may make it freely available for inspection. I further agree that permission for copying of this thesis in any manner, in whole or in part, for scholarly purposes may be granted by the professor or professors who supervised my thesis work or, in their absence, by the Head of the Department or the Dean of the College in which my thesis work was done. It is understood that any copying or publication or use of this thesis or parts thereof for financial gain shall not be allowed without my written permission. It is also understood that due recognition shall be given to me and to the University of Saskatchewan in any use which may be made of any material in my thesis.

Requests for permission to copy or to make other uses of materials in this thesis in whole or part should be addressed to:

Head of the Department of Civil Engineering
University of Saskatchewan
Engineering Building
57 Campus Drive
Saskatoon, Saskatchewan, Canada
S7N 5A9

ABSTRACT

Structural Health Monitoring (SHM) comprises a wide range of techniques for the condition and damage assessment of an existing structure. Vibration-based damage detection (VBDD) techniques, a class of SHM methods, use changes in the dynamic properties (i.e., natural frequencies, mode shapes and damping characteristics) of structures to detect deterioration or damage. The application of VBDD methods to simple structures in a well-controlled laboratory environment has gained some successful results. However, the practical field application of VBDD still faces significant challenges since vibration measurement is subject to the influences of high levels of uncertainty in environmental, structural and loading conditions. In this thesis, the influence of temperature variations on the application of VBDD methods to an in-service complex structure was experimentally and numerically studied. The structure studied was the Attridge Drive overpass in Saskatoon, Saskatchewan.

The main objective of this research was to assess the influence of temperature variation on the dynamic properties (natural frequencies and mode shapes) of the overpass, and on the ability of VBDD methods to detect and locate damage. Field dynamic measurements were made on the bridge on numerous occasions under a wide variety of ambient temperatures, using high sensitivity accelerometers and a temperature sensor. Dynamic excitation was provided solely by ambient traffic loading.

Finite element models of the overpass were also created and manually calibrated to measured field data. The models were used to simulate the dynamic behaviour of the bridge at a variety of temperatures and under various states of small-scale damage. Numerical analysis was conducted to study the effect of ambient temperature on structure's dynamic characteristics and to differentiate the patterns of mode shape changes caused by damage and ambient temperature.

It was concluded that the change of ambient temperature mainly affects the elastic modulus of the construction materials and therefore stiffness of the entire bridge. As a result, the eigenfrequencies and mode shapes of the structure are influenced.

The dynamic properties extracted from measured experiment data showed an approximately bilinear relationship between the three first natural frequencies and the ambient temperature. The natural frequencies for all three modes increased when the temperature fell.

It was also found that, conceptually, it is possible to distinguish the patterns of mode shape changes caused by small-scale damage from those due to thermal effects, but only if a sufficient number of sensors are used to measure the mode shapes; in addition, those sensors must be located close to the damage location.

ACKNOWLEDGEMENTS

I would like to take this opportunity to express my sincere thanks and gratitude to my supervisors, Dr. Bruce Sparling and Dr. Leon Wegner for their assistance, guidance and words of encouragement during the formation of this thesis.

I am grateful for the funding provided by Saskatchewan Highways and Transportation, and the Intelligent Sensing for Innovative Structures Canada Research Network (ISIS).

I would like to extend my gratitude to my committee members, Drs. Mohamed Boulfiza, Lisa Feldman, Gordon Putz, and external examiner Mr James Johnston for their comments and advice during the research program.

I would like to express my thanks to Dale Pavier, Brennan Pokoyoway for their instruction and assistance in the completion of the field testing program. The generous assistance of departmental staff and fellow graduate students is acknowledged.

Lastly, I would like to take this opportunity to thank my family and my wife Linh Nguyen, who provided much support and encouragement throughout the course of this project.

TABLE OF CONTENTS

LIST OF TABLES

LIST OF FIGURES

LIST OF SYMBOLS

E	=	Modulus of elasticity
$\mathbf{F}$	=	Flexibility matrix
$\mathbf{F}^*$	=	Flexibility matrix of a structure in damage state
f	=	Uniform load flexibility
f''	=	Uniform load flexibility curvature
$f_c^{'}$	=	Compressive strength of concrete
G	=	Modulus of rigidity
gradT	=	Temperature gradient through the height or width of the cross section
[k]	=	System stiffness matrix
[m]	=	System mass matrix
n_i	=	Size of sample *i*
s_i	=	Standard deviations of the sample *i*
$s_{\bar{x}_1-\bar{x}_2}$	=	Standard error of the difference between mean values of the two samples
T_0	=	The mean temperature of the structure
$\bar{x}_i$	=	Mean values of sample *i*
Z_j	=	Normalized damage index
α	=	Coefficient of thermal expansion of material
β_j	=	Damage index at j^{th} node for multiple modes
β_{ji}	=	Damage index at the location of j^{th} node for i^{th} mode shape
γ_c	=	Density of concrete
$\overline{\delta_j}$	=	Maximum absolute value of a column of change in flexibility matrix
Δf	=	Change in frequency
μ_β	=	Mean value of damage indices
ν	=	Number of degrees of freedom
ρ	=	Density of material

σ_β	=	Standard deviation of damage indices
υ	=	Poisson's ratio of material
$\boldsymbol{\phi}_i$	=	i^{th} vibration mode shape vector
$\boldsymbol{\phi}_i^*$	=	i^{th} vibration mode shape vector of damaged induced structure
ϕ''_{ji}	=	curvature at point j corresponding to the i^{th} mode
ϕ_{ji}	=	Modal amplitude at point j to the i^{th} mode.
$\Phi(t,\nu)$	=	Standard normal cumulative distribution
$\boldsymbol{\phi}_{Ti}$	=	Mode shape vector for a given temperature range
$\boldsymbol{\phi}_{T0}$	=	Mode shape vector for the temperature range of 20°C to 26°C
ω	=	Angular natural frequency

LIST OF ABBREVIATIONS

ADINA	Automatic Dynamic Incremental Nonlinear Analysis: A finite element software
ASCII	American Standard Code for Information Interchange
ARX	Auto-Regressive exogeneous model
Avg	Average
CSA	Canadian Standards Association
DC	Direct Current
DAQ	Data Acquisition
DOF	Degree of Freedom
FE	Finite Element
FFT	Fast Fourier Transform
FORTRAN	Formula Translation (computer language)
FRF	Frequency Response Function
LabView	Laboratory Virtual Instrumentation Engineering Workbench
MAC	Modal Assurance Criterion
MAX	Measurement and Automation Explorer
NI	National Instruments
PCMCIA	Peripheral Component Microchannel Interconnect Architecture
RMS	Root Mean Square
SD	Standard Deviation
SHM	Structural Health Monitoring
VBDD	Vibration-based Damage Detection

CHAPTER 1 . INTRODUCTION

1.1 BACKGROUND

There is an increasing need to keep the existing bridge infrastructure in service for a long period of time. At the same time, unexpected traffic volumes and heavy vehicles, gradually increasing fatigue effects, and environmental (storm, wind, temperature, ice, relative humidity, and exposure to salts and snow accumulation, etc.) and accidental (vessel collisions and traffic accidents, earth quakes) conditions continuously accumulate damage in bridges during their service life. Therefore, the capability of existing bridges to perform in an acceptable manner presently, and in the future, is of primary concern. Regular inspection and condition assessment of existing bridges is necessary so that early detection of any defect can be made and the safety and reliability of the structure can be determined.

Current practices for assessing the condition of bridges include visual inspections and localized experimental methods. Visual inspection relies heavily on the inspector's experience and knowledge and is insufficient for assessing elements that are concealed or that cannot be reliably evaluated. Localized evaluation methods, such as acoustic emission, ultrasonic methods, magnetic field methods, radiographs, and eddy-current methods, require that the location of the damage be known in advance and that the portion of the structure being inspected is accessible (Farrar et al. 2001).

A promising alternative method for structural health monitoring (SHM) is vibration monitoring. Damage or fault detection determined by changes in the dynamic properties or response of structures is a subject that has received considerable attention in the literature. The basic idea is that modal parameters (eigenfrequencies, mode shapes and modal damping), which can be measured by vibration experiments in the field, are

functions of the physical properties of the structure (mass and stiffness). The occurrence of damage of a bridge leads to changes in the physical properties, and therefore causes changes in the modal properties. Using vibration-based methods, damage can be detected by measuring the global response even when the location of damage is inaccessible.

To date, vibration-based damage detection (VBDD) methods have been successfully applied to rotating machinery and well-defined mechanical and aerospace systems (Shives and Mertaugh 1986, Farrar and Duffey 1999). These methods have also been applied on bridge structures in recent years (Peeters and De Roeck 2000, Brownjohn 2003, Halling 2001). Although successful applications have been developed recently, the damage assessment of complex structures such as bridges remains a challenging task for structural engineers.

Previous studies carried out at the University of Saskatchewan have demonstrated that VBDD methods can be applied to detect and locate small-scale damage in relatively uncomplicated bridge structures. Research by Zhou et al. (2003) has demonstrated the successful implementation of VBDD methods for a slab-on-girder bridge deck and prestressed concrete girders in a controlled laboratory environment. In applying VBDD to a complex field structure - namely a bridge - Siddique et al. (2005) numerically showed the ability of VBDD methods to detect and locate various states of damage in an integral abutment bridge provided that some conditions related to the number and placement of sensors were satisfied.

There are many issues that are critical to the successful application of VBDD techniques to complex and real structures such as bridges under varying operational and environmental conditions. Among these factors is the influence of environmental temperature on the dynamic response of the bridge. A number of researchers have explored the influence of changing temperature on the natural frequencies of bridges (Loland and Dodds 1976, Cawley and Adams 1979, Salawu 1997 and Doebling et at. 1996). However, the effect of ambient temperature on mode shapes has not yet been studied thoroughly.

The special weather conditions of Saskatoon, Saskatchewan, with hot, dry summers and long hours of sunshine as well as sunny, windy and very cold winters, present a unique opportunity to evaluate the effect of ambient temperature on the mode shapes of a bridge. The research described in this thesis is the continuation of investigations at the University of Saskatchewan focused on applying VBDD to real and complex structures. This thesis presents and interprets the effects of ambient temperature on the dynamic properties of a bridge using field experiments and numerical analysis of the Attridge Drive Overpass located in Saskatoon, Saskatchewan.

1.2 OBJECTIVES

The primary objectives of the current study were:

- To determine how temperature variation influences the natural frequencies and mode shapes of the Attridge Drive overpass ; and
- To compare the changes to mode shapes caused by temperature variation to those caused by small-scale damage in an attempt to distinguish between the two.

Both of these objectives are intended to contribute toward efforts for the successful implementation of VBDD methods on large-scale civil engineering structures.

1.3 SCOPE

This study focused on the effect of ambient temperature on the application of VBDD to a full-scale bridge. The field data used in this study were obtained from vibration measurements on the Attridge Drive Overpass located in Saskatoon, Saskatchewan over a wide range of ambient temperatures. Measured properties were limited to the modal parameters of natural frequencies and mode shapes, calculated from measured accelerations. The effect of loading conditions on the application of VBDD was not studied.

The overpass was accurately represented by three-dimensional finite element (FE) models to simulate the dynamic behaviour. Due to the limited knowledge regarding foundation conditions, changes to foundation properties due to thermal cycling were not considered in the models.

The reliability or the uncertainty of vibration measurements for vibration-based damage detection techniques applied to field structures was not studied. This research project was not intended to compare or verify the data with that collected from other sites.

1.4 METHODOLOGY

The methodology used in this thesis included both field testing and numerical modelling components.

For the field testing component, the dynamic response of the Attridge Drive Overpass was measured repeatedly under a wide range of environmental conditions, using ambient traffic loading as the source of vibration. The dynamic properties obtained from the processed field data were then presented versus ambient temperature to determine the thermal effects on the dynamic properties of the bridge.

Revised versions of an existing FE model of the overpass, which were calibrated to field measurements to ensure that they were representative of the actual structure, were used to supplement the field testing program and extend the investigation beyond the conditions tested in the field. The response of the bridge under a variety of damage and temperature conditions was simulated to better understand the effect of these factors on the dynamic properties of the bridge and to try to differentiate the patterns of mode shape changes due to both factors.

1.5 THESIS LAYOUT

The thesis consists of seven chapters, plus references and appendices. A brief description of each chapter is given below.

Chapter 1 has introduced the main objectives of the thesis and presented background information.

Chapter 2 reviews the relevant literature related to structural health monitoring and vibration-based damage detection in general and provides a detailed review of the past research related to the influence of environmental effects, especially ambient temperature, on the application of VBDD. A discussion of some research regarding damage detection techniques is also provided.

Chapter 3 describes the collection of measurements from the Attridge Drive Overpass and their use to determine the changes to the bridge's dynamic characteristics due to temperature. The components of the data acquisition system used are discussed in this chapter, as well as the processing of the acquired data.

Chapter 4 describes the numerical study. It covers the numerical model correction and calibration, the simulation of damage scenarios in the model, the implementation of the five VBDD techniques, and the methods of comparing the dynamic properties of the bridge under different induced damage and temperature conditions.

The experimental results and discussion are presented in Chapter 5. The effects of temperature variation on the measured dynamic properties of the overpass structure, and the variability measured mode shape are discussed in this chapter.

Chapter 6 presents the results from finite element modelling. The findings regarding how the dynamic properties of the bridge change due to variation of ambient temperature are presented. Visual and quantitative comparisons of the damage induced mode shape changes and temperature induced mode shape changes are also presented.

Chapter 7 presents the conclusions of the study and recommendations for future research.

CHAPTER 2 . LITERATURE REVIEW

2.1 APPLICATION OF VIBRATION-BASED DAMAGE DETECTION TO BRIDGES

2.1.1 Overview

Structural Health Monitoring (SHM) refers to the gathering of information of a structure and using that information for assessing its condition. Techniques for SHM may be classified as global or local. Local methods concentrate on only a part of the structure and are based on acoustics, eddy currents, hardness testing, magnetic fields, radiography, X-rays, or any number of other specific techniques (Housner et al. 1997). The disadvantage of such techniques is that they can only find damage in a small vicinity; therefore, inspection of a large test object is costly and time consuming. Global methods make use of changes in the overall response of a structure as indicators of damage. In global methods, measurements at a limited number of locations may be sufficient to assess the condition of the whole structure even when the measurement locations differ from the location of the damage. Global methods can be intermittently applied using temporarily installed sensors or continuously applied with sensors permanently attached to the structure.

Most global SHM methods currently under investigation focus on the use of dynamic responses to detect and locate damage. These dynamics-based methods can be divided into two groups: time domain methods (Fugate et al. 2000, Masri et al. 1996, Kim et al. 2005), and frequency domain methods (Samman and Biswas 1994a). The approach used in this research, a frequency domain method, uses changes in natural frequencies and

mode shapes to detect damage. This approach is known as vibration-based damage detection (VBDD). With VBDD, it is possible to locate and detect damage because modal properties are directly related to the physical properties (mass, stiffness, damping) of the structure.

Based on their damage detecting capabilities, SHM methods in general, and VBDD techniques in particular, can be classified into four categories exhibiting different levels of damage detection, as follows (Rytter 1993):

(1) Identification that damage has occurred;

(2) Identification that damage has occurred and determination of the location of damage;

(3) Identification that damage has occurred, localization of the damage and estimation of its severity; and

(4) Identification that damage has occurred, localization of the damage, estimation of its severity and determination of the remaining useful life of the structure.

VBDD methods have been applied to bridge structures since the early 1980s (Salane et al. 1981, Kato and Shimada 1984). Lately, some successful applications of VBDD to bridge structures have shown the feasibility of detecting the presence and location of damage (Pandey and Biswas 1994, Wang et al. 1997, Maeck and De Roeck 1999); however, the study of Level 3 and 4 damage detection is less common.

A systematic research program studying the feasibility of applying VBDD methods to bridge structures was established at the University of Saskatchewan several years ago. In this research program, various aspects related to the application of VBDD methods to bridges have been examined considering issues of increasing complexity over time, beginning with simple numerical and laboratory experimental studies and moving into complex field structural measurements. These studies have focused on the use of VBDD methods to detect and locate small-scale damage using a limited number of sensors. This work is briefly summarized here, followed by a review of studies conducted elsewhere on the use of VBDD for bridge structures.

2.1.2 Research Conducted at the University of Saskatchewan

Zhou et al. (2003, 2007) conducted forced vibration tests using harmonic excitation on a half-scale laboratory model of a two-girder steel-free bridge deck, supplementing the experimental work with additional numerical studies. It was found that small-scale damage could be detected and located using only the first mode of vibration before and after damage, along with a small number of sensors positioned along each girder. The location of damage was able to be determined with a resolution of approximately 65% to 70% of measurement point spacing. This study also indicated the advantages of using forced harmonic vibration applied at a natural frequency over other excitation methods in terms of repeatability of mode shape measurements.

Results by Zhou et al. (2004) using forced vibration tests on a full-scale prestressed concrete box girder were similar to those mentioned above. The accuracy of the predicted longitudinal location of damage was strongly influenced by the spacing between sensors, the location of damage relative to sensors, and the distance between two damage states when close in proximity. The resolution of damage localization was observed to decline when multiple damage sites were present and when damage was located near a support.

Extending the program to full-scale field structures, Siddique et al. (2005, 2006, 2007) conducted ambient vibration tests on a two span continuous composite (concrete deck on steel-girders) integral abutment bridge. A finite element model was developed to simulate the dynamic response of the structure in undamaged and damaged conditions. The numerical study showed that VBDD methods could be used to detect and locate damage on the bridge deck with a high degree of confidence, provided that a sufficient number of sensors were used to measure the mode shapes and that the sensors were located close to the damage location. It was also found that unless a large number (up to 500) of repeated vibration trials using random loading patterns were used, the changes in fundamental mode shape resulting from the damage were completely masked by the measurement uncertainty.

Alwash et al. (2005, 2006, and 2009) found that the quality of modal properties extracted from the dynamic response of a bridge depended to a large extent on the

characteristics of the force-time history of the excitation. The research was conducted on a three span reinforced concrete bridge strengthened by the addition of external steel reinforcement in regions of high positive moment. Free vibration response and controlled impact excitation consistently created the most reliable modal properties.

2.1.3 Applications of VBDD to Bridges in the Broader Research Community

Brownjohn et al. (2003) performed forced vibration testing (shaker excitation) and ambient vibration monitoring to assess the effect of upgrading on a simply supported 18.16 m span bridge in Singapore. The main upgrading work involved replacing nominal simple supports with those approximating nominal full fixity. By employing structural identification techniques to develop calibrated finite element models using data obtained both before and after upgrading of the bridge, the authors found that the alteration of boundary condition was the principal cause of natural frequency increases of up to 50%.

Halling et al. (2001) carried out several forced vibration tests on an isolated single span of a freeway overpass structure in connection with a series of controlled damage and repair states. The authors found that the calibrated analytical model was capable of successfully identifying damage or retrofits on the structure, as well as estimating their location and extent.

A study by Alampalli et al. (1997) showed that there was some difficulty in using mode shapes to locate deterioration since modal amplitudes within undamaged and damaged sections were similarly affected by the damage. They suggested that natural frequencies and mode shapes that possess high degrees of sensitivity to damage may be used to identify the location of damage. Impact tests were conducted on a one-sixth-scale multiple steel-girder model, as well as on full-scale two steel girder bridges in both intact and simulated (saw-cut) damage states.

Farrar et al. (1997) reported on extensive testing of damage detection methods on the Alamosa Canyon Bridge in New Mexico. Both forced and ambient vibrations were applied while measurements were made using a dense array of accelerometers. Among the important outcomes was the observation of variability of various modal parameters

resulting from changes in the time of day when the test was performed, the amount of traffic, and other environmental conditions.

Salawu and Williams (1995) conducted full-scale forced vibration tests before and after structural repairs on a multi-span reinforced concrete highway bridge. They found that the natural frequencies did not change significantly as a result of structural repairs. The modal assurance criterion (defined in Section 6.2) and the coordinate modal assurance criterion values were found to be good indicators of the presence and location of damage for the condition assessment of the bridge.

Pandey and Biswas (1994) proposed a method for detecting and locating damage in structures based on the computation of change in the flexibility matrix. The method was applied to several numerical examples, and to a simply supported W12x16 beam. The beam had a splice at mid span. The success of the method using the experimental data suggested the practical applicability of this method for full-scale structures. It was found that the proposed method worked best when damage was located at a section where high bending moments occurred.

Mazurek and DeWolf (1990) conducted ambient vibration tests on a two span aluminium plate girder bridge in the laboratory. They used low mass vehicular excitation and found that the ambient vibration method provided approximately the same resonant frequencies and mode shapes as those derived using conventional modal analysis techniques like those employing an impact hammer. It was found that crack propagation and changes in the support conditions caused significant changes in natural frequencies and mode shapes.

As demonstrated, several researchers have applied VBDD methods to laboratory models and actual bridges. The methods have been quite successful with laboratory models. The models in the laboratory could mainly be categorized as beams, columns, trusses and frame structures; in addition, the location and severity of damage in the models were known in advance.

The field testing and damage assessment of real bridges are more complicated than those of models in the laboratory. Past research has generally focused on a few, relatively severe damage scenarios and has shown some success in assessing the presence and

location of damage on the bridge structures in these cases. The correlation between the damage indicator and damage type, location, and extent still needs to be improved. Studies conducted to date have also revealed many challenges in applying VBDD methods to bridge structures, including those caused by the large physical size, low natural frequencies and vibration levels, the diversity of test structures (e.g. materials, support conditions, and connectivity of components) and variability in loading and environmental conditions.

In spite of the these challenges, vibration-based health monitoring looks to be a promising method for the detection of damage and condition assessment of bridge structures, with the potential to help infrastructure owners reduce maintenance costs by reducing service disruption, allowing early detection of problems, avoiding catastrophic failures and improving the safety and reliability of structures.

2.2 INFLUENCE OF ENVIRONMENTAL EFFECTS ON THE APPLICATION OF VIBRATION-BASED DAMAGE DETECTION

Many issues are critical for the successful application of VBDD methods to bridge structures. One of the most important current challenges is the variability of modal parameters caused by changing environmental and operational conditions, especially those relating to temperature variation.

Temperature change may have an impact on the boundary conditions and on the material properties of a bridge; they will, therefore, also have an influence on the structure's eigenfrequencies (Peeters et al. 2001). The basis for VDBB is that damage may cause the loss of stiffness at some location along the bridge, and hence decrease the eigenfrequencies. However, the changes of modal properties caused by temperature variation may be greater than the changes in modal parameters caused by damage or deterioration, resulting in an incorrect diagnosis by either falsely identifying non-existent damage or masking actual changes due to deterioration. Thus, before comparing sets of dynamic parameters to detect damage, the effect of changing temperature on modal properties must be considered.

The literature related to temperature effects on bridge structures is long and substantial. However, previous research has mainly concentrated on structural design considerations which result from temperature changes, as well as on thermal-stress induced damage and fatigue. There has been very little study of the effect of ambient temperature on modal parameters.

Wahab and De Roeck (1997) investigated the effect of temperature change on the natural frequencies of a three span box girder highway bridge. The bridge was skew-symmetric with skew angle of 43°. The bridge was excited by a drop weight and by ambient vibrations. It was found that a decrease in temperature from 15°C to 0°C led to an increase in natural frequencies for all measured modes of 4-5%. It was concluded that the decrease in temperature mainly affected the elastic modulus of the asphalt pavement, thus producing changes to the natural frequencies of the bridge.

Alampalli (1998) conducted field tests over a 9 month period on an abandoned steel-stringer bridge with a concrete deck. It was found that the relative eigenfrequency differences caused by freezing of the supports were larger than the changes due to damage, which took the form of an artificial saw-cut across the bottom flanges of both girders. It should be mentioned that the bridge under investigation was small, with a span of 6.76 m and a width of 5.26 m.

Sohn et al. (1999) developed a linear adaptive model to describe the variation of the eigenfrequencies of the Alamosa Canyon Bridge caused by changes in the environmental temperature. The model was used to establish confidence intervals of the frequencies for a new temperature profile. It was suggested that changes in mass due to moisture absorption and retention by the bridge may have a significant effect on the eigenfrequencies. Cornwell et al. (1999), using the data from the same bridge, found that the frequencies of the first, second and third modes varied by approximately 4.7%, 6.6% and 5%, respectively, over a 24-hour period due to temperature differential across the deck.

Lloyd et al. (2000) presented correlations of the modal frequencies with seasonal temperatures during a seven month period of observation for a large-span prestressed segmental concrete bridge over a temperature range of -15°C to 33°C. It was found that

the temperature sensitivity coefficients for the first four vertical mode frequencies computed from the field data varied from -3.1320×10^{-3} (Hz/ ^{o}C) to -1.8282×10^{-3} (Hz/^{o}C), which are relatively low.

The results of a study by Rohrmann et al. (2000) from six years of monitoring the Westend Bridge in Berlin showed that the variation of the natural frequencies could be approximately described as being linearly dependent on measured temperature. It was found that, for each temperature, a relatively high scatter of natural frequencies occurred. They proposed the following relationship between a change in frequency, Δf, and certain temperature parameters for beamlike structures:

$$\Delta f = a_0 T_0 + a_1 \text{gradT} \quad , \qquad [2.1]$$

where T_0 and gradT are, respectively, the mean temperature of the structure and the temperature gradient through the height or width of the cross section. The parameters a_0 and a_1 must be determined from the measured data.

Peeters and De Roeck (2000) conducted a one year monitoring study of the Z24 Bridge in Switzerland under ambient vibrations. They presented a method to distinguish normal eigenfrequency changes resulting from the environmental effects, such as wind and temperature, from damage events. It was demonstrated that the bilinear behaviour between temperature and frequency was mainly due to the variation of Young's modulus of the asphalt layer with temperature. Peeters et al. (2001) developed Autoregressive Exogenous (ARX) models to fit the same bridge data. These models were used to simulate and separate the identified frequencies from the temperature effect.

Londoño and Lau (2006) presented data relating to the variability of the vibration characteristics of the Confederation Bridge, extracted from the measured ambient vibration monitoring data. An attempt was made to quantify the variability arising from the measurement, modelling and computational uncertainties, as well as that caused by the environmental and loading fluctuations. It was found that the standard deviations of extracted modal frequencies under random environmental and loading fluctuations were approximately 1.1% of the mean, which was approximately two times greater than the standard deviation due to measurement and modelling uncertainties. Temperature was identified as the factor that was mainly responsible for the variation of eigenfrequencies.

As mentioned above, past studies examined the effect of temperature and other environmental factors on natural frequencies. However, the influence of temperature on mode shapes, the pattern of mode shape changes caused by temperature variation, and methods to differentiate between mode shape changes due to temperature and mode shape changes due to damage remain largely unknown.

These considerations led to a program designed to quantify in a numerically meaningful way the temperature-mode shape relationships for a composite (concrete deck on steel-girder) integral abutment bridge in a climate as cold as that in Saskatchewan. It was intended that these relationships could be used as part of an ongoing monitoring program.

2.3 DAMAGE DETECTION TECHNIQUES

Vibration-based damage detection methods rely on modal parameters to detect damage. Modal analysis has become a standard practice for engineers to describe the dynamic properties of a structure in terms of natural frequencies, damping ratios and mode shapes. By detecting changes in these parameters, the presence and location of damage can be theoretically determined.

Doebling et al. (1996) and Sohn et al. (2003) give extensive literature reviews on vibration-based damage detection methods and their application to civil, mechanical and aerospace structures. The first review (Doebling et al. 1996) classified the methods according to required measurement data and analysis techniques. The literature review concentrated primarily on Levels 1 to 3 of damage detection. Most of the literature reviewed focused on laboratory structures or controlled damage to field structures and did not attempt to predict the remaining service life of a structure.

Different approaches were identified, from over 250 references, which they categorised as follows: natural frequency based methods (Cawley and Adams 1979; Salawu 1997; Peeters 2000), mode shape based methods (Fox 1992; Srinivasan and Kot 1992; Salawu and Williams 1994), mode shape curvature/strain mode shape based methods (Pandey et al. 1991; Zhang and Aktan 1995; Kim and Stubbs 1995, 2003), dynamically measured flexibility based methods (Pandey and Biswas 1994; Zimmerman and Kaouk 1994),

matrix update based methods (Hajela and Soeiro 1990; Casas and Aparicio 1994; Hu et al. 2001), non-linear methods, and neural network based methods (Wu et al. 1992; Masri et al. 1996).

Among the various vibration-based techniques, the methods used in this research are methods that rely on direct changes to mode shapes, changes to mode shape curvatures, changes to modal strain energy, changes in uniform flexibility curvature and changes in flexibility to characterize damage. These five methods were used extensively in Zhou et al. (2003, 2004, 2007), and Siddique et al. (2005, 2006, 2007). These techniques are described in Chapter 4.

CHAPTER 3 . EXPERIMENTAL PROGRAM

3.1 INTRODUCTION

This research is composed of an experimental program and numerical studies to determine the effect of ambient temperature on the dynamic properties of the Attridge Drive Overpass. This chapter focuses on a description of the experimental study.

The experimental program involved dynamic field measurements taken at the bridge site. The vertical acceleration response of the deck under traffic excitation and ambient temperatures were measured. These measurements were used to extract the dynamic properties (natural frequencies and mode shapes) over a range of temperatures as well as to provide a basis for calibration of the finite element model.

This chapter includes a description of the measurement procedure and the data acquisition/instrumentation system, followed by a discussion of the data collection process.

3.2 BRIDGE DESCRIPTION

The Attridge Drive Overpass (Figure 3.1 and Figure 3.2) is located at the intersection of Attridge Drive and Circle Drive in the City of Saskatoon, Saskatchewan, Canada. Built in 2001, the structure is a two-span integral abutment bridge with an alignment that is skewed by $16^{o}5'16''$ and span lengths of 38.7 m and 30.6 m. The overpass is a composite steel girder-concrete deck structure with a 300 mm thick reinforced concrete deck and a 90 mm polymer modified asphalt wearing surface. Supported by nine built up steel girders, the bridge deck is 27 m wide and is sloped at 2% towards the outside shoulders. As can be seen in Figure 3.3, the bridge features four eastbound lanes

(including the turning lane) and two westbound lanes, with a 1000 mm wide reinforced concrete median strip.

Figure 3.1. Arial view of the Attridge Drive Overpass (Source: Microsoft Bing Maps).

Figure 3.2. Attridge Drive Overpass, viewed from the north side.

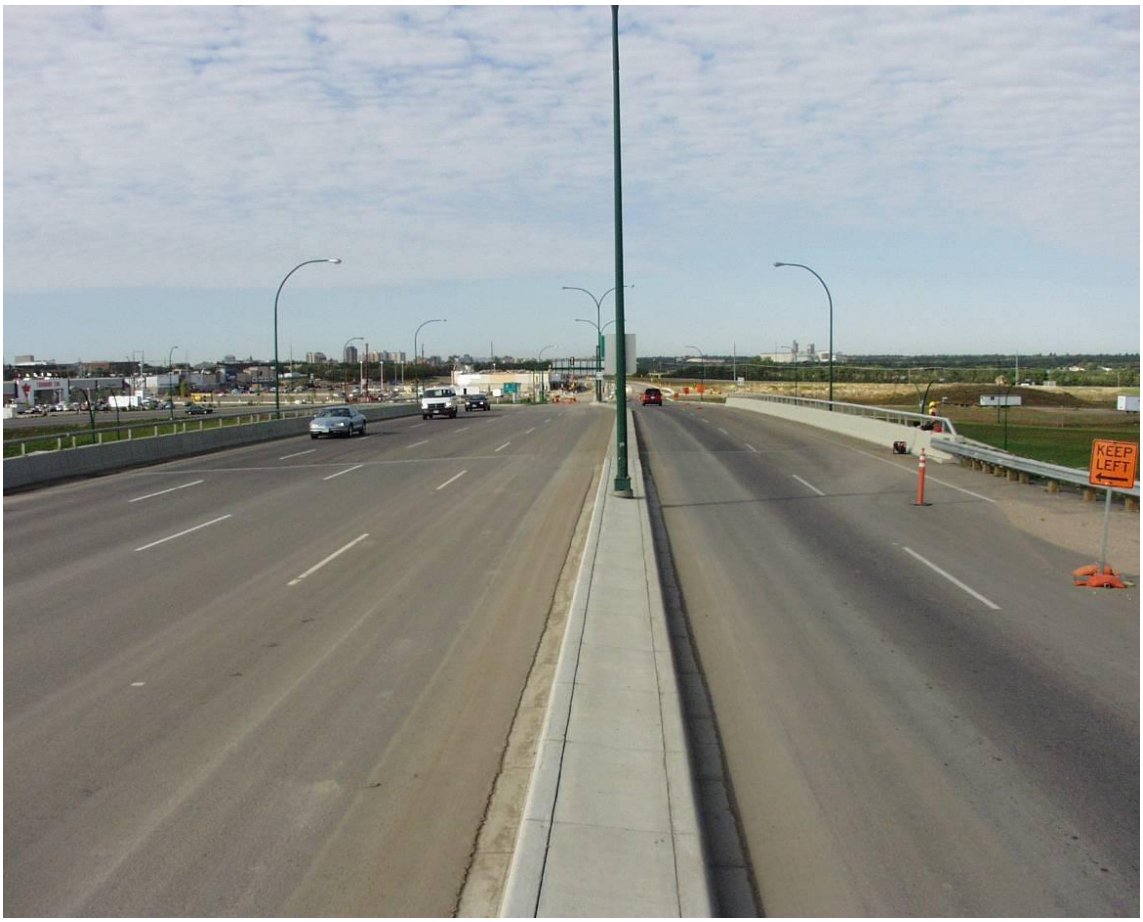

Figure 3.3. Driving lanes, viewed from the East.

As seen in Figure 3.4, the abutments were cast integrally with the deck slab and girders, allowing the bridge to accommodate thermal effects by flexural frame action, thereby eliminating the need for expansion joints. The abutments rest directly on a single row of friction belled piles, and are connected to the piles by dowel bars. This configuration is assumed to act as a pinned connection, which should theoretically allow some rotation of the abutments when subject to thermal movement.

Approach slabs 6000 mm long and 300 mm thick are anchored into the abutment back-wall so that they move in concert with the bridge. At the pier, the girders are welded to the sole plates, which rest on neoprene pads and are anchored to the pier cap in a direction parallel to the skew alignment. This configuration is intended to create the equivalent of roller supports at the pier to allow the bridge to move freely in the longitudinal direction. The connection between the pier and girders is illustrated in Figure 3.5.

Figure 3.4. Deck slab and girders cast integrally with the abutment.

Figure 3.5. Connection between girders and pier.

3.3 FIELD TEST PROCEDURE AND SETUP

The dynamic response of the Attridge Drive overpass was monitored over a period of three years, during which time it experienced full seasonal changes, with ambient temperatures ranging from approximately - 40°C to 40°C.

Test schedules were established in consultation with the City of Saskatoon for the performance of the ambient vibration tests. The city provided traffic control during the testing so that the bridge could be safely instrumented. The lanes adjacent to the instrumented barrier wall were temporarily closed during measurement and subsequently re-opened to traffic (Figure 3.6). The ambient air temperature was also recorded intermittently during each seven hour test period (approximately 9:00 a.m. to 4:00 p.m.) in order to establish the relationship between the temperature change and measured dynamic response. Temperature was measured by a thermometer placed in a shaded area on the bridge deck near the barrier wall.

Figure 3.6. Closed lane during testing.

Measurements were taken of the response due to normal traffic (ambient) conditions. An effort was made to wait for the arrival of heavy vehicles in order to excite a large amplitude response and to facilitate the observation of a period of relatively free vibration afterwards. Since one lane was closed during testing, the bridge experienced lower amplitudes of excitation than normal due to the resulting reduced traffic speed.

The dynamic response data were collected from the structure using seven accelerometers connected to a portable data acquisition system. The instrumentation system is described in the next section. Since only seven accelerometers were available, four different setups were needed to measure the modal properties of the entire bridge. For each setup, six accelerometers were installed as a group in a given quadrant of the bridge. When testing was complete in one quadrant, tests were repeated with accelerometers installed in each of the remaining quadrants. The seventh accelerometer was left at a fixed location as a reference accelerometer so that the readings from each quadrant of the bridge could be scaled in reference to it, and then 'glued' together to reconstruct the response of the whole bridge, as described in Section 3.5.3 (Hermans and Van Der Auweraer 1999, Brownjohn et al. 2003).

In each quadrant, six accelerometers were mounted to the top of the barrier walls at approximately 5.0 m intervals longitudinally, with the first accelerometer located 5.0 m from the centre-line of the abutment wall in that quadrant (Figure 3.7). Since the overpass was in service during testing, accelerometers were temporarily installed on top of the barrier walls. They were attached to the barrier walls by anchor bolts drilled into the concrete and were levelled with the use of a carpenter's level. For each set-up, a few trials were recorded to check the working condition of equipment before saving the vibration data for subsequent analyses.

In addition to the accelerometers, 51 electrical resistance 350-ohm strain gauges with a 6 mm gauge length were permanently installed on four of the nine steel girders shortly after the bridge was constructed in 2001. The strain gauges were mounted to measure longitudinal strains on the webs of the steel girders in groups of three, aligned vertically, to provide curvature measurements at 17 locations. The strain gauge data are not included in this thesis.

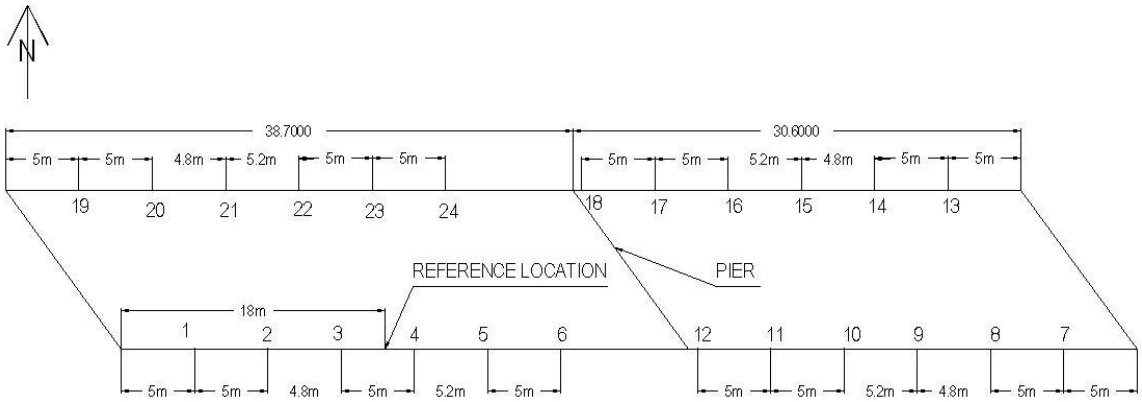

Figure 3.7. Plan of the bridge deck, showing the location of the accelerometers.

At least ten loading events were recorded for each of the four accelerometer configurations for each site visit. This enabled the averaging of response data to attenuate the effects of random measurement noise and excitation characteristics and to provide numerous data sets to establish consistent natural frequencies. Only the accelerations perpendicular to the plane of the concrete deck were measured, since the transverse and longitudinal movement of the bridge are far less pronounced. The data used in this study were acquired during five site visits. The date and range of ambient temperatures for each testing period considered in this study are shown in Table 3.1. As an example of the more detailed data that was recorded, the loading events and ambient temperatures that were recorded in two of the bridge quadrants for the 30th March 2005 field test are shown in Table 3.2.

Many of the records were not useful for determining the bridge's modal parameters due to the low amplitude response of the bridge resulting from relatively low velocity and light weight vehicles crossing the bridge at that time. The tests that provided the most valuable data resulted from the excitation caused by the passing of one or two large tractor-trailer units, subjecting the bridge to an initial disturbance followed by a period of pronounced free vibration. However, there were also times when large vehicles provided poor data. It appears that this was due to other vehicles following the tractor-trailers, resulting in a dampening effect on the free vibration of the bridge.

The quality of measured accelerations were affected to a large degree by the weather conditions, as well as by various difficulties encountered with data acquisition. During cold weather conditions, the possibility of snow or water getting inside the wiring

connections increased, causing those particular connections to short out, and leading to useless data. Also, during winter testing, prior to the installation of anchor bolts to fasten accelerometers to the barrier wall concrete, the accelerometers were attached to the concrete using frozen water, which resulted in measurements that were taken when the accelerometers were not levelled properly or had become unattached from the concrete surface at some locations.

On some test days, measurements were only taken in two or three quadrants of the bridge deck instead of all four. This was due to insufficient time being available for the recording of data, and also to time spent resolving problems that occurred during installation of sensors and the data acquisition system, as well as for the calibration of sensors.

The accelerometers used in this research, according the manufacturer's manual (Kinemetrics, Inc., 2002), may be operated within the temperature range of -20°C to 70°C. It was observed that their performance was greatly impaired for temperatures near the lower end of this range, thereby affecting the quality of field data when the air temperature approached -20°C.

Table 3.1. List of test dates and temperature ranges.

Date	Temp. (°C)	Sampling Frequency (Hz)	No. of Accelerometers	Note
4 Jul 2003	20 to 26	150	6	
24 Jul 2003	30 to 40	150	6	Six accelerometers were not working properly on the north side of the bridge
24 Nov 2003	-9 to -7	300	6	Channel 4, corresponding to locations of 20 m and 49.3 m from west abutment, was not working.
3 Mar 2004	-12 to -5	300	6	Channel 4, corresponding to locations of 20 m and 49.3 m from west abutment, was not working.
30 Mar 2005	4 to 7	300	6	Six accelerometers were not working properly on the south side of the bridge

Table 3.2. Loading events and measured ambient air temperatures on 30th March 2005.

Quadrant	Sampling Rate (Hz)	No.	Temperature (°C)	Type of vehicle
North East	300	1	7.3	5 ton truck
		2		3 ton truck, 1 ton truck
		3		2 ton truck
		4	6.7	Bus
		5		Semi trailer truck
		6		1 ton truck
		7	6.3	2 ton truck
		8		5 ton truck
		9		Access Transit Bus
		10	6.5	Bus
		11		Bus
North West	300	1	4.8	Semi trailer truck
		2	5.1	Bus
		3	4.6	5 ton truck
		4		Semi trailer truck, Van
		5	6.1	Bus, Bus
		6		Semi trailer truck, 2 ton truck
		7	5.7	Bus
		8	5.2	5 ton truck
		9		Semi trailer truck
		10	4.25	1 ton truck
		11		Bus

The field measurement program was also faced with other difficulties and restrictions such as harsh weather conditions, the scheduling of traffic control provided by the City of Saskatoon, difficulties in accessing some parts of bridge and the limited number of sensors. All of this would limit the number of tests that could be carried out on the bridge and also would affect the quality of the data that was obtained.

3.4 DATA ACQUISITION SYSTEM

3.4.1 Data Acquisition System Components.

Data were acquired using a portable, computer-based data acquisition system manufactured by National Instruments (Austin, Texas), which consisted of the following measurement hardware and software items: Episensor accelerometers, signal conditioning modules, a data acquisition chassis, a dynamic data acquisition Peripheral

Component Microchannel Interconnect Architecture (PCMCIA) card, terminal blocks, connectors, cables, a power supply, and data acquisition software. The hardware components of the measurement system are shown in Figure 3.8.

The accelerometers used in this study were Episensor single-axis acceleration sensors model FBA ES–U, obtained from Kinemetrics, Inc. (Pasadena, California). These sensors are force-balance type accelerometers with full-scale recording acceleration ranges of ± 0.25g to ± 4g. A typical accelerometer is shown mounted on a barrier wall in Figure 3.9.

Figure 3.8. Data acquisition system.

Figure 3.9. Accelerometer used during measurement.

Each accelerometer was attached to a single channel or terminal on the National Instruments SCXI-1320 High-Voltage Terminal Block by connectors. The terminal block provided an efficient method for connecting and disconnecting accelerometers to the data acquisition system.

The terminal blocks were connected to an 8-Channel Isolation Amplifier module (National Instruments model SCXI-1120) that provided the signal conditioning. This module has eight isolated input channels with selectable amplifier gains up to 1,000 times the signal strength and configurable analog lowpass filters of 4 Hz and 10 kHz on each channel. A gain of 1 and a low pass filter bandwidth of 10 kHz were used when acquiring the signal in this study. The gain was used to amplify the low voltage signal before it was converted to a digital signal, thereby increasing the accuracy of the conversion. The filtering permitted a higher signal to noise ratio by eliminating high

frequency noise generated by the amplifier and other sources. The SCXI-1120 module also samples the analog input channels.

The terminal block and the module were housed in a data acquisition chassis (National Instruments model SCXI-1001). The chassis can hold up to 12 SCXI modules. The chassis also provided electrical power and control circuitry for the module.

The chassis was connected to a dynamic data acquisition PCMCIA card (model NI DAQCard-6036E) from the same manufacturer. This card has a maximum sampling rate of 200,000 samples/second and a 16 bit accuracy. The card managed the operation of the data collection and digitized the conditioned analog signals from the module. It also communicated directly with the laptop computer that stored the data for future processing and diagnostics through the PCMCIA slot. Figure 3.10 provides a schematic description of the data acquisition process.

The data acquisition system (hardware) was configured by the software Measurement and Automation Explorer (MAX) from National Instruments through the use of device test panels, interactive measurements, and scaled Input/output (I/O) channels. MAX provided access to National Instruments devices, as well as managing the addition of new channels, interfaces, and virtual instruments, and viewing the devices and instruments connected to the system.

The data were acquired and manipulated using LabView routines and were stored digitally on a laptop computer. The LabView routine converted the digitized voltage time history from an accelerometer to an acceleration-time history and saved it in American Standard Code for Information Interchange (ASCII) format for later analyses.

A sampling rate of 300 samples per second was used for a typical trial period of 10 seconds, resulting in a total of 3000 samples being acquired for each channel. This ensured that the sampling rate chosen was considerably greater than twice the desired natural frequencies of the bridge to avoid aliasing, which would result in the contamination of lower frequencies by higher frequency components. The period of the sampling rate was also chosen to be less than the difference between the natural periods of the first five modes. This ensured sufficient frequency resolution to facilitate the measurement of individual modes.

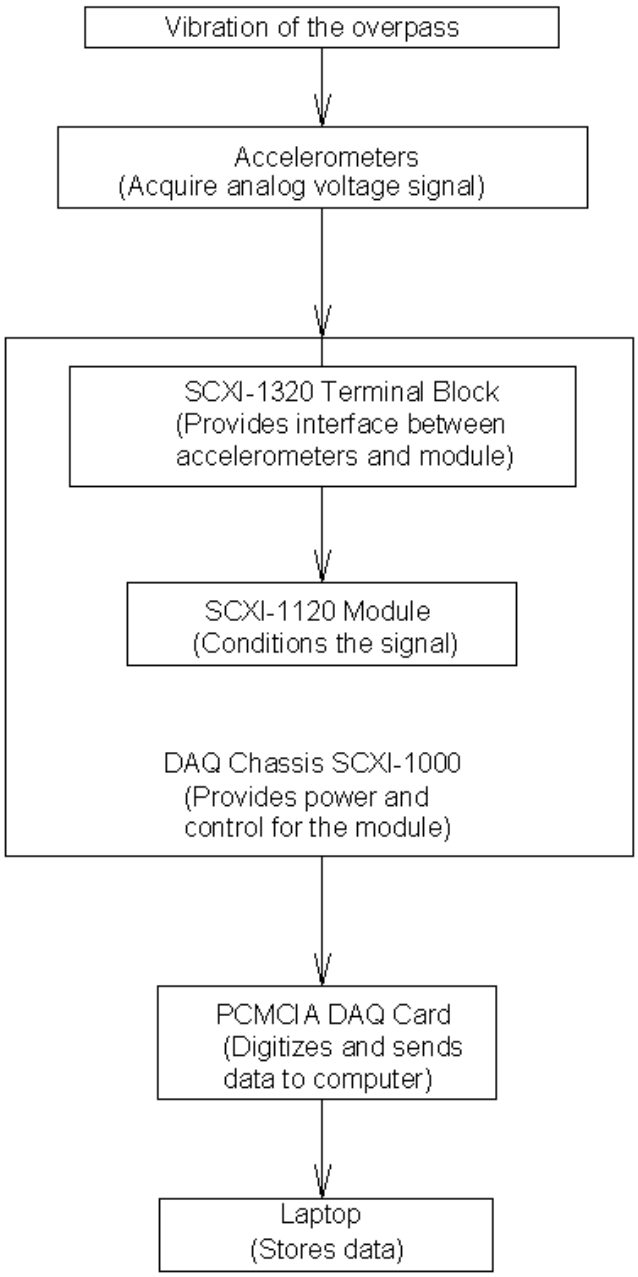

Figure 3.10. The flow chart of data acquisition system components.

3.4.2 System Calibration

The data acquisition system was calibrated in the Structures Laboratory of the Civil and Geological Engineering Department of the University of Saskatchewan one week before every field visit.

The accelerometers were calibrated not only to acquire a precise measurement value, but also to ensure that the readings were consistent among the sensors. The sensors were

placed onto a flat and still floor. First, a functional check of the sensors was performed by tilting the sensors +90° and –90° about each of the sensor's principal axes. The measured acceleration was adjusted to ± 1 g. Then, the sensors were stacked one on top of the other in a wooden box and exposed to vibration consisting of manual shaking in the vertical direction. The calibration factors were manually adjusted after each shaking trial so that the differences between measured acceleration amplitudes at different sensors were minimized.

The calibration was performed on the individual sensors attached to their dedicated wires that would be used during measurement. A change in cable length would have altered the system's sensitivity since the voltage produced by the accelerometer is divided between the accelerometer's capacitance and the cable's capacitance. The configurations of the accelerometers and SCXI-1120 module were set by changing jumpers on the devices. The accelerometers were configured to a range of ± 0.5 g, a differential output voltage level of 5 V, and a sensitivity of 10 V/g. This resulted in a precision of 0.00025 g for acceleration measurements. A gain of 1 and a low pass filter bandwidth of 10 kHz were set in the module, as mentioned previously.

3.5 DATA PROCESSING

3.5.1 Overview

Data processing involves separating the extraneous information from the cleansed data, and extracting the dynamic properties of the structure (i.e., its natural frequencies and mode shapes) from individual accelerometer signals in preparation for the damage detection and modelling analyses.

The previous section described how an analog voltage signal from an accelerometer was first conditioned by measurement hardware and then digitized into discrete acceleration-time histories. As described in greater detail below, each acceleration-time history was then digitally conditioned to remove noise and error. A Fast Fourier Transform (FFT) was then used to transform the time history to a frequency response spectrum. The flow chart illustrating the data processing procedures is shown in Figure 3.11.

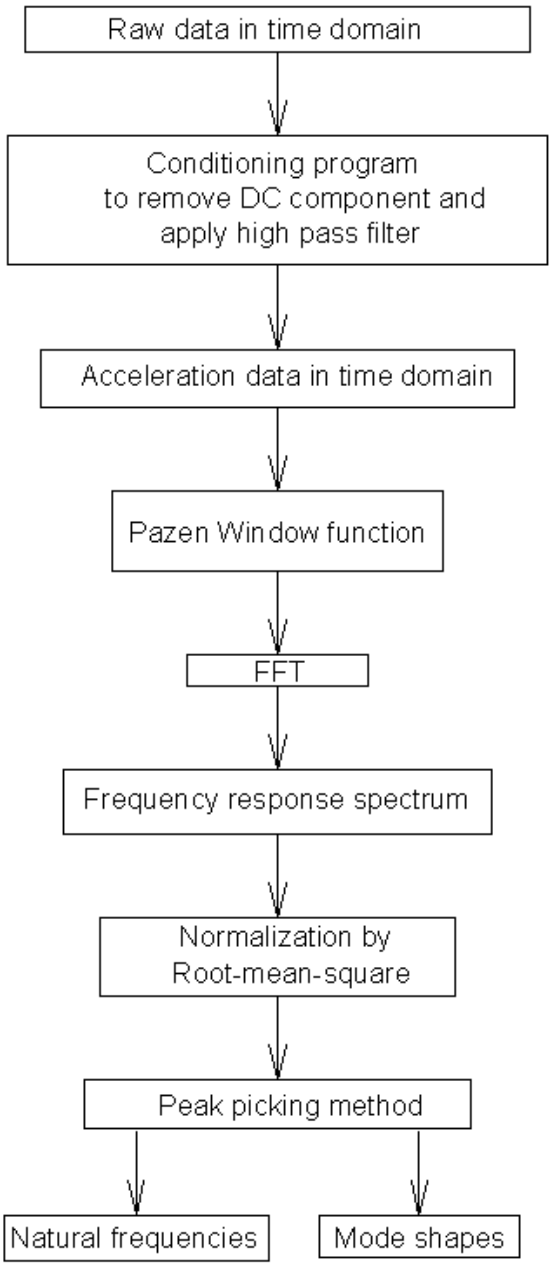

Figure 3.11. The flow chart for data processing.

One commonly used method to extract the modal properties of the structure is to pick the peaks in the frequency response spectra as candidates representing the natural frequencies of the bridge. The mode shapes are constructed from the relative amplitudes of the peaks of the spectra from different sensors on the structure at the same peak frequency. Each of these steps is described in greater detail in the following sections.

3.5.2 Data Conditioning

In every step of the data processing, numerous procedures were used. The acquired digitized readings contained some errors and noise due to ambient interference, equipment-related errors caused by calibration and zero drift, limited resolution and other sources that cannot be eliminated but, nonetheless, can be minimised.

The digitized acceleration-time histories from individual accelerometers, an example of which is shown in Figure 3.12, were processed by running a series of FORTRAN routines. The first routine removed the direct current (DC) initial offset (time-averaged mean value). This routine also filtered the signal by a digital high pass (1^{st} order recursive) filter (Proakis and Manolakis 1992), which attenuated low frequency components and passed high frequency components in order to eliminate acceleration drift. The first order recursive filter is given by the expression

$$y_n = 0.999 y_{n-1} + x_n - x_{n-1}, \qquad [3.1]$$

where x_n is the instantaneous measured acceleration at the instant t_n, x_{n-1} is the instantaneous measured acceleration at the previous instant t_{n-1}, and y_n is the conditioned (modified) acceleration reading at the same time instant.

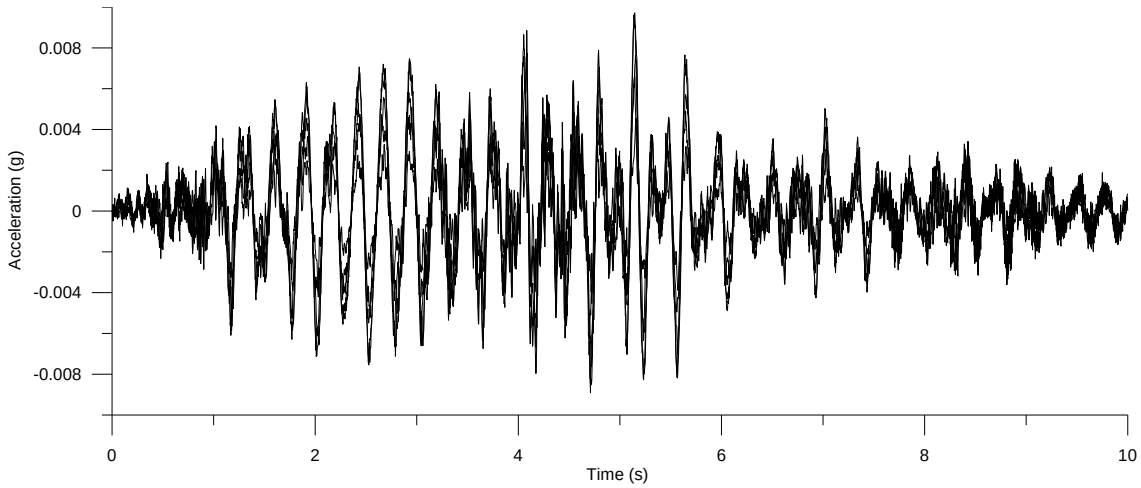

Figure 3.12. Example of acceleration-time history plots acquired from several accelerometers.

A second routine was used to apply a window function to the data. The abrupt truncation of a signal during sampling leads to the introduction of artificial frequency components in the response spectrum. In order to avoid this, all time series data were conditioned by a Parzen window function (Ramirez 1985), which smoothes the transition of the signal to zero at both ends of the sampling periods, prior to performing FFT analyses.

3.5.3 Modal Parameter Extraction.

After conditioning, the acceleration-time histories were converted to a frequency domain representation through the use of an FFT. The FFT produces the average frequency content of a signal over the entire time that the signal was acquired. The FFT spectrum output of an acceleration-time history is complex; that is, every frequency component has a magnitude and phase angle. The phase angle is defined relative to the start of the time record, or relative to a cosine wave starting at the beginning of the time record. The FFT response spectra for the signals shown in Figure 3.12 are shown in Figure 3.13. The corresponding phase angle plots over a frequency range that includes first three natural frequencies of the overpass are shown in Figure 3.14.

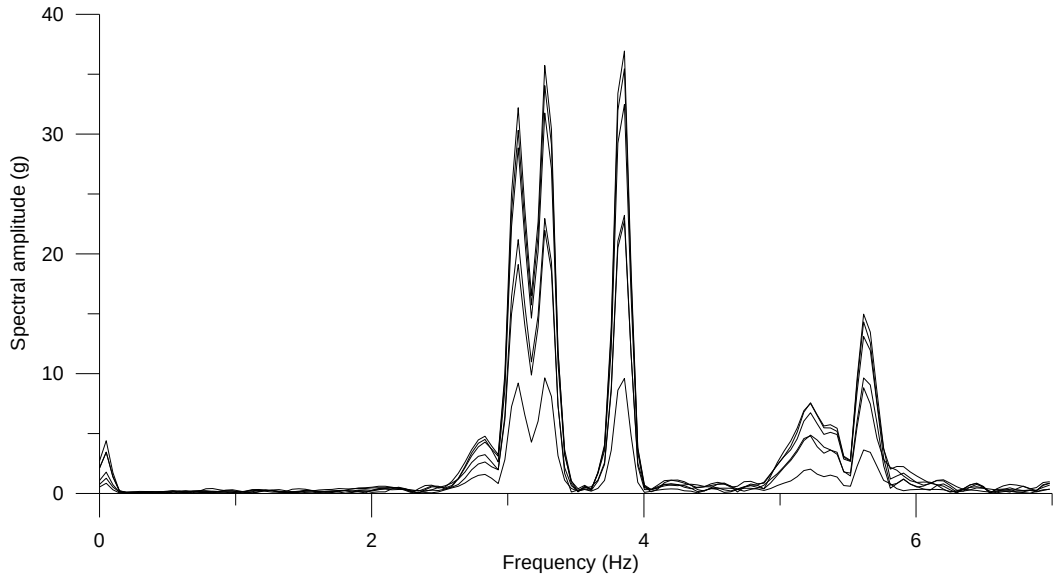

Figure 3.13. Fast Fourier Transform spectra for several accelerometer signals obtained during the same event.

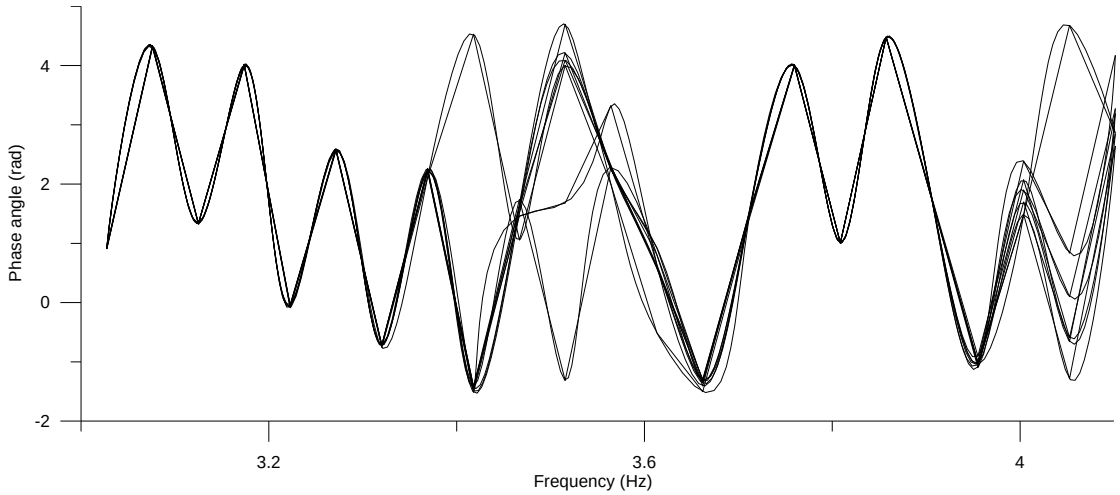

Figure 3.14. Phase angle plots for several accelerometer signals obtained during the same event.

Due to the unknown input excitation force arising from ambient vibration, traditional modal analysis techniques based on the frequency response function (FRF), which relates measured output to measured input, could not be applied to extract the dynamic characteristics of the overpass. A peak picking method based on normalized spectra of accelerometer signals was used instead. In this approach, it is assumed that the bridge would either vibrate at its own natural frequencies or at frequencies induced by the forced vibrations. It is possible to identify peaks in a response spectrum plot that correspond to the damped natural frequencies of the structure, but it is sometimes difficult to distinguish between peaks that represent natural frequencies from those due to excitation induced by heavy vehicles. Natural frequencies were identified in the following manner.

First, each response spectrum was normalized by its root-mean-square (RMS) value to eliminate the influence of event intensity. Several response spectra from the same accelerometer but corresponding to different events were then averaged. This averaging process tends to attenuate the peaks at vehicle-induced response frequencies since these tend to be random in nature, while the response at natural frequency tends to be persistent.

For vibration components at the natural frequencies, the measurement points will vibrate either in phase or 180° out of phase with one another. In the phase angle plots of the

response spectra, for those frequencies where a peak in the response spectra corresponds to the excitation force (i.e., the passing of a heavy truck), the phase angle between any two output measurements will usually be something other than zero or 180°. This fact was used to assist in identifying the natural frequencies from the response spectra for each loading event.

The most commonly appearing frequency values at the first three spectral peaks for each bridge quadrant in a particular temperature range were then selected as the natural frequencies for that quadrant in that temperature range. The natural frequencies of the overpass in that temperature range would then be calculated as the average of the values for all four bridge quadrants.

Once the natural frequencies had been identified, the relative modal amplitudes at various measurement locations were computed from the original response spectra corresponding to individual events. The acceleration magnitude at each natural frequency was normalized by the corresponding frequency amplitude from the reference accelerometer for that event, at the same natural frequency. The normalized acceleration amplitudes at a particular measurement location corresponding to several repeated trials were then averaged. The phase angle plot of the response spectrum was also examined to determine whether a particular measurement location was vibrating in phase or out of phase with the reference accelerometer.

The mode shape of the bridge was determined by plotting the average normalized acceleration magnitudes at each measurement location with respect to length along the bridge deck. An example of an experimentally derived mode shape is displayed in Fig. 3.15.

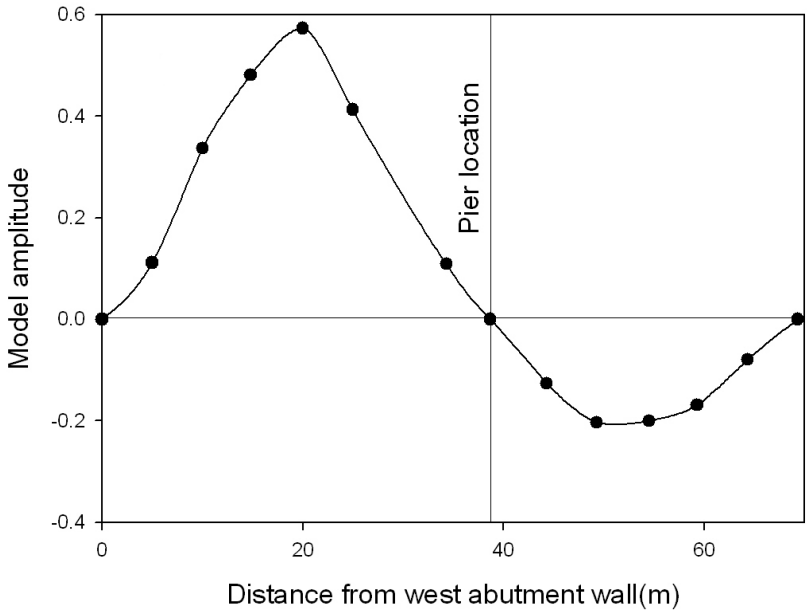

Figure 3.15. Mode shape of first natural frequency (3.25 Hz) along the north side of the bridge in a temperature range of 4°C to7°C.

CHAPTER 4 . NUMERICAL STUDY

4.1 INTRODUCTION

As mentioned previously, this research consisted of experimental and numerical studies of vibration-based damage detection (VBDD) techniques. This chapter focuses on a description of the numerical study.

A finite element (FE) study of the dynamic behaviour of the overpass was implemented to investigate the influence of temperature variation and damage - both independently and together - on the natural frequencies and mode shapes, and on the distributions of the VBDD parameters. The finite element models used in this research were modifications of an existing model prepared by Siddique et al. (2005).

This chapter describes the creation of the finite element models, including discretization into elements, boundary conditions, and material models. Also covered is the model calibration, as well as simulation of damage scenarios in the models. The implementation of the five VBDD techniques is also presented.

4.2 DESCRIPTION OF FINITE ELEMENT MODEL

4.2.1 Elements and Discretization

The earlier model developed by Siddique et al. (2005) was created to study the application of vibration-based damage detection methods to the bridge under investigation and the influence of uncertainty of mode shape measurements. It was built using the commercial analysis program Automatic Dynamic Incremental Nonlinear Analysis (ADINA) (2002). For this earlier model, the reinforced concrete bridge deck was modelled using 8-node 3-dimensional isoparametric solid elements: 29 elements

longitudinally, 31 elements transversely, and three vertical layers that were 50 mm, 75 mm, and 100 mm deep, respectively. Three-dimensional solid elements were also used to model abutments and barrier walls. The girder flanges and webs were modelled using 4-node shell elements. Shell transition elements were used to model the intersection between shell elements (girders) and 3-dimensional solid elements (abutment). The beam diaphragms (diaphragms at the pier) were represented by shell elements, while truss diaphragms (diaphragms located between the pier and abutments) were modelled by truss elements and 2-node hermitian beam elements. The barrier walls were modelled with 29 solid elements along the length of bridge, and were spatially separated slightly to account for their actual segmental construction.

To study the effect of temperature on the dynamic properties and on the implementation of vibration-based damage detection methods on the overpass, the earlier finite element model was modified and more elements were added, as described below.

One additional 90 mm thick element layer was added to the top surface of bridge deck to represent the asphalt surface. In addition, the 20 cm thick concrete median strip was also created. Both the asphalt layer and the median were modelled using eight-node three-dimensional isoparametric solid elements with six degrees of freedom per node.

A finer mesh, using elements which were longitudinally half the size of those used in the original model of Siddique et al. (2005), was applied to the 4 layers of the bridge deck, as well as to the median, barrier walls and girders. As a result, the deck slab was discretized into 7752 three-dimensional solid elements.

The finite element model of the bridge is shown in Figure 4.1. It had a total of 15369 nodes, 112 truss elements, 112 beam elements, 2486 shell elements, 896 spring elements, 8560 three-dimensional solid elements and 48494 degree of freedom.

4.2.2 Boundary Conditions

The same boundary conditions used in the earlier version of the model were imposed at the pier and abutments. The nodes at the bottom flanges of the girders directly above the pier were restrained against vertical translation, as well as against lateral translation and

rotation. These nodes were free to translate and rotate in the longitudinal bridge direction.

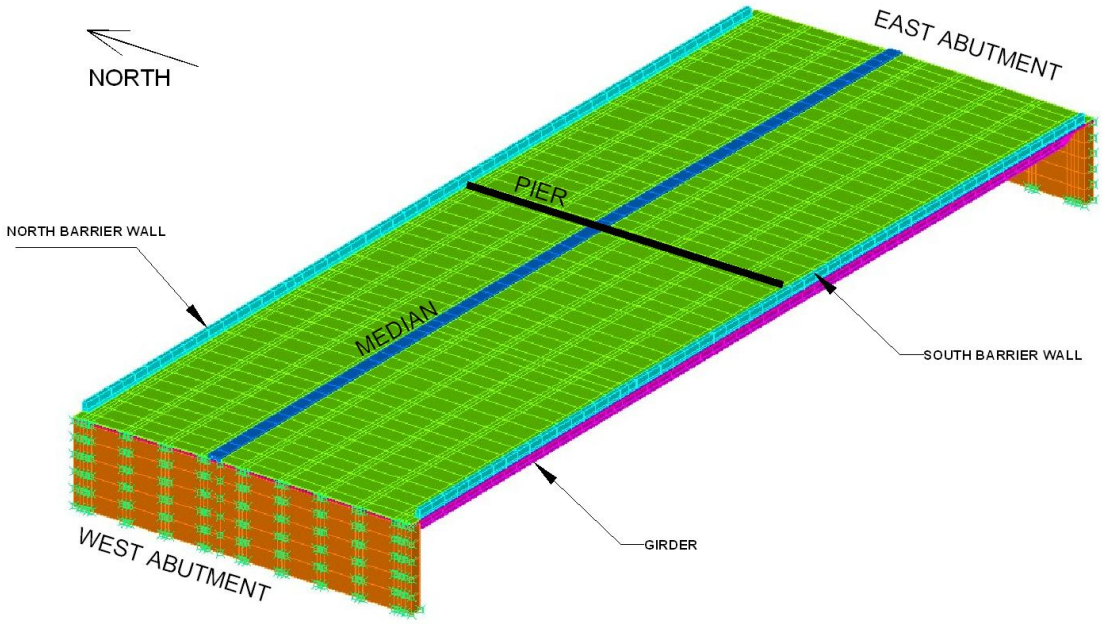

Figure 4.1. Finite element model of the Attridge Drive Overpass, viewed from the southwest.

The effect of the pile foundation was modelled using both rotational and translational spring elements at the bottom of abutments (Siddique 2005). The role of the wing walls was modelled by providing translation fixity at the locations of the steel connectors attaching the abutment and wing walls. To simulate the changing pressure of the backfill soil in response to seasonal contraction and expansion of the bridge, horizontal springs were added to nodes of the backwall of the abutment (Siddique 2005). The spring stiffness was taken from the Siddique model (Siddique 2005). The composite action between concrete deck and steel girders was modelled by applying the constraint condition that the translational degrees of freedom in the horizontal and vertical directions between the nodes on the top flange of the girder and nodes at the soffit layer of the deck must experience identical displacements (Siddique 2005).

4.2.3 Material models

An isotropic, linearly elastic material model was used for the steel (girders and diaphragms), reinforced concrete (abutments, barrier walls, median deck) and asphalt

concrete. The three layers of the bridge deck were modelled as an orthotropic, linearly elastic material to account for direction-dependent flexural cracking in the bridge deck in an approximate fashion without resorting to a nonlinear analysis (Siddique 2005). The relative flexural rigidity of the cracked slab was defined as a percentage of the uncracked (gross) stiffness that was deemed to be maintained in the bridge's current (cracked) state. Material properties for bridge elements at an ambient temperature of 23°C are shown in Table 4.1. These were determined as described below. The material properties for the models at ambient temperatures of 35°C, 20°C, 5°C, -10°C, and -25°C, which were used later in the analyses in Chapter 6, are presented in Appendix A.

The elastic modulus, Poisson's ratio and density of mild steel were assigned to girders and diaphragms. According to the literature, the elastic modulus of mild steel decreases with increasing temperature (Chen et al. 2006; Le et al. 2003). It was assumed that the properties of steel remained constant within the ambient temperature range considered in this research.

The material properties of the Siddique model were adjusted according to the design specifications for the bridge. According to those specifications, the bridge substructure concrete has a compressive strength of 35 MPa. The bridge superstructure concrete is high performance concrete with a nominal compressive strength of 45 MPa.

The assumed variation of reinforced concrete properties with temperature was based on information taken from the literature. The behaviours of normal and high strength concrete in the temperature range of -30°C to 40°C were considered. Shah and Ahmad (1994) found that the compressive strength of normal and high strength concrete increased by 54% and 28.5%, respectively, when the temperature decreased from 20°C to -30°C (see Figure 4.2). The relations between the modulus of elasticity, the compressive strength, $f_c^{'}$, and density of concrete, γ_c, are specified by CSA A23.3-04 (CSA. 2004) as follows:

$$E_{ch} = (3300\sqrt{f_c^{'}} + 6900)\left(\frac{\gamma_c}{2300}\right)^{1.5} \quad , \qquad [4.1]$$

$$E_{cn} = 4500\sqrt{f_c^{'}} \quad , \qquad [4.2]$$

Table 4.1. Material properties of different structural elements of FE model at 23°C.

Elements	Material	Material Model	Material Properties
Wearing Surface	Asphalt Concrete	Isotropic Linear Elastic	E^b=3.65 GPa, υ^c=0.32, ρ^d=2375 kg/m^3, α^e=2.5E-005 /°C
Bridge Deck	High Performance Reinforced Concrete	Orthotropic Linear Elastic	$E_1{}^a$= 24.54 GPa, E_2=3.39 GPa, E_3=24.54 GPa $\upsilon_{12}{}^c$= 0.25, υ_{13}=0.21, υ_{23}=0.2, $G_{12}{}^b$=9.81 GPa, G_{13}=10.14 GPa, G_{23}=1.41 GPa, ρ^d=2400 kg/m^3
Median Deck and Barrier Walls	High Performance Reinforced Concrete	Isotropic Linear Elastic	E^b=28.86 GPa, υ^c=0.2, ρ^d=2400 kg/m^3, α^e=1.2E-005 /°C
Abutments	Normal Strength Reinforced Concrete	Isotropic Linear Elastic	E^b=25.85 GPa, υ^c=0.2, ρ^d =2400 kg/m^3, α^e=1.2E-005 /°C
Girders and Diaphragms	Mild Steel	Isotropic Linear Elastic	E^b=200 GPa, υ^c=0.3, ρ^d =7800 kg/m^3, α^e=1.24E-005 /°C

[a]Direction 1 = Along the width of the overpass
Direction 2 = Along the length of the overpass
Direction 3 = Along the vertical direction of the overpass
[b]E= Young's modulus of elasticity; G= Shear modulus
[e]α= Coefficient of thermal expansion
[c]υ= Poisson's ratio; [d]ρ= Density

where E_{ch} and E_{cn} are the modulus of elasticity of high strength and normal concrete, respectively.

The literature shows that, in the temperature range of 20°C to 40°C, the behaviour of normal and high strength concrete is quite similar. A simplified expression for the temperature dependency of Young's modulus of concrete was suggested by Bangash (1989) as follows:

$$E_T = E\left(1 - \frac{T - 20^o C}{137}\right) \quad , \qquad [4.3]$$

where E is the Young's modulus of concrete taken at 20°C and T is any temperature between 20°C and 50°C.

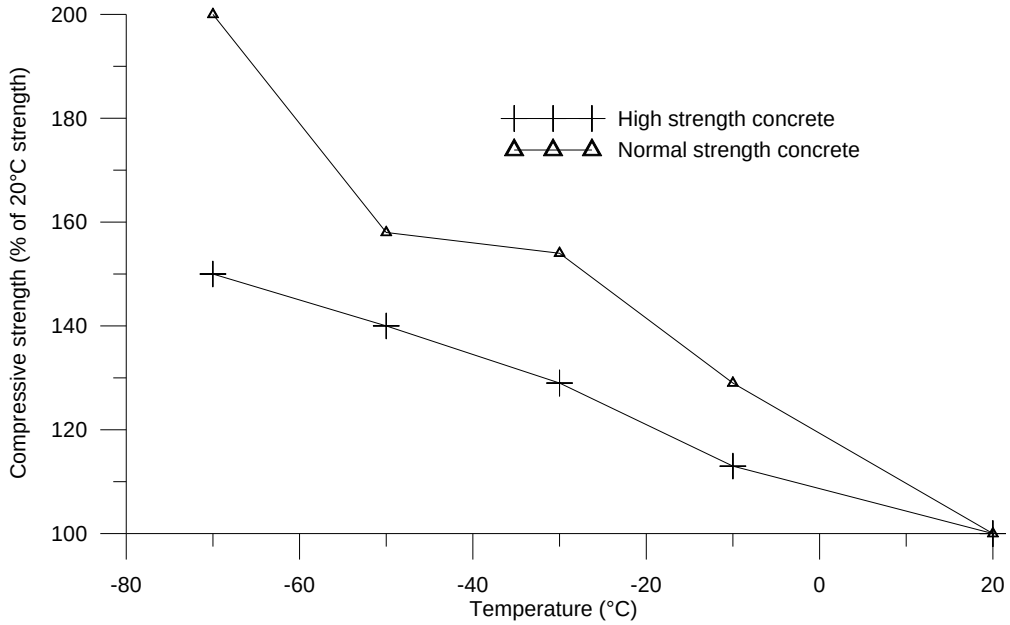

Figure 4.2. Variation of compressive strength for normal and high-strength concrete with temperature (Shah and Ahmad (1994)).

The literature concerning the effect of temperature on Poisson's ratio of reinforced concrete is limited. Marechal (1972) found that Poisson's ratio decreases with increasing temperature. For the ambient temperature range considered in this research, it was assumed that Poisson's ratio of reinforced concrete did not vary with temperature. A Poisson's ratio of 0.22 was used throughout this research.

The asphalt concrete was also modelled as a linearly elastic material whose properties varied with temperature. The mechanistic properties (resilient modulus and Poisson's ratio) of hot mix asphalt material were used in this research. Resilient modulus, the elastic modulus in pavement engineering, characterizes the elastic properties of asphalt concrete subjected to vehicles loads. The variation of the material properties of the asphalt concrete layer with temperature was taken from Watson and Rajapakse (2000), who report results for climatic conditions in the province of Manitoba, where the weather is similar to that in Saskatchewan. Figure 4.3 shows that the resilient modulus of asphalt concrete increases significantly at temperatures below 0°C and experiences a smaller decrease in the above zero temperature range. The variation of Poisson's ratio of the asphalt concrete with temperature was taken from Yoder and Witczak (1975). It is noted that Poisson's ratio tends to decrease with decreasing temperature (Figure 4.4).

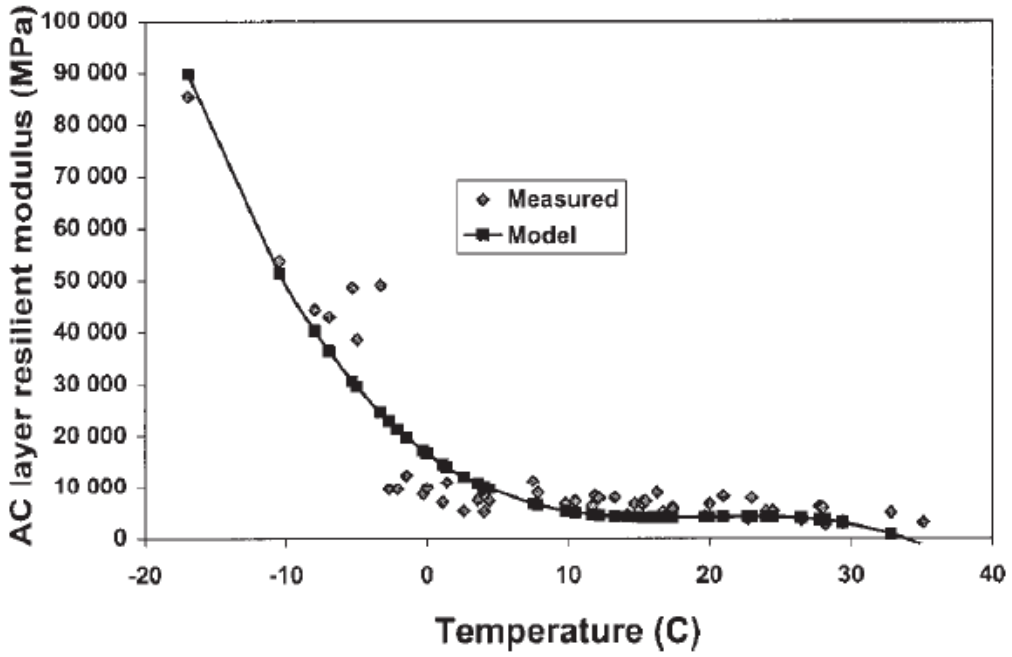

Figure 4.3. Variation of asphalt concrete resilient modulus with temperature (Watson and Rajapakse 2000).

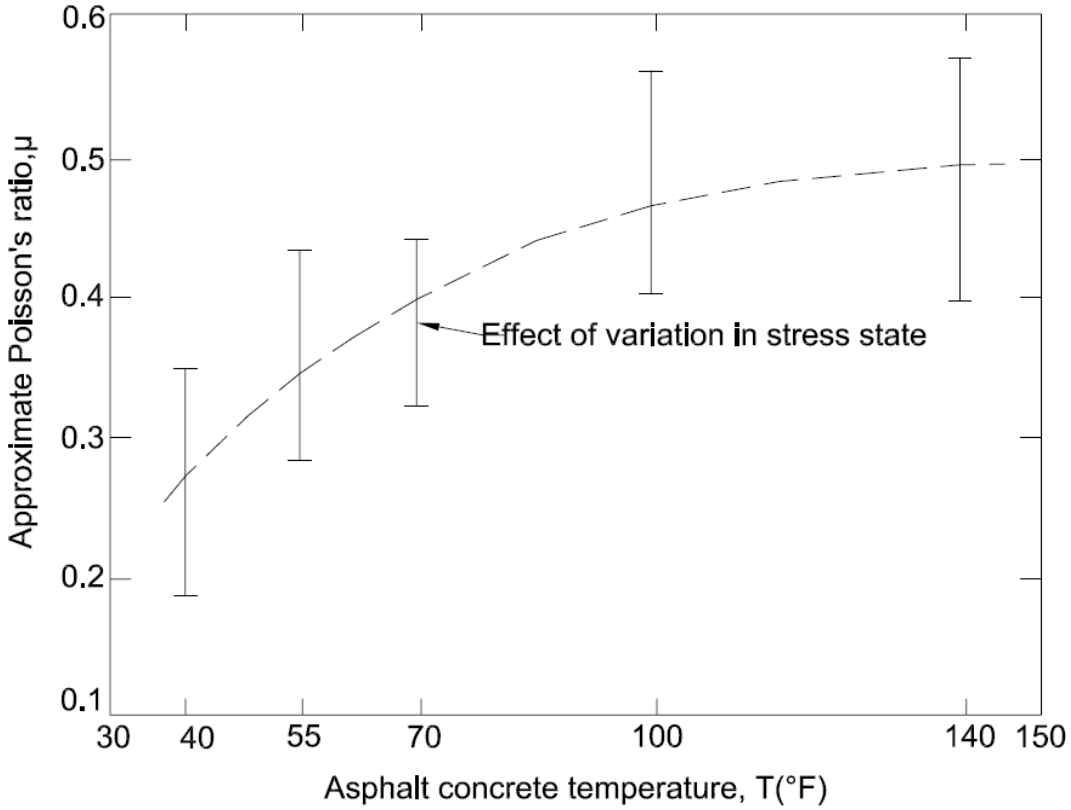

Figure 4.4. Variations of Poisson's ratio of asphalt concrete with temperature (after Yoder and Witczak 1975).

To account for the expansion and contraction of the bridge during daily and seasonal temperature variations, the coefficients of thermal expansion for steel, reinforced concrete, and asphalt concrete were specified as material properties.

4.2.4 Analysis

For the temperature sensitivity study, the material properties of the bridge were varied according to the simulated temperatures. Different models were created for each of the temperature ranges under consideration. In these particular models, the material properties were specified to correspond with the temperature range; in addition, a uniform temperature change was imposed relative to the base condition of 20°C.

When modelling temperature variations, it was assumed that the temperature of the whole bridge was the same as that of the ambient environment. The effect of a temperature gradient through the bridge deck on the dynamic properties of the bridge was not studied. In addition, it was assumed that temperature changes only affected the material properties of the reinforced concrete and asphalt layer, as described in the previous section. The boundary conditions of the bridge were assumed not to change with temperature. Changes in abutment-backfill behaviour and soil-pile interaction in response to changing temperatures were not examined.

The temperature loading was applied to the model for each prescribed temperature range by using a uniform temperature applied to all model elements. It was assumed that the initial (construction) temperature of the bridge was 20°C.

To include the effects of static axial loads due to temperature changes, and the deformed geometry of the bridge due to thermal contraction and expansion, a stressed eigenvalue analysis was performed to extract the natural frequencies, as well as selected vertical components of the mode shapes of the structure.

The natural frequencies and mode shapes of the overpass are calculated using:

$$([\mathrm{k}] - \omega^2[\mathrm{m}])(\phi) = \{0\} \quad , \qquad [4.4]$$

where [m] and [k] are the system mass matrix and stiffness matrix, respectively, (ϕ) is the vector describing a mode shape of the system, and ω is the angular natural frequency associated with that mode shape.

The accelerated subspace-iteration method available in ADINA was used to solve the above equation, yielding the eigenvalues and eigenvectors of the overpass. The first three natural frequencies and vertical components of the corresponding mode shapes along selected longitudinal lines of the bridge were used for subsequent analyses described in later sections.

4.2.5 Model Calibration

The models were calibrated to match the first three natural frequencies and mode shapes extracted from the measured field data. The dynamic properties acquired from several field data sets taken over a wide range of weather conditions were used as the basis for the calibration exercise. Separate models for the temperature ranges of 30° C to 40° C, 20° C to 26° C, 4° C to 7° C, -9° C to -7° C, and -12° C to -5° C were manually calibrated. The model for the "baseline" temperature range of the 20° C to 26° C range was calibrated first.

The first step in the model calibration was to determine the sensitivity of the modal parameters to a variety of variables by adjusting the temperature conditions or material properties. The stiffness of the substructure and superstructure, reinforced concrete and asphalt layers, the stiffness of springs representing the translation and rotation of piles at the bottom of the abutments and translation of backfill material at the back of abutment walls, and the density and Poisson's ratio of reinforced and asphalt concrete materials were subsequently modified to determine the resulting changes to the dynamic response of the bridge model. The changes to the natural frequencies and the mode shapes were then noted to gain an understanding of the significance of each parameter.

The parameters deemed to be temperature independent were: the densities of steel, reinforced and asphalt concrete; the modulus of elasticity of steel; the coefficient of thermal expansion of bridge materials; and Poisson's ratio of normal and high strength reinforced concrete. The parameters identified as being temperature dependent included:

the modulus of elasticity of the abutment backwall, the barrier wall, the median and the asphalt layer; the effective stiffness of the bridge deck; and the Poisson's ratio of the asphalt layer. The stiffness of springs representing soil-structure interaction was found to have little influence on the dynamic response of the model and was therefore assumed to be invariant with temperature.

The model for the 20°C to 26°C range was then calibrated manually by trial and error. The temperature independent parameters were taken from the average values of elastic properties for typical materials (mild steel, hot mix asphalt, normal and high strength reinforced concrete). The temperature dependent parameters identified above were altered in an iterative manner within their expected range of variation taken from existing literature, considering the temperature range on the day the measurements were taken.

The elastic modulus of the deck concrete was altered independently in the transverse, longitudinal and vertical directions in an attempt to accurately represent the reduced relative flexural rigidity in the field structure due to flexural cracking. Careful attention was paid to make sure the smallest flexural rigidity was not reduced below that corresponding to a fully cracked deck cross section.

The adjustment of parameters was implemented until the natural frequencies obtained from the stressed eigenvalue analysis were similar to those from the experimental analysis for the 20°C to 26°C range. The values of material properties of calibrated model for the 20°C to 26°C range are listed in Table 4.1.

The other temperature range models were then calibrated using the same procedure. The temperature independent parameters, as well as those found to have little effect on dynamic response, and the ratios between the stiffness of bridge deck in the three principal orthogonal directions were kept the same in all models. The comparison of dynamic properties extracted from calibrated finite element models and field data are presented in Subsections 6.2.

4.3 SIMULATED DAMAGE SCENARIOS

To determine the changes to the dynamic response of the bridge caused by changes to its structural condition, various damage scenarios were imposed on the finite element model. Damages in the form of small–scale localized deteriorations in the concrete deck were simulated at nine locations, as shown in Figure 4.5, by removing selected elements from the top surface of the bridge deck. Two elements at the same plan location were removed at a time, one from the asphalt layer (90 mm deep) and one (immediately below) from the top layer of the reinforced concrete deck (50 mm deep). The damage states were applied to the south-west quadrant only, and were located longitudinally in the middle of the west span as well as close to the abutment and pier. The locations and dimensions of removed elements are shown in Table 4.2.

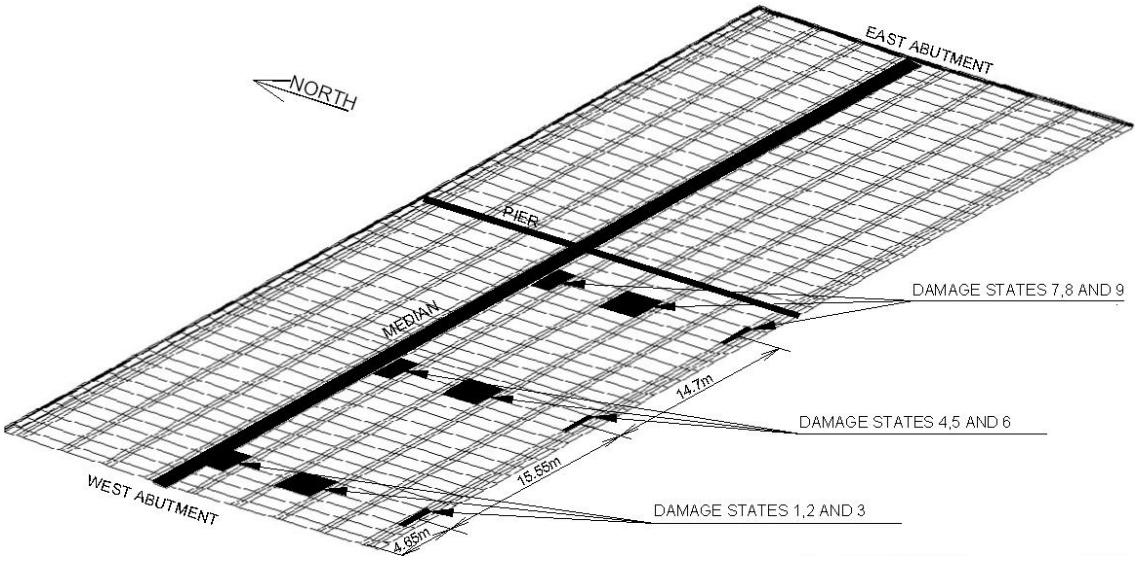

Figure 4.5. Locations of simulated damage states in the bridge deck of the finite element model.

4.4 NORMALIZATION OF MODE SHAPES

The VBDD methods used in this research rely on relative differences between the mode shapes of the structure at different structural conditions. Since the amplitude of a mode shape is arbitrary by definition, the mode shapes must be normalized to a common basis to allow meaningful comparisons. The two mode shapes, one corresponding to an undamaged condition and one corresponding to a damaged condition, must be scaled by

Table 4.2. Locations and dimensions of simulated damage states.

	Damage state								
	1	2	3	4	5	6	7	8	9
Distance from the centre to the west abutment (m)	4.65	4.65	4.65	20.2	20.2	20.2	34.9	34.9	34.9
Distance from the centre to the outside of south barrier wall (m)	0.95	8.85	14.55	0.95	8.85	14.55	0.95	8.85	14.55
Length(m)	2.5	2.5	1.5	2.5	2.5	1.5	2.5	2.5	1.5
Width (m)	0.3	2.5	2.5	0.3	2.5	2.5	0.3	2.5	2.5
Area (m^2)	0.75	6.25	3.75	0.75	6.25	3.75	0.75	6.25	3.75

normalization factors so as to be as similar as possible, so that the changes caused by damage are not masked by changes caused by differences in scaling.

In this project, normalization was achieved by imposing the following constraint on selected portions of individual mode shapes:

$$\sum_{j=1}^{n} \phi_j^2 = 1 \quad , \qquad [4.5]$$

where ϕ in this case represents either the damaged or undamaged mode shape vector under consideration, and n is the number of elements in each vector. This type of normalization is known as unit-norm normalization.

In this research, while unit-norm normalization was used consistently, two normalization schemes were employed, each one considering a different portion of the complete mode shape vector when normalizing. In the first approach, line-by-line normalization was implemented, in which mode shapes were normalized in a piecemeal fashion along each longitudinal line of the bridge independently. In this case, modal amplitudes along each longitudinal line were scaled by a different factor. In the second scheme, referred to as surface normalization, the normalization was carried out using all the extracted modal amplitudes simultaneously, so that a single scaling factor was applied to the entire mode shape.

4.5 FINITE ELEMENT ANALYSES

The finite element analyses were intended to simulate the dynamic behaviour of the bridge under damage and temperature change conditions. Vertical components of the fundamental mode shapes over the surface of the bridge generated by the FE models were compared in these analyses. Three studies were performed to investigate (1) the influence of temperature variations on baseline (undamaged) mode shapes at 35°C, 20°C, 5°C, -10°C, and -25°C, (2) changes in mode shapes due to different damage scenarios at 20°C and at -25°C, and (3) the combined influence of temperature changes and damage scenarios on mode shapes using dynamic properties generated from the damaged structure at -25°C and the pristine structure at 20°C. The detailed results of all the analyses are presented in Chapter 6.

4.6 VIBRATION-BASED DAMAGE DETECTION METHODS

4.6.1 Change in Mode Shape Method

Damage present in a structure causes a localized decrease in stiffness, thus creating a change in the mode shape. The difference between the mode shapes corresponding to pristine and damaged states can be graphically monitored to locate damage in the structure. As mentioned in the previous section, the mode shapes must be normalized to a common basis in order to effectively find the location of damage.

It is expected that the greatest change in mode shape displacement will occur at the location of damage. For the i^{th} vibration mode, if the unit-norm normalized damaged and undamaged mode shape amplitudes are denoted by the vectors $\boldsymbol{\phi}_i^*$ and $\boldsymbol{\phi}_i$, respectively, the change in mode shape $\Delta\boldsymbol{\phi}_i$ caused by damage is simply defined as:

$$\Delta\boldsymbol{\phi}_i = \boldsymbol{\phi}_i^* - \boldsymbol{\phi}_i \quad . \qquad [4.6]$$

The location associated with the largest absolute value in the vector $\Delta\boldsymbol{\phi}_i$ would then represent the most likely location of damage. In this research, only the fundamental mode shapes were considered; in addition, the mode shapes $\boldsymbol{\phi}_i^*$ and $\boldsymbol{\phi}_i$ were defined using

only the vertical components of the modal amplitudes at discrete points on the surface of the bridge deck.

4.6.2 Change in Mode Shape Curvature Method

It is known that the curvature of a beam is directly proportional to the inverse of its flexural stiffness. Thus, a reduction of stiffness associated with damage will, in turn, lead to an increase in curvature. Pandey et al. (1991) demonstrated that the absolute change in mode shape curvature can be a good indicator of damage for beam-like structures.

The change in mode shape curvature of unit-norm normalized damaged and undamaged mode shapes $\boldsymbol{\phi}_i^*$ and $\boldsymbol{\phi}_i$ is calculated by:

$$\Delta\boldsymbol{\phi}_i'' = \left|\boldsymbol{\phi}_i''^* - \boldsymbol{\phi}_i''\right| \quad , \tag{4.7}$$

where $\boldsymbol{\phi}_i''^*$ and $\boldsymbol{\phi}_i''$ are the corresponding damaged and pristine mode shape curvatures for the i^{th} mode of the bridge; here, the determination of absolute values is carried out on each element in the vector. Large peaks in $\Delta\boldsymbol{\phi}_i''$ are indicative of possible damage locations. If multiple modes are used, the sum of the differences in absolute curvature may be used as an indicator of damage, i.e.

$$\Delta\boldsymbol{\phi}_i'' = \sum_{i=1}^{n} \Delta\boldsymbol{\phi}_i'' \quad . \tag{4.8}$$

Since the displacement mode shapes are known at discrete points, the curvature values may be computed using the central difference approximation equation for the second derivative as follows:

$$\phi_{ji}'' = \frac{\phi_{(j+1)i} - 2\phi_{ji} + \phi_{(j-1)i}}{h^2} \quad , \tag{4.9}$$

where h is the average distance between measurement points, ϕ_{ji}'' is the curvature at point j corresponding to the i^{th} mode, and ϕ_{ji} is the unit-norm normalized modal displacement at point j corresponding to the i^{th} mode.

4.6.3 Change in Flexibility Method

The flexibility matrix, **F**, of a structure in undamaged and damaged states may be estimated from a few of the lower vibration modes as follows (Pandey and Biswas 1994):

$$\mathbf{F} \approx \sum_{i=1}^{n} \frac{1}{\omega_i^2} \boldsymbol{\phi}_i \boldsymbol{\phi}_i^T \qquad [4.10]$$

$$\mathbf{F}^* \approx \sum_{i=1}^{n} \frac{1}{\omega_i^{*2}} \boldsymbol{\phi}_i^* \boldsymbol{\phi}_i^{*T} \quad , \qquad [4.11]$$

where ω_i is the angular frequency of the i^{th} mode, n is the number of measured modes, $\boldsymbol{\phi}_i$ is the i^{th} unit-norm normalized mode shape, as above, and asterisks signify properties of the damaged structure. The change in flexibility caused by damage can be obtained from the difference between the respective matrices, i.e.

$$\boldsymbol{\Delta}\mathbf{F} = \mathbf{F}^* - \mathbf{F} , \qquad [4.12]$$

where $\Delta\mathbf{F}$ is the change in flexibility matrix.

For the j^{th} column of this matrix, the parameter $\overline{\delta_j}$ may be defined as the maximum absolute value of the elements in that column, or

$$\overline{\delta_j} = \max\left|\Delta F_{ij}\right| , \; i=1 \ldots m \qquad [4.13]$$

where ΔF_{ij} are elements of $\Delta\mathbf{F}$, and m is the number of points at which the mode shape is defined. The parameter $\overline{\delta_j}$ is a measure of the change of flexibility at point j. The largest value of $\overline{\delta_j}$ is indicative of the location where the change in physical properties (i.e., damage) is located.

4.6.4 Change in Uniform Flexibility Curvature Method

The j^{th} column of the flexibility matrix $\boldsymbol{F}$ calculated by Eq. [4.10] corresponds to the deflected shape assumed by the structure when a unit load is applied at the j^{th} degree of freedom. The sum of all columns of the flexibility matrix thus represents the deflected

shape if a unit load is applied at each degree of freedom simultaneously. This shape is referred to as the uniform load flexibility, and is represented by the vector ***f***.

Zhang and Aktan (1995) indicated that the change in curvature of the uniform load flexibility surface caused by damage could be used to determine the location of the damage. Elements of the uniform flexibility curvature vector, ***f″***, may be calculated from ***f*** again using the central difference approximation as:

$$f_j'' = \frac{f_{j+1} - 2f_j + f_{j-1}}{h^2} \quad , \qquad [4.14]$$

where h is the average distance between measurement locations.

For the current study, the increase in the absolute value of curvature at location j was evaluated as:

$$\Delta f_j'' = \left| f_j''^{*} - f_j'' \right| \quad , \qquad [4.15]$$

where the asterisk indicates the damaged state. The largest positive value of $\Delta \boldsymbol{f''}$ was taken to be indicative of the location of damage.

4.6.5 Damage Index Method

For a structure that can be represented as a beam, Stubbs and Kim (1995) derived a damage index based on the change in modal strain energy at location j for the i^{th} mode as follows:

$$\beta_{ji} = \frac{\left(\int_a^b \left[\phi_i''^{*}(x)\right]^2 dx + \int_0^L \left[\phi_i''^{*}(x)\right]^2 dx \right)}{\left(\int_a^b \left[\phi_i''(x)\right]^2 dx + \int_0^L \left[\phi_i''(x)\right]^2 dx \right)} \times \frac{\int_0^L \left[\phi_i''(x)\right]^2 dx}{\int_0^L \left[\phi_i''^{*}(x)\right]^2 dx} = \frac{NUM_{ji}}{DEN_{ji}} \quad , \qquad [4.16]$$

where $\phi_i''(x)$ and $\phi_i''^{*}(x)$ are continuous mode shape curvature functions for the i^{th} mode in terms of distance, x, along the beam, corresponding to the undamaged and damaged structures, respectively. These are based on the second derivatives of continuous displacement mode shape functions $\phi_i(x)$ and $\phi_i^{*}(x)$. In addition, L is the length of the

beam, and *a* and *b* are the limits of a segment of the beam where damage is being evaluated.

In discrete form, assuming that the spacing between points in the mode shape vectors is uniform, calculation of the damage index is carried out by:

$$\beta_{ji} = \frac{\left(\phi''^{*}_{ji}\right)^2 + \sum_{k=1}^{m}\left(\phi''^{*}_{ki}\right)^2}{\left(\phi''_{ji}\right)^2 + \sum_{k=1}^{m}\left(\phi''_{ki}\right)^2} \times \frac{\sum_{k=1}^{m}\left(\phi''_{ki}\right)^2}{\sum_{k=1}^{m}\left(\phi''^{*}_{ki}\right)^2} = \frac{NUM_{ji}}{DEN_{ji}} \quad , \qquad [4.17]$$

in which variables have been defined previously. If more than one mode is used, a single index for each location, *j*, is formed by:

$$\beta_j = \frac{\sum_{i=1}^{n} NUM_{ji}}{\sum_{i=1}^{n} DEN_{ji}} \quad . \qquad [4.18]$$

Assuming that the set of damage indices for the structure represents a sample population of a normally distributed random variable, a normalized damage indicator is calculated as follows:

$$Z_j = (\beta_j - \mu_\beta)/\sigma_\beta \quad , \qquad [4.19]$$

where μ_β and σ_β are the mean and standard deviation of damage indices, respectively. Damage indices falling two or more standard deviations from the mean (i.e., $Z_j \geq 2$) are indicative of a possible damage location.

CHAPTER 5 . EXPERIMENTAL RESULTS AND DISCUSSION

5.1 INTRODUCTION

In this chapter, the natural frequencies and mode shapes of the Attridge Drive overpass extracted from field measurements are presented. Since the ambient temperatures on the measurement days ranged from -12°C to 40°C, the influence of temperature on the lowest three natural frequencies is also presented. The variability of experimentally measured mode shapes is quantified by calculating the standard deviation at each sensor location. The comparison of measured mode shapes in different temperature ranges was also performed.

5.2 NATURAL FREQUENCIES

The calculated natural frequencies were taken from the peaks on averaged response spectra plots from different loading events during the test period. Since the observed natural frequencies varied from one quadrant to the next by approximately 2 %, only the average natural frequencies for the measurement day are presented here.

The first three natural frequencies were extracted from the field data. Higher natural frequencies were found to be inconsistent throughout the measured data, a finding which is thought to be due to varying vehicular loading.

Table 5.1 lists the measured natural frequencies obtained in different temperature ranges. Figure 5.1 plots the same data with horizontal range indicator bars representing the temperature variation that occurred over the test period. A distinctly bilinear relationship between natural frequency and temperature is apparent for all three modes, a result that is broadly consistent with the findings of Peeters et al. (2001). The location of the break

point on the curves from the present study is somewhat difficult to determine due to the relatively limited data in this range. Natural frequencies for all three modes tend to increase with decreasing temperature. The first, second and third natural frequencies of the overpass were seen to increase by 9.3%, 14.2% and 13.7%, respectively, when the

Table 5.1. Measured natural frequencies at different temperature ranges.

Temperature range (°C)		Natural Frequency		
		1st Mode	2nd Mode	3rd Mode
-12 to -5	Average (Hz)	3.353	3.679	4.33
	COV (%)	1.942	1.770	1.504
-9 to -7	Average (Hz)	3.296	3.571	4.321
	COV (%)	0	1.026	0
4 to 7	Average (Hz)	3.25	3.515	4.166
	COV (%)	0	0	0
20 to 26	Average (Hz)	3.076	3.247	3.833
	COV (%)	0	0.868	0.736
30 to 40	Average (Hz)	3.076	3.223	3.809
	COV (%)	0	0	0

COV = Coefficient of Variation.

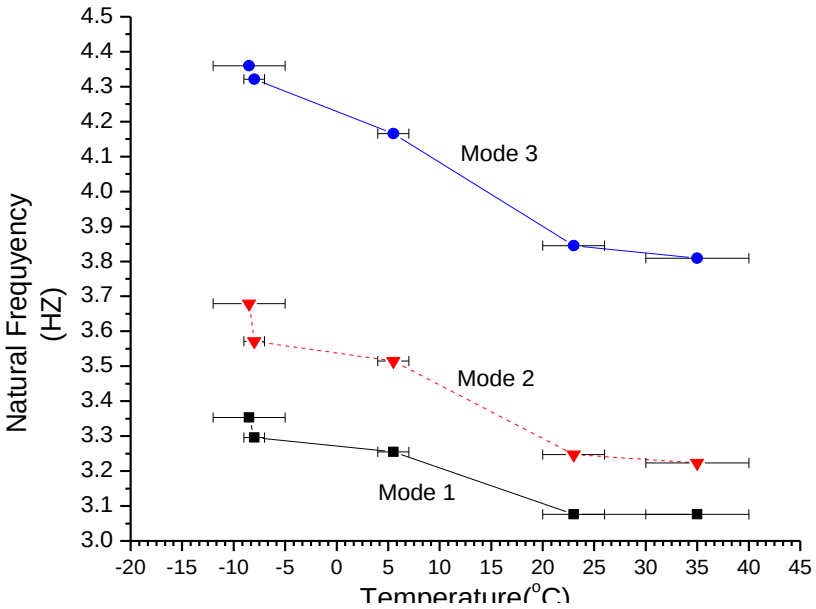

Figure 5.1. The influence of ambient temperature on the lowest three natural frequencies of the overpass.

temperature decreased from 40°C to -12°C; therefore, the higher modes appear to be more temperature sensitive. These changes in natural frequencies were larger than the variations of natural frequencies experienced in any given test day.

It was proposed by Wahab and De Roeck (1997) and Peeters et al. (2001) that the increase in natural frequencies with a reduction in temperature is caused by the increase in the material properties (Young's modulus of the reinforced concrete and asphalt surface) of the bridge components. As will be shown later, the finite element analysis results support this conclusion. Changes in material properties affect the stiffness of the bridge and, therefore, change the natural frequencies.

5.3 MODE SHAPES

Experimental mode shapes were extracted as described in Section 3.5.3 from the measured accelerations at certain points along the two barrier walls of the bridge. Five to six measurement points in each quadrant of the bridge were used to represent the mode shapes along the two barrier wall lines. In this research, only the first three mode shapes were taken into consideration.

The first mode shape in the ambient temperature ranges between -12°C and 40°C is shown in Figure 5.2. The local depression apparent in Fig. 5.2d in the southwest quadrant at 20 m from the west abutment wall is believed to be due to measurement error. As shown in Figures 5.2c and d, the mode shapes for the 4°C to 7°C and 30°C to 40°C temperature ranges are incomplete. Due to technical difficulties, measurements along the south side in the 4°C to 7°C temperature range and along the north side in the 30°C to 40°C temperature range were found to be unusable. Also, one channel malfunctioned on two separate test days; therefore, there are no data at the location of 20 m and 49.3 m from the west abutment for the temperature ranges of -9°C to -7°C (Fig. 5.2b) and -12°C to -5°C (Fig. 5.2e). The modal amplitude at these two locations for the temperature ranges of -9°C to -7°C and -12°C to -5°C were generated using a cubic spline interpolation technique, so that mode shapes for these two temperature ranges could be compared with the mode shapes in the other temperature ranges. The

second and third experimental mode shapes of the bridge in the ambient temperature ranges of from -12°C to 40°C are shown in Appendix B.

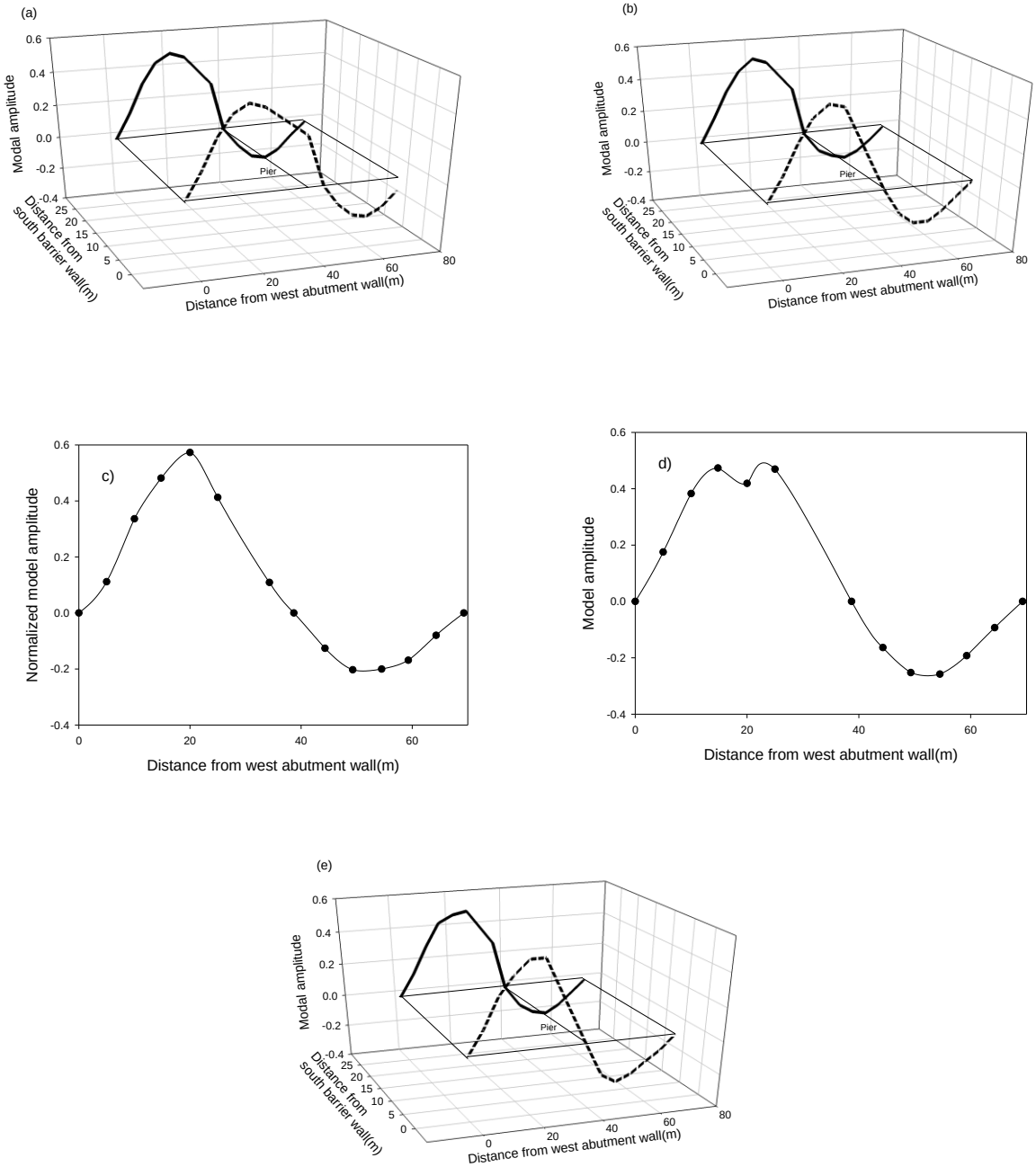

Figure 5.2. First experimental mode shapes of the bridge in the ambient temperature ranges of: (a) 20°C to 26°C; (b) - 9°C to -7°C; (c) 4°C to 7°C (north side of overpass); (d) 30°C to 40°C (south side of overpass); and (e) -12°C to -5°C.

It should be noted that the magnitude of a normalized mode shape is arbitrary; however, the shape itself (i.e., the relative magnitude of one point to another) is more important. Since measurements were taken along the two barrier walls only, it was difficult to tell whether a mode shape was a flexural or a torsional mode. For the same reason, it was also difficult to differentiate between the first and third mode shapes based on measurements along these two lines alone.

5.4 VARIABILITY IN MEASURED MODE SHAPES

Data related to repeated measurements of the overpass taken at the same location and under similar types of excitation during a test day would vary to some extent due to random variations in the loading, measurement errors, external interference, etc.

The variability of the measured mode shapes was quantified by calculating the standard deviation of modal amplitudes from multiple site readings at a given sensor location during a specific measurement day. The modal amplitudes were scaled according to the reference sensor, which was assigned an amplitude of unity. The number of data sets at each sensor location within each quadrant in each temperature range varied from 3 to 15 and was shown in Table 3.2, Table 5.4, Table D.1, and Table D.2. The computed standard deviations were also used in Section 5.5 in a statistical comparison between mode shapes.

Table 5.2 shows the mean and standard deviation of the normalised mode shape amplitudes at each sensor location of the first three modes of the bridge for the 20°C to 26°C temperature range. Figure 5.3 plots the same data with error bars that indicate the standard deviation of the normalised amplitudes. As shown in Table 5.2, if the maximum and the mean values of the standard deviations are considered, for a given mode, the mode shapes along the north side had less uncertainty than mode shapes along the south side. The means and standard deviations of the normalised mode shape amplitudes at each sensor location for the first three modes in the other temperature ranges are presented in Appendix C.

Table 5.2. Variability in the first three measured mode shapes in the temperature range of 20°C to 26°C.

Mode no.			Sensor location from the west abutment (m)									
			5	10	14.8	20	25	44.3	49.3	54.5	59.3	64.3
1st	North Side	Avg	0.50	1.11	1.51	1.68	1.59	-0.41	-0.66	-0.72	-0.57	-0.26
		SD	0.02	0.02	0.05	0.09	0.06	0.07	0.13	0.07	0.08	0.05
	South Side	Avg	0.37	0.86	1.18	1.28	1.19	-0.37	-0.51	-0.52	-0.41	-0.22
		SD	0.06	0.15	0.21	0.28	0.22	0.10	0.13	0.15	0.10	0.06
2nd	North Side	Avg	-0.45	-1.04	-1.45	-1.64	-1.57	0.39	0.63	0.64	0.49	0.22
		SD	0.02	0.04	0.12	0.19	0.12	0.05	0.08	0.10	0.07	0.04
	South Side	Avg	0.55	1.41	2.02	2.34	2.17	-0.44	-0.62	-0.61	-0.46	-0.22
		SD	0.15	0.30	0.48	0.59	0.55	0.14	0.22	0.22	0.16	0.08
3rd	North Side	Avg	0.43	1.03	1.46	1.63	1.60	-0.33	-0.54	-0.55	-0.40	-0.18
		SD	0.04	0.05	0.13	0.16	0.11	0.06	0.08	0.09	0.06	0.03
	South Side	Avg	0.38	1.08	1.34	1.49	1.43	-0.44	-0.65	-0.63	-0.45	-0.19
		SD	0.05	0.15	0.08	0.17	0.15	0.05	0.07	0.09	0.08	0.05

Avg = Average; SD= Standard Deviation.

5.5 COMPARISION BETWEEN MODE SHAPES IN DIFFERENT TEMPERATURE RANGES.

In order to quantify changes in the measured mode shapes with temperature, comparisons between mode shapes were carried out. Percentage changes between unit-norm normalized mode shapes in given temperature ranges and the corresponding unit-norm normalized mode shape in the temperature range of 20°C to 26°C were computed using the following expression:

$$\Delta\boldsymbol{\phi}_T = \frac{\boldsymbol{\phi}_{Ti} - \boldsymbol{\phi}_{T0}}{|\boldsymbol{\phi}_{T0}|} \times 100\,, \qquad [5.1]$$

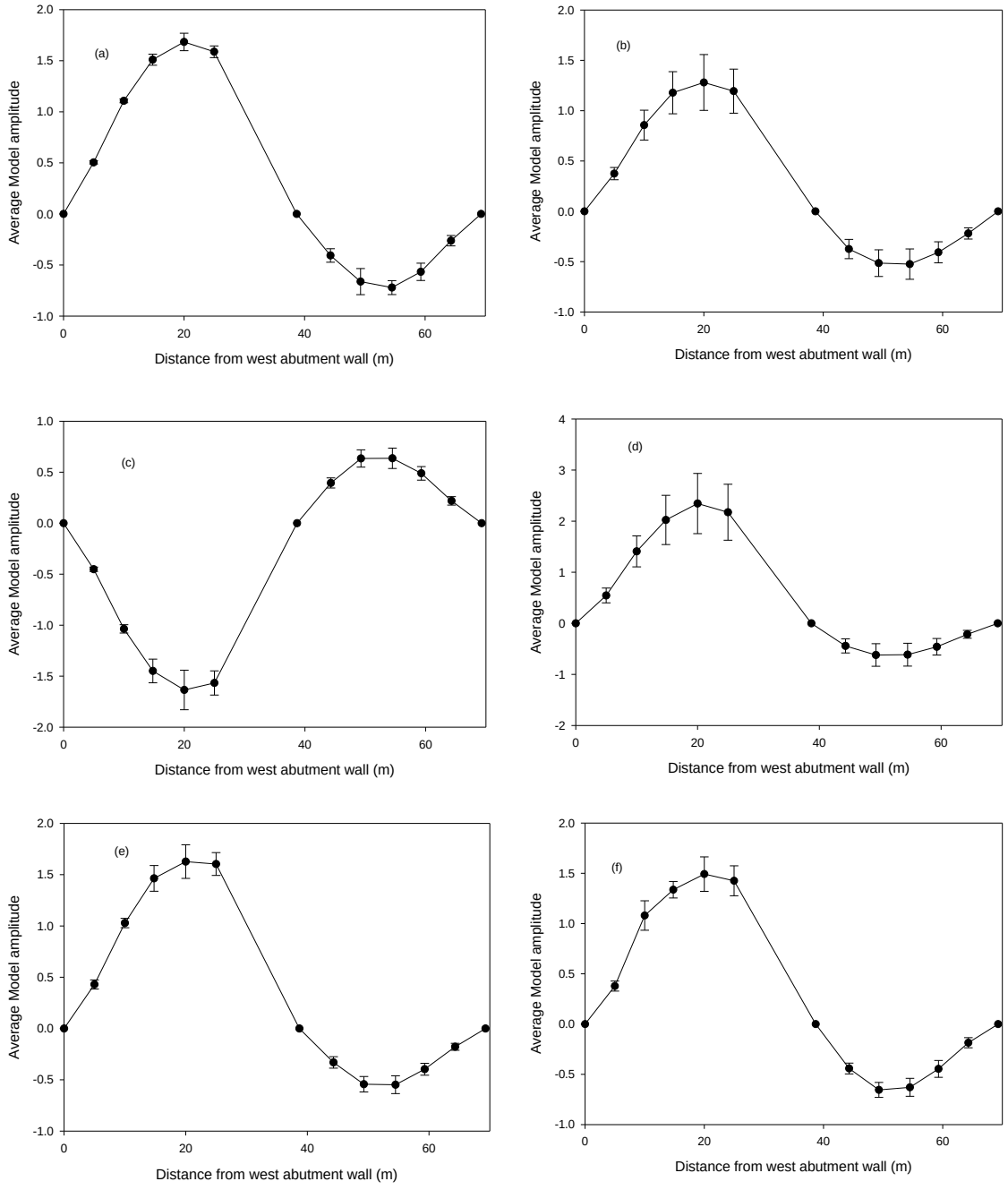

Figure 5.3. Mode shape variability at individual sensor locations of the bridge for the temperature range of 20°C to 26°C: (a) 1st mode shape along the north side; (b) 1st mode shape along the south side; (c) 2nd mode shape along the north side; (d) 2nd mode shape along the south side; (e) 3rd mode shape along the north side; and (f) 3rd mode shape along the south side.

where $\Delta\phi_T$, ϕ_{Ti}, ϕ_{T0} are the vector of percentage changes in mode shapes between two temperature ranges, the mode shape vector for a given temperature range, and the mode shape vector for the temperature range of 20°C to 26°C, respectively.

Figure 5.4 shows the percentage change in mode shapes relative to that in the 20°C to 26°C temperature range; these data are also presented in Table 5.3. The percentage change plots in Figure 5.4 do not appear to show a general trend. If average percentage changes in mode shapes (using absolute values of percentage change) are considered, it is observed that the changes in the mode shapes along the south side are more significant than those along the north side. One exception was noted in the case of percentage changes in first mode shapes for temperature range of -9°C to -7°C compared to that mode shape at 20°C to 26°C, for which the differences in mode shapes on the north side are larger than those on the south side. Also, it appears that changes are larger on the east span than on the west. The mode shapes along the south side for the temperature range -12°C to -5°C show the largest percent decreases (from 1.4% to 68.6%). It is interesting that the largest percentage changes do not necessarily occur for the largest temperature differences.

Statistical analyses using the two-sample Student's t-test (Vining 1998) were used to quantify and compare changes in the measured mode shapes. This procedure tests whether the two samples are likely to be from the same population, based on the mean and standard deviation values for the two samples. The differences between modal amplitude mean values at the same sensor location obtained for two different temperature ranges were examined. It was intended to determine whether the observed changes in the measured mode shapes due to temperature were statistically significant, or whether the differences fell within the bounds of uncertainty.

Consider the modal amplitudes from multiple readings at a given sensor location for two temperature ranges, denoted as sample 1 and sample 2. The variable (t) used in the t-test is defined as:

$$t = \frac{\bar{x}_1 - \bar{x}_2}{s_{\bar{x}_1 - \bar{x}_2}} \quad , \qquad [5.2]$$

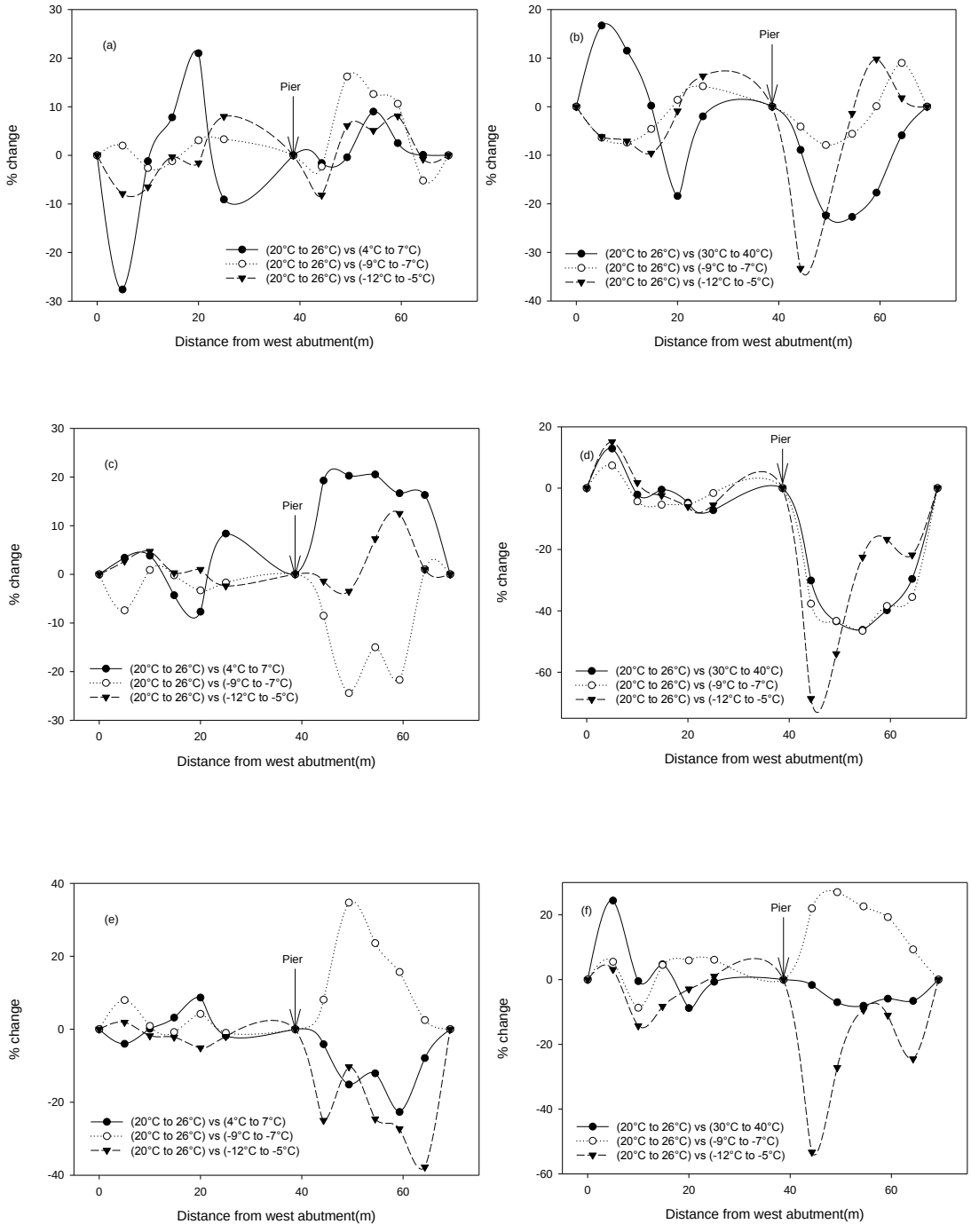

Figure 5.4. Percentage change in mode shapes for given temperature range compared to that mode shape at 20°C to 26°C: (a) 1st mode shape along the north side; (b) 1st mode shape along the south side; (c) 2nd mode shape along the north side; (d) 2nd mode shape along along the south side; (e) 3rd mode shape along the north side; and (f) 3rd mode shape along the south side.

Table 5.3. Percentage differences between mode shapes for a given temperature range and that mode shape for the temperature range of 20°C to 26°C.

Mode no.	Temp range (°C)	Sensor location from the west abutment (m)										Avg
		5	10	14.8	20	25	44.3	49.3	54.5	59.3	64.3	
1st	Percentage change (north side)											
	30 to 40	N/A	N/A	N/A	N/A	N/A	N/A	N/A	N/A	N/A	N/A	
	4 to 7	-27.6	-1.2	7.8	21.0	-9.1	-1.6	-0.4	9.0	2.5	0.1	8.0
	-9 to -7	2.0	-2.6	-1.2	3.1	3.3	-2.3	16.2	12.6	10.6	-5.2	5.9
	-12 to -5	-7.9	-6.5	-0.3	-1.6	8.0	-8.2	6.1	5.1	8.1	-0.8	5.3
	Percentage change (south side)											
	30 to 40	16.7	11.5	0.2	-18.4	-2.0	-8.9	-22.4	-22.7	-17.7	-5.9	12.6
	4 to 7	N/A	N/A	N/A	N/A	N/A	N/A	N/A	N/A	N/A	N/A	
	-9 to -7	-6.4	-7.4	-4.6	1.4	4.2	-4.1	-7.9	-5.6	0.1	9.0	5.1
	-12 to -5	-6.2	-7.1	-9.6	-0.9	6.3	-33.3	-22.4	-1.4	9.8	1.8	9.9
2nd	Percentage change (north side)											
	30 to 40	N/A	N/A	N/A	N/A	N/A	N/A	N/A	N/A	N/A	N/A	
	4 to 7	3.4	3.8	-4.3	-7.7	8.4	19.3	20.3	20.3	16.7	16.3	12.6
	-9 to -7	-7.4	0.9	-0.2	-3.3	-1.7	-8.5	-24.4	-15.0	-21.7	1.0	8.4
	-12 to -5	2.7	4.7	0.3	1.0	-2.4	-1.4	-3.5	7.3	12.5	1.0	3.7
	Percentage change (south side)											
	30 to 40	12.9	-2.1	-0.5	-4.7	-7.2	-30.1	-43.4	-46.2	-39.8	-29.6	21.6
	4 to 7	N/A	N/A	N/A	N/A	N/A	N/A	N/A	N/A	N/A	N/A	
	-9 to -7	7.4	-4.3	-5.4	-5.1	-1.6	-37.7	-43.3	-46.5	-38.4	-35.5	22.5
	-12 to -5	15.1	1.8	-2.4	-6.0	-5.5	-68.6	-54.0	-22.5	-16.7	-21.8	21.4
3rd	Percentage change (north side)											
	30 to 40	N/A	N/A	N/A	N/A	N/A	N/A	N/A	N/A	N/A	N/A	
	4 to 7	-4	-0.1	3.2	8.7	-1.8	-4.1	-15.1	-12.1	-22.	-7.90	8
	-9 to -7	8.0	0.9	-0.8	4.2	-1.0	8.1	34.7	23.6	15.7	2.5	10
	-12 to -5	1.9	-1.8	-2.2	-5.1	-2.0	-25.0	-10.3	-24.6	-27.3	-37.8	13.8
	Percentage change (south side)											
	30 to 40	24.4	-0.5	4.7	-8.8	-0.7	-1.7	-7.0	-8.1	-5.9	-6.6	6.8
	4 to 7	N/A	N/A	N/A	N/A	N/A	N/A	N/A	N/A	N/A	N/A	
	-9 to -7	5.5	-8.7	4.5	5.9	6.1	22.0	27.0	22.6	19.3	9.3	13.0
	-12 to -5	3.1	-14.3	-8.3	-2.9	1.0	-53.3	-27.2	-9.4	-11.0	-24.5	15.5

Avg = Average.

where $\bar{x}_1$ and $\bar{x}_2$ are the mean values of two samples, and $s_{\bar{x}_1-\bar{x}_2}$ is the standard error of the difference between mean values of the two samples:

$$s_{\bar{x}_1-\bar{x}_2} = \sqrt{\frac{s_1^2(n_1-1)+s_2^2(n_2-1)}{(n_1-1)+(n_2-1)} \times (\frac{1}{n_1}+\frac{1}{n_2})} \quad , \qquad [5.3]$$

where n_1 and n_2 are the sizes of the two samples, and s_1 and s_2 are the standard deviations of the two samples.

For the difference between the mean values of two samples to be statistically significant, such that the two samples are unlikely to have come from the same population at the 95% level of significance, their two-tailed P-value should satisfy the criteria that:

$$P < 0.05 \, , \qquad [5.4]$$

where P is the probability that the two samples are from the same population as given by:

$$P = 2 \times [1 - \Phi(t, \nu)] \quad . \qquad [5.5]$$

In this equation, $\Phi(t,\nu)$ is the standard normal cumulative distribution, and ν is the number of degrees of freedom, determined by:

$$\nu = n_1 + n_2 - 2 \quad . \qquad [5.6]$$

Bonferroni correction (Glantz 2005) was used to adjust for multiple comparisons. There were four comparisons with a single control group (the measured mode shape amplitudes within the temperature range of 20°C to 26°C) at each sensor location. Therefore, a P value of 0.05/4 = 0.0125 was used.

Results of the t-test analyses to compare the fundamental mode shape obtained in a given temperature range to that for the temperature range of 20°C to 26°C at each sensor location are shown in Table 5.4. A sample calculation of the Student's t-test and results of t-test analyses for the second and third mode shapes are shown in Appendix D.

As shown in Table 5.4, the differences between modal amplitudes measured in various temperature ranges are mainly statistically insignificant at the 95 percent confidence

level. One exception was noted for the temperature range of 4°C to 7°C, where almost all P-values were smaller than 0.0125. The results from these t-tests clearly show that changes in measured mode shapes due to temperature changes are generally not statistically significant. This suggests that those changes can be explained by variability in the measurements.

Table 5.4. Comparison of 1st mode shapes at various temperature ranges using a t-test analysis.

Temp. range (°C)			Sensor location from the west abutment (m)									
			5.0	10.0	14.8	20.0	25.0	44.3	49.3	54.5	59.3	64.3
30 to 40	South side	t-value	1.15	0.70	-0.17	-1.07`	-0.32	-0.53	-1.53	-1.47	-1.17	-0.29
		P-value	0.30	0.51	0.87	0.33	0.76	0.61	0.16	0.17	0.27	0.78
		DOF	6	6	6	6	6	10	10	10	10	10
4 to 7	North side	t-value	0.37	2.74	5.79	6.75	2.27	-6.20	-5.29	-7.47	-5.06	-4.83
		P-value	0.72	0.02	**0.00**	**0.00**	0.05	**0.00**	**0.00**	**0.00**	**0.00**	**0.00**
		DOF	9	9	9	9	9	9	9	9	9	9
-9 to -7	North side	t-value	-0.21	-0.93	-0.50	N/A	0.05	0.05	N/A	2.10	1.19	-0.15
		P-value	0.84	0.37	0.63	N/A	0.96	0.96	N/A	0.08	0.28	0.89
		DOF	13	13	13	N/A	13	6	N/A	6	6	6
	South side	t-value	0.86	1.60	1.85	N/A	2.35	0.37	N/A	0.24	0.62	1.74
		P-value	0.41	0.13	0.09	N/A	0.04	0.72	N/A	0.82	0.55	0.12
		DOF	13	13	13	N/A	13	9	N/A	9	9	9
-12 to -5	North side	t-value	-2.95	-4.73	-0.19	N/A	2.47	-0.48	N/A	0.39	0.60	-0.03
		P-value	0.02	**0.00**	0.86	N/A	0.04	0.64	N/A	0.71	0.57	0.98
		DOF	8	8	8	N/A	8	8	N/A	8	8	8
	South side	t-value	-2.08	-2.31	-2.19	N/A	-1.55	-0.15	N/A	0.90	1.42	1.24
		P-value	0.07	0.05	0.06	N/A	0.16	0.88	N/A	0.41	0.22	0.27
		DOF	8	8	8	N/A	8	5	N/A	5	5	5

DOF=Degrees of freedom.

P-values in bold denote statistical significance at the 95% level.

CHAPTER 6 . NUMERICAL RESULTS AND DISCUSSION

6.1 INTRODUCTION

This chapter describes the results of the numerical studies conducted to investigate the influence of temperature variation and damage – independently and together – on the natural frequencies and mode shapes. The results of finite element (FE) model calibrations and a comparison of FE and experimental natural frequencies and mode shapes in different temperature ranges are first presented. Next, influences of temperature variation and damage on the extracted modal properties are evaluated first separately and then in combination. Finally, the changes in mode shapes due to temperature changes and damage are compared and attempts to distinguish one from the other by using four vibration-based damage detection methods (VBDD) (change in mode shape curvature, change in flexibility, change in uniform flexibility curvature, and damage index methods) and Fast Fourier Transform (FFT) analyses are described.

6.2 MODEL CALIBRATION

Separate models for the temperature ranges of 30°C to 40°C, 20°C to 26°C, 4°C to 7°C, -9°C to -7°C, and -12°C to -5°C were manually calibrated so that their natural frequencies and mode shapes matched those measured experimentally in the same temperature ranges. Details regarding model calibration procedures and adjustments for temperature were provided in Section 4.2.5. These separately calibrated models were not used for subsequent analyses, but facilitated a more accurate estimate of the temperature-dependent material properties in the ranges for which experimental data were available. The material properties obtained for the calibrated models are in Appendix A.

The natural frequencies calculated using the FE models are shown in Table 6.1 along with those measured within the different temperature ranges. As can be seen, there is a good agreement between experimental and FE natural frequencies, with a maximum error between the two of 4.3% for the third mode, and less than 2% error for the fundamental mode over all temperature ranges.

The first three mode shapes calculated from the calibrated finite element model at 23°C are shown in Figure 6.1. It is apparent that the first mode is a flexural mode, the second mode is a torsional mode, and the third mode involves combined flexure and torsion. The experimental and FE mode shapes along the two barrier walls in the temperature ranges of 20°C to 26°C and -9°C to -7°C are shown in Figure 6.2 and Figure 6.3, respectively, again suggesting consistently close agreement between the numerical models and the field measured data. Comparisons of the experimental and FE mode shapes in other temperature ranges are presented in Appendix E.

Table 6.1. Comparison of FE and experimental natural frequencies in different temperature ranges.

Temperature (°C)		Natural Frequency (Hz)			Relative error (%)		
		1st mode	2nd mode	3rd mode	1st mode	2nd mode	3rd mode
-12 to -5	Experiment	3.353	3.678	4.33	-0.3	-1.5	4.3
	FE Model	3.344	3.623	4.518			
-9 to -7	Experiment	3.296	3.571	4.321	0.4	0.08	2.8
	FE Model	3.308	3.574	4.446			
4 to 7	Experiment	3.25	3.515	4.166	-1.8	-2.98	-0.16
	FE Model	3.192	3.41	4.159			
20 to 26	Experiment	3.076	3.247	3.833	0.22	0.43	1.9
	FE Model	3.083	3.261	3.906			
30 to 40	Experiment	3.076	3.223	3.809	-0.91	-0.18	1.4
	FE Model	3.048	3.217	3.863			

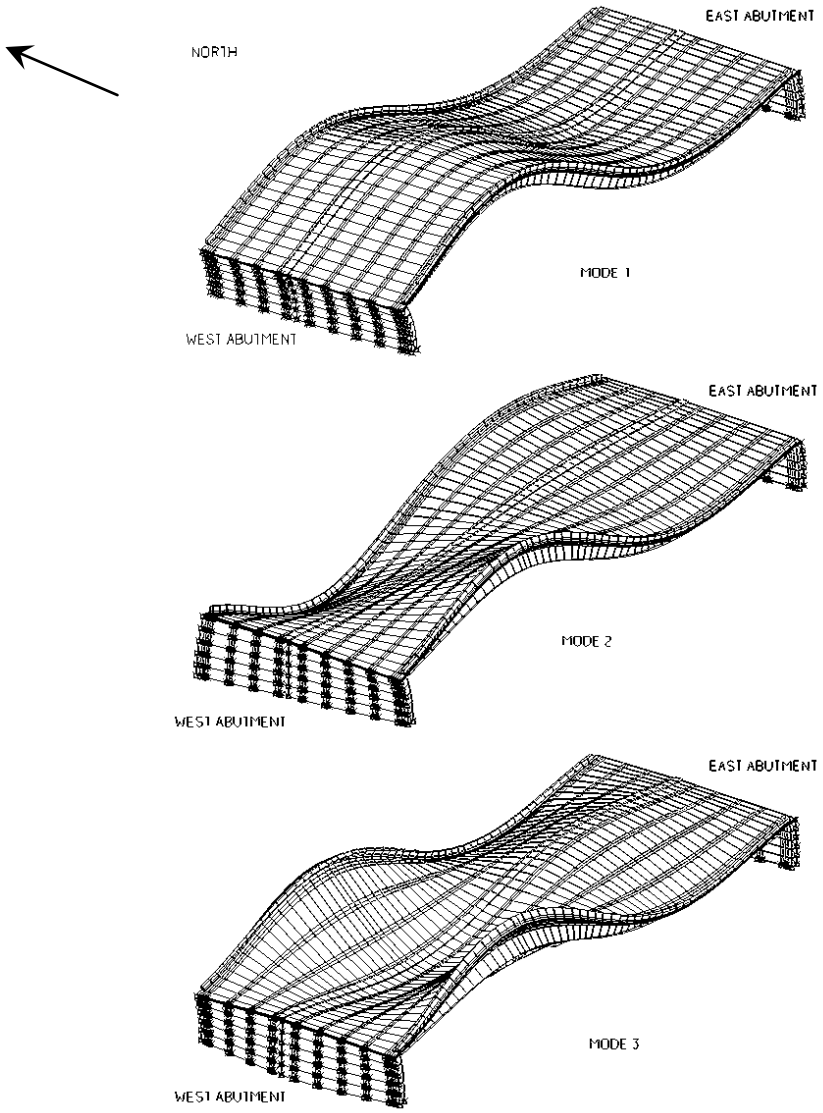

Figure 6.1. Mode shapes generated from the finite element model for an ambient temperature of 23°C.

The Modal Assurance Criterion (MAC) (Ewins 2000) was used as a quantitative comparison of the three first mode shapes determined experimentally and numerically. The MAC value of two mode shape vectors $\boldsymbol{\phi}^{A}$ and $\boldsymbol{\phi}^{B}$ (in this case, the experimental and numerical mode shapes, respectively) is defined as:

$$MAC_{A,B} = \frac{\left|\sum_{i=1}^{n} \boldsymbol{\phi}_i^{A} \boldsymbol{\phi}_i^{B}\right|^2}{\sum_{i=1}^{n} \left(\boldsymbol{\phi}_i^{A}\right)^2 \times \sum_{i=1}^{n} \left(\boldsymbol{\phi}_i^{B}\right)^2} \quad , \qquad [6.1]$$

where *n* is the number of points at which the two mode shapes are compared and *i* indicates an element in the vectors (corresponding to a particular sensor location). The MAC value indicates the degree of correlation between the two modes and varies from 0 to 1, with the value of 0 indicating that the two vectors are orthogonal and the value of 1 indicating that the two vectors are identical.

The MAC values comparing the first three numerical and experimental modes shapes along the north and south barriers walls in various temperature ranges are shown in Table 6.2. As seen, all MAC values are over 0.94, indicating a very good agreement between the measured and numerical mode shapes.

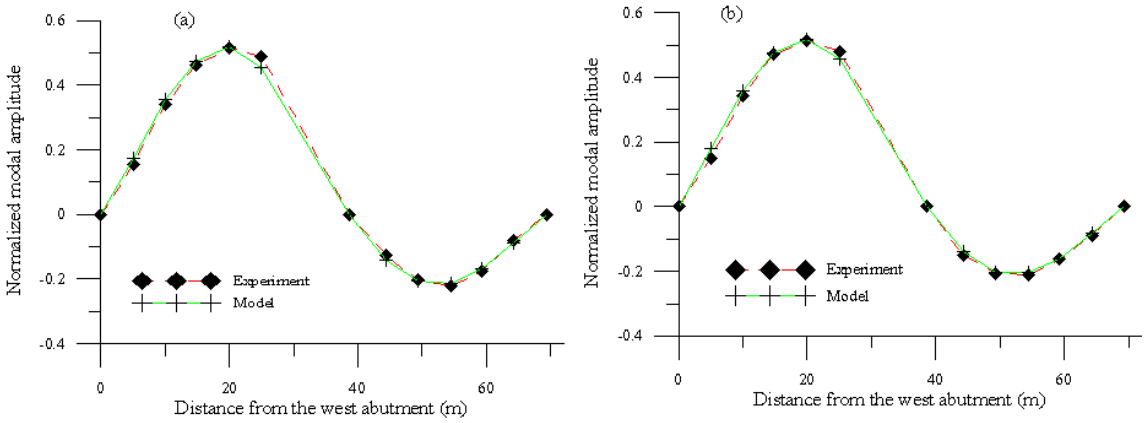

Figure 6.2. Comparison of measured and numerical fundamental mode shapes for the temperature range of 20°C to 26°C: (a) along the north barrier wall; and (b) along the south barrier wall.

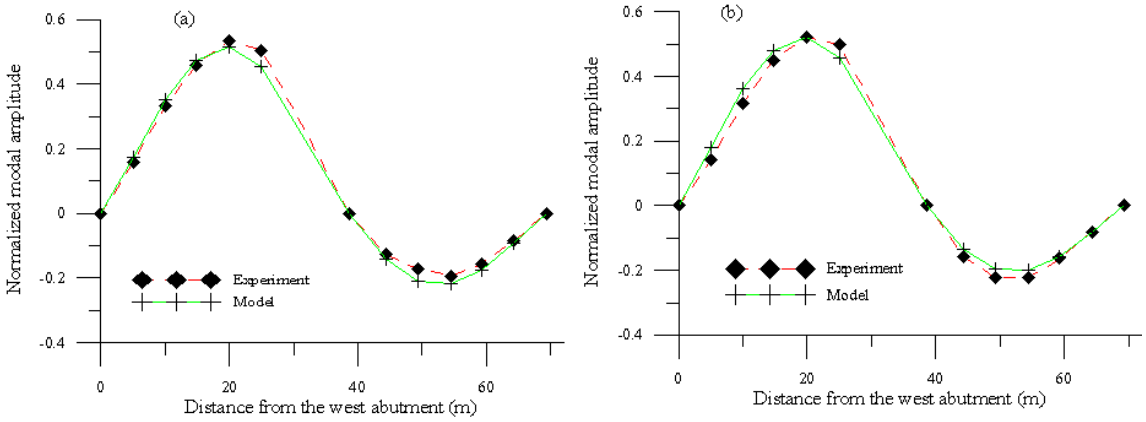

Figure 6.3. Comparison of measured and numerical fundamental mode shapes for the temperature range of -9°C to -7°C: (a) along the north barrier wall; and (b) along the south barrier wall.

Table 6.2. Modal Assurance Criterion (MAC) values, comparing numerical and experimental mode shapes.

Temperature (°C)		Modal Assurance Criterion		
		1st mode	2nd mode	3rd mode
-12 to -5	North side of bridge	0.944	0.951	0.944
	South side of bridge	0.969	0.980	0.960
-9 to -7	North side of bridge	0.965	0.950	0.958
	South side of bridge	0.988	0.990	0.988
4 to 7	North side of bridge	0.994	0.997	0.996
20 to 26	North side of bridge	0.978	0.975	0.974
	South side of bridge	0.998	0.974	0.998
30 to 40	South side of bridge	0.982	0.998	0.994

The high MAC values and good agreement between the experimental and numerical dynamic parameters illustrate that the calibrated finite element models closely represent the dynamic response of the bridge. On that basis, it was concluded that the FE model dynamic results could be viewed with a satisfactory level of confidence.

6.3 INFLUENCE OF TEMPERATURE ON MODE SHAPES

The variations of ambient temperature between an initial temperature 20°C and four different final temperatures (35°C, 5°C, -10°C, and -25°C) were simulated using the FE models that had been calibrated at 20°C, 35°C, 5°C, and -10°C. The temperature dependent material properties were first adjusted to match those taken from the literature corresponding to the desired final temperatures. Then temperature loads were applied to bring the models from 20°C to the final temperatures (i.e., a specified temperature change was imposed on all elements of the model uniformly).

Only the vertical components of the fundamental mode shapes over the surface of the bridge generated by the FE models were used to assess the influence of temperature. Mode shapes were normalized by two different methods, line-by-line and surface normalization, as described in Chapter 4, before being analysed. The difference between the mode shape generated at a certain temperature and the mode shape at 20°C was obtained by subtracting the normalized mode shape vector corresponding to each

longitudinal line at 20°C from the corresponding vector generated at the given temperature.

Spatial distributions of the mode shape change caused by an increase in temperature from 20°C to 35°C are shown in Figure 6.4. It is apparent that when the temperature rose from 20°C to 35°C, the magnitudes of the changes in the fundamental mode shape over the bridge surface were small. The maximum amplitude of the fundamental mode shape normalized line-by-line was 0.00123, whereas the maximum change was 2.93%. For surface normalization, the maximum change was 22 %. The low level of change is expected because the changes in the stiffness of the asphalt layer and concrete as the temperature increases from 20°C to 35°C are relatively small. As seen in Figure 6.4, for both normalization methods, the changes vary smoothly over the bridge deck surface, and feature undulations with wavelengths approximately corresponding to the deck span. Mode shape changes for surface normalization were seen to exhibit more variation across the width of the bridge deck.

The spatial distributions of the mode shape change caused by a decrease in temperature from 20°C to -25°C and from 20°C to -10°C are shown in Figure 6.5 and Figure 6.6, respectively. These distributions differ from those in Fig. 6.4 in that changes are seen to vary significantly in both the longitudinal and transverse directions, while for increasing

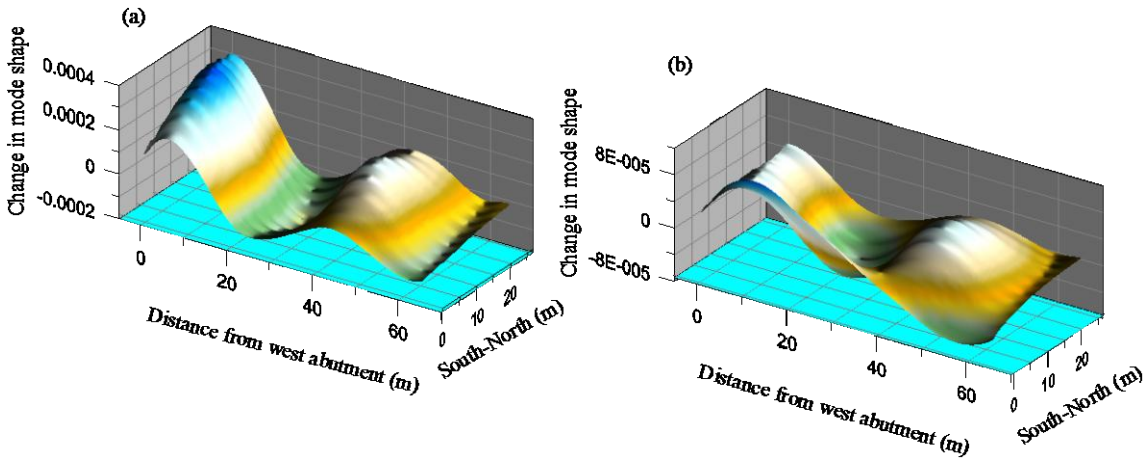

Figure 6.4. Distributions of the change in mode shape over the surface of the deck caused by an increase in temperature from 20°C to 35°C using: (a) line-by-line normalization; and (b) surface normalization.

temperatures (Fig. 6.4), the changes are, relatively speaking, more consistent transversely and varying primarily in the longitudinal direction. As shown in Fig. 6.5, the patterns of changes produced by both normalization methods when the temperature decreased from 20°C to -25°C are similar to those in Fig. 6.6 corresponding to a decrease in temperature from 20°C to -10°C. However, the patterns of changes produced using line-by-line normalization are notably different from those produced using surface normalization, in that they feature more undulations with shorter wavelengths.

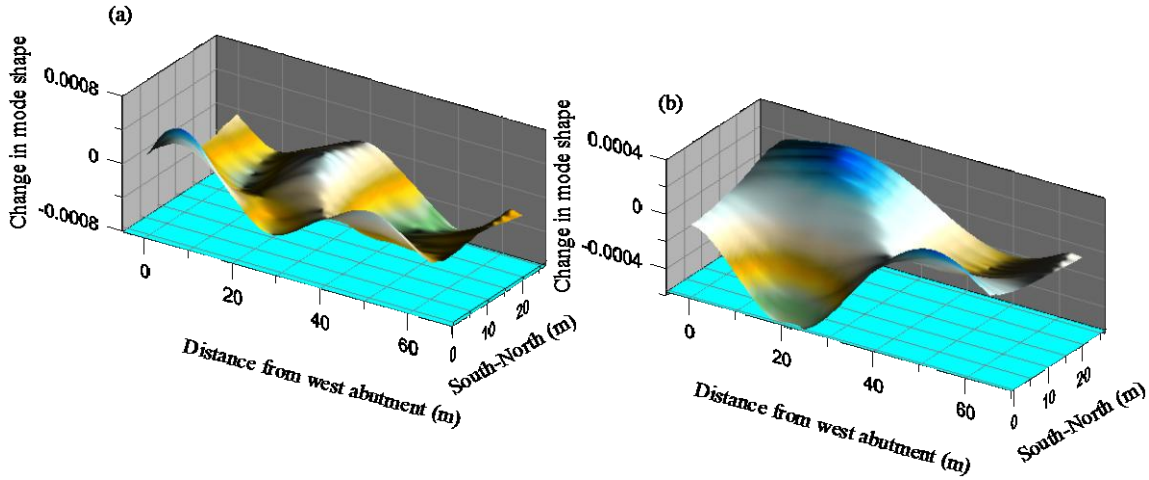

Figure 6.5. Distributions of the change in mode shape over the surface of the deck caused by a decrease in temperature from 20°C to -25°C: (a) using line-by-line normalization; and (b) using surface normalization.

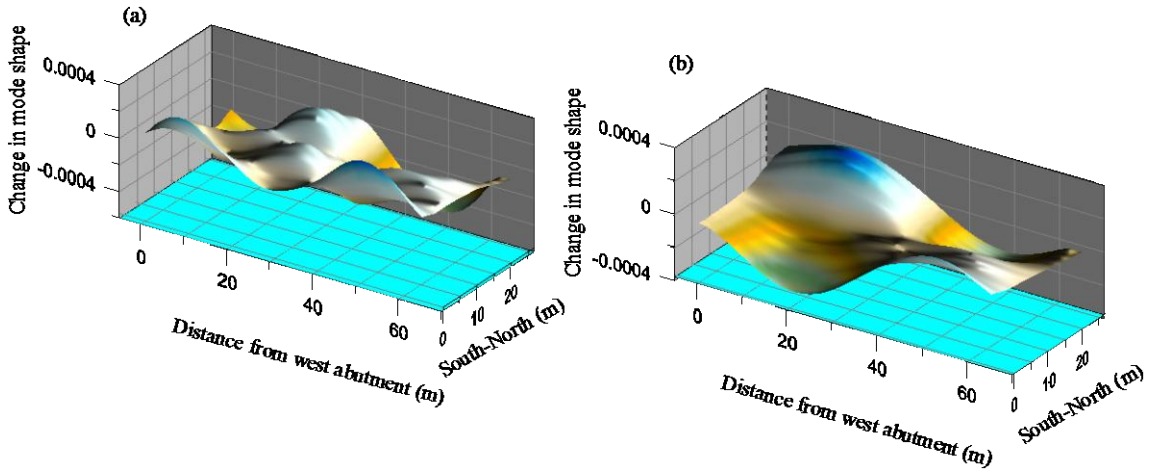

Figure 6.6. Distributions of the change in mode shape over the surface of the deck caused by a decrease in temperature from 20°C to -10°C: (a) using line-by-line normalization; and (b) using surface normalization.

In order to illustrate changes that could be measured along longitudinal lines where instrumentation could be readily installed during normal operation of the bridge, the change of normalized mode shapes along the north and south edges of the deck, as well as along the median, are shown in Figure 6.7, corresponding to a decrease in temperature from 20°C to -25°C. In general, the changes are again seen to vary smoothly with wavelengths roughly equal to the deck spans when surface normalization is used, and somewhat shorter wavelengths when line-by-line normalization is used. The changes of normalized mode shapes along the three longitudinal lines due to a decrease or an increase in temperatures from 20°C to other temperatures are shown in Appendix F.

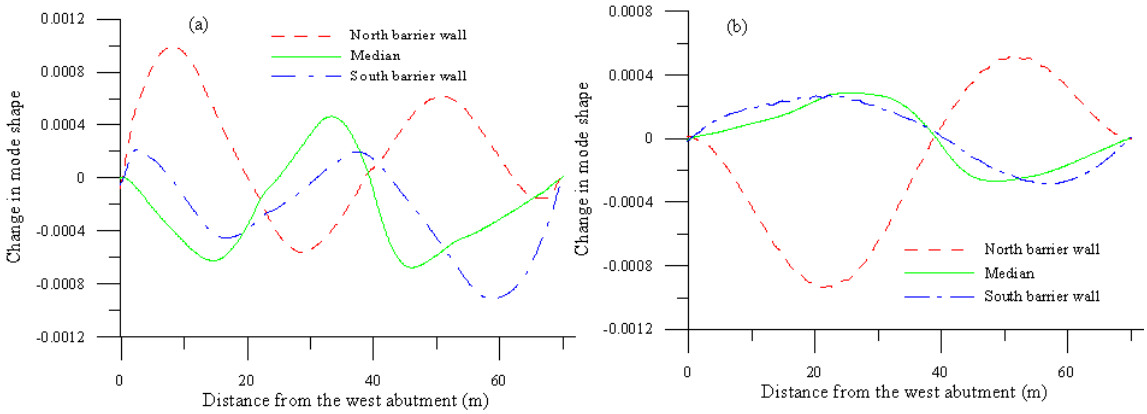

Figure 6.7. Distributions of changes in mode shape along three longitudinal lines, corresponding to a decrease in temperature from 20°C to -25°C: (a) using line-by-line normalization; and (b) surface normalization.

A more detailed comparison of the changes in mode shapes caused by different temperature changes was undertaken. Percentage changes in mode shapes along three longitudinal lines (north barrier wall, median, and south barrier wall) relative to the maximum normalized amplitude over the corresponding lines at 20°C were computed. Figure 6.8 and 6.9 show the percentage changes in mode shapes caused by all investigated temperature variations calculated using line-by-line and surface normalization, respectively. These figures indicate small changes (less than 1.5% for line-by-line normalization and less than 4.9% for surface normalization) along the three sensor lines. The most significant changes in mode shapes occurred at the middle points of the spans, and the differences in mode shapes became larger when the temperature changes were larger. The distributions of relative changes calculated using surface

normalization (Fig. 6.9) were not only larger in magnitude, but also exhibited longer wavelengths than the corresponding distributions calculated using line-by-line normalization (Fig. 6.8).

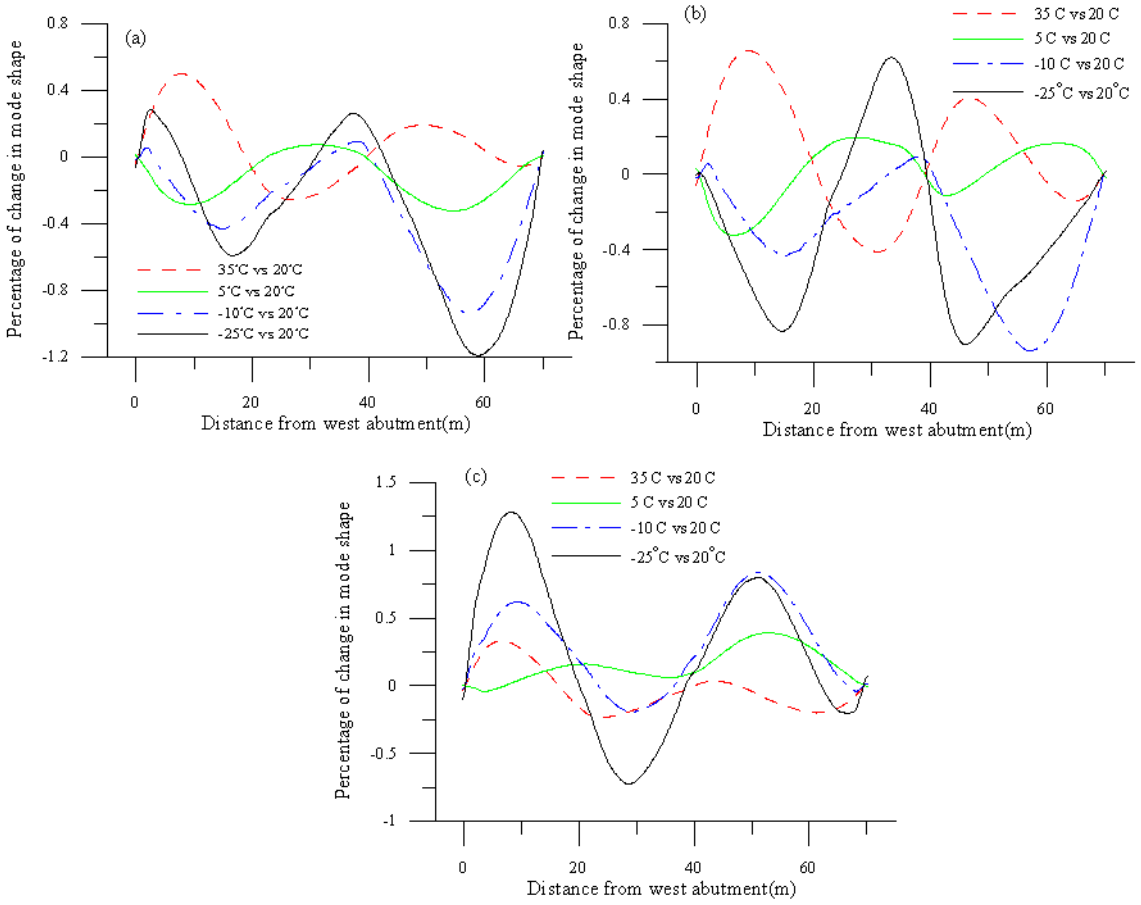

Figure 6.8. Percentage change in fundamental mode shape caused by temperature variation relative to 20°C using line-by-line normalization : (a) along the north barrier wall; (b) along the south barrier wall; (c) and along the median.

6.4 DAMAGE-INDUCED CHANGES IN DYNAMIC PROPERTIES

6.4.1 Overview

As indicated in Section 4.3, nine states of damage were introduced into the finite element models at ambient temperatures of 20°C and -25°C by removing two adjacent elements at a time from each of the asphalt layer and the top layer of reinforced concrete for a total thickness of 160 mm. This subsection presents the results for only three damage states, which are described below. These three damage cases were selected as

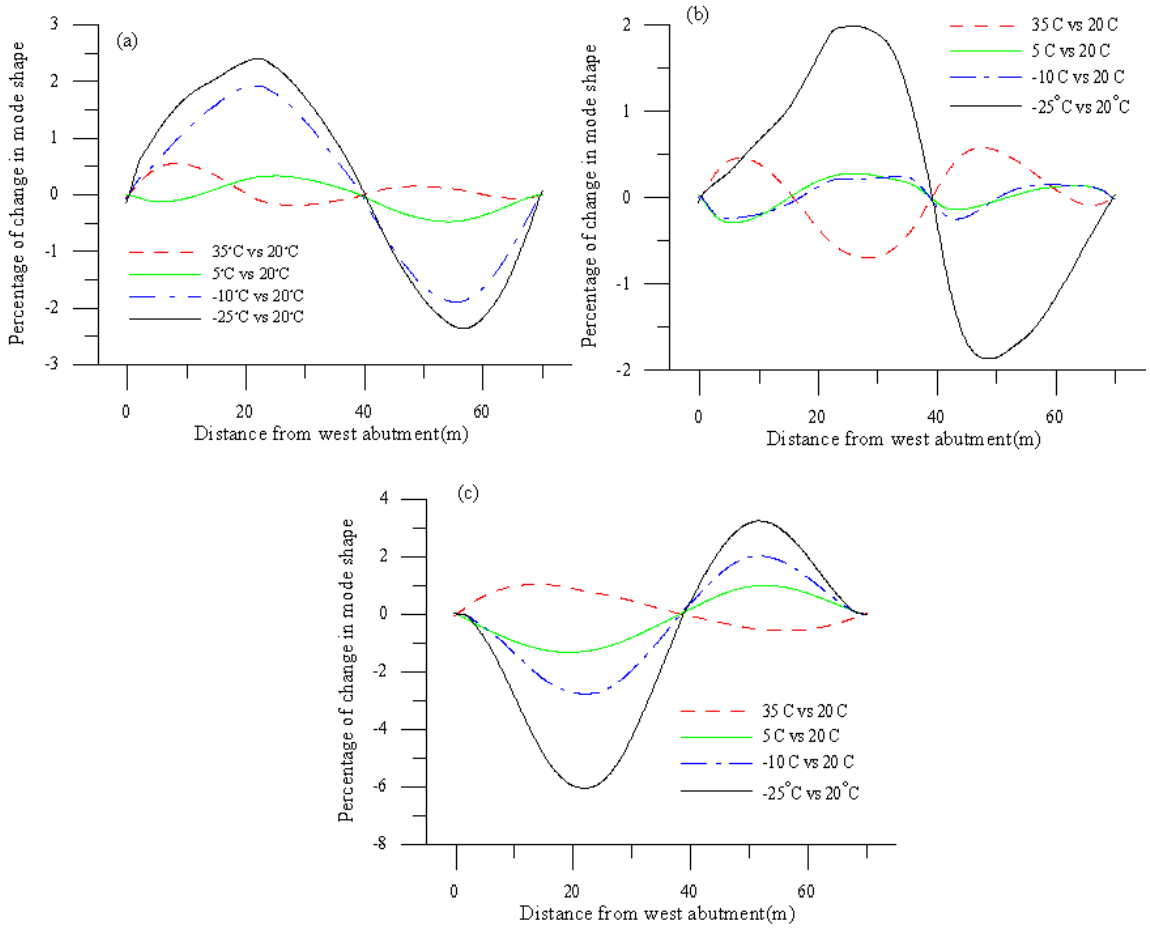

Figure 6.9. Percentage change in fundamental mode shape caused by temperature variation relative to 20°C using surface normalization: (a) along the north barrier wall; (b) along the south barrier wall; and (c) along the median.

they encompassed the trends observed in the remaining cases. Results for additional damage states are provided in Appendix G.

As shown in Fig. 6.10, damage state 1 was located adjacent to the west abutment and the south barrier wall and had a plan area of 0.75 m^2. Damage state 6 was located near the median and 20.2 m from the west abutment and had a plan area of 3.75 m^2. Damage state 8 was located midway between the south barrier wall and median, 3.06 m from the pier in the west span, with a plan area of 6.5 m^2.

In addition to considering mode shapes over the entire surface of the deck, it was also assumed that the bridge would be in operation during measurement, so that sensor locations (simulated measurement points) were restricted to three longitudinal lines

along the north edge, south edge, and median of bridge deck. The mode shapes used in the analysis were the fundamental mode shapes generated from the calibrated models.

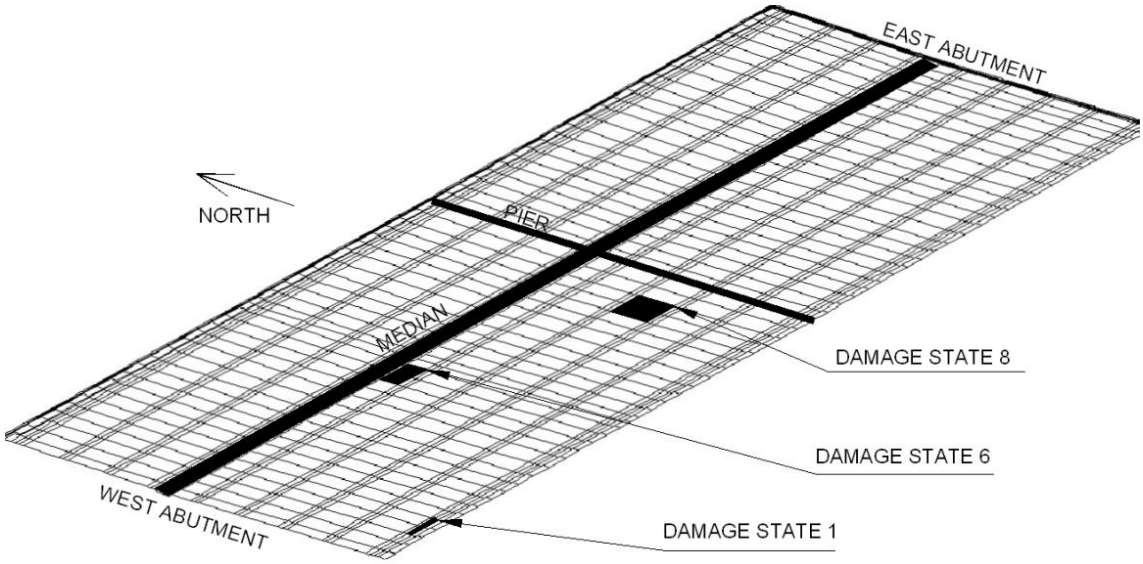

Figure 6.10. Schematic of finite element model showing locations of simulated damage.

6.4.2 Damage-induced Changes in Natural Frequency

The changes in the first three natural frequencies produced by the introduction of all damage scenarios considered in this research at ambient temperatures of both 20°C and -25°C were insignificant. The magnitudes of damage-induced frequency changes were limited to the fourth decimal place and were therefore several orders of magnitude smaller than those produced by temperature changes (see Table 6.1). Therefore, natural frequency change is not a suitable damage detection parameter for the type of damage considered here if the dynamic measurements are to be taken over varying temperature ranges.

6.4.3 Damage-induced Changes in Mode Shape

For damage state 8, the spatial distributions of mode shape changes over the entire surface of the bridge are shown in Figure 6.11. As seen in the Figure 6.11, line-by-line normalization (Figure 6.11a) produced a prominent downward peak at the location of removed elements, while surface normalization (Figure 6.11b) did not show any obvious indication of the damage location. This suggests that the surface normalized plots were

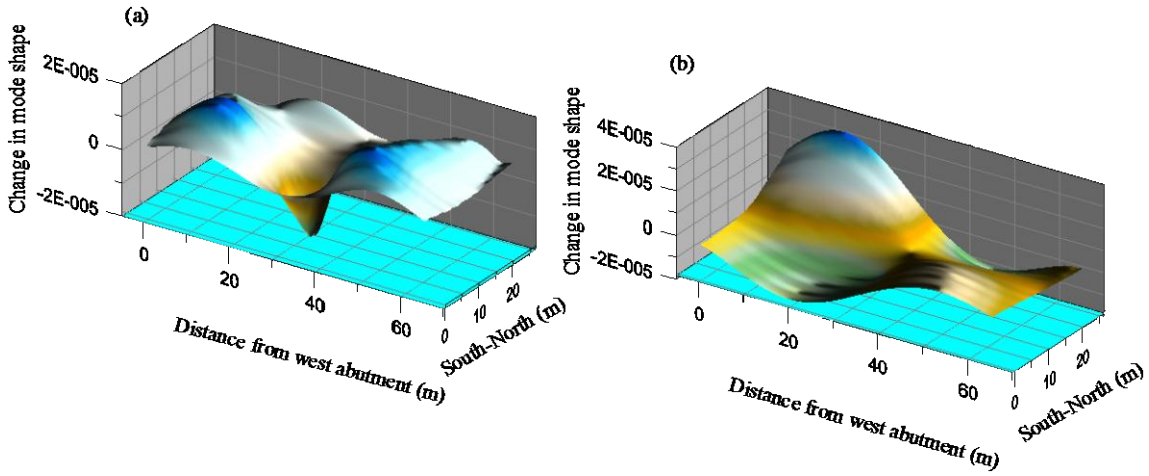

Figure 6.11. Spatial distributions of changes in mode shape caused by damage state 8 at an ambient temperature of 20°C: (a) calculated using line-by-line normalization; and (b) surface normalization.

less sensitive in detecting the location of damage than line-by-line normalized plots, a finding that can be explained by the difference between the two normalization methods.

In surface normalization, single scale factor was applied for the entire model, while in line-by-line normalization each longitudinal line was scaled by a different factor. Line-by-line normalization therefore produces a closer fit between the damaged and baseline mode shape over any given portion of the deck, thus emphasising small, localized mode shape changes caused by damage.

Plots of mode shape changes along three longitudinal lines (possible sensor locations) spanning the bridge length are shown in Figure 6.12 for damage state 8. As seen in Figure 6.12a and Figure 6.12b, neither line-by-line nor surface normalization produced a noticeable peak at the damage location. In this case, since damage was located relatively far from the measurement lines, the change in mode shape did not provide an indication of the location of the damage site. Thus, level 2 damage detection (i.e., damage localization) would not be possible. However, the fact that there were significant continuous waveforms present in the change of mode shape plots may be sufficient evidence to indicate that damage was, at least, present (level 1 damage detection).

The spatial distributions of mode shape changes due to damage state 6 for an ambient temperature of 20°C using line-by-line and surface normalization are shown in

Figure 6.13a and Figure 6.13b, respectively. In the immediate vicinity of the simulated damage, Figure 6.13a features a distinct, narrow positive peak centred on the damage location. Figure 6.13b also shows a small upward hump at the location of damage.

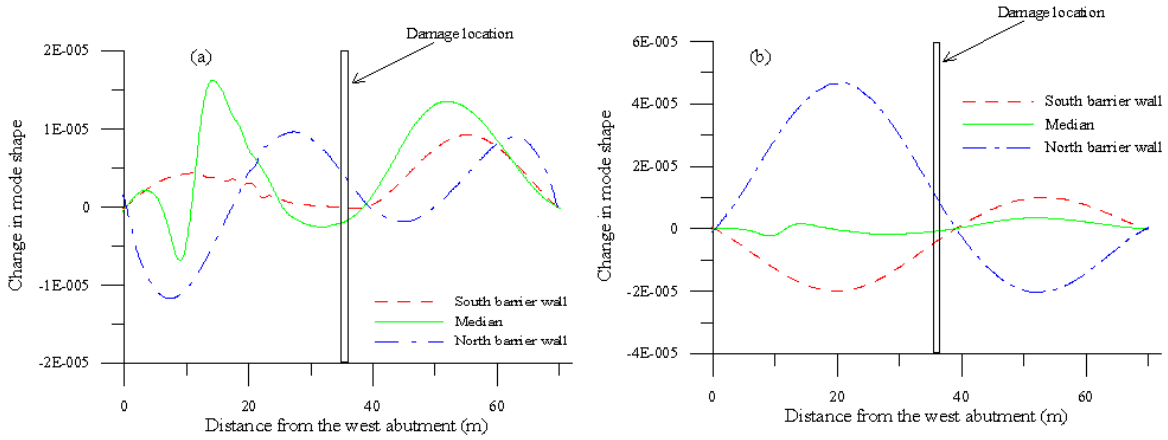

Figure 6.12. Distributions of changes in mode shape caused by damage state 8 at an ambient temperature of 20°C along selected longitudinal lines: (a) calculated using line-by-line normalization; and (b) surface normalization.

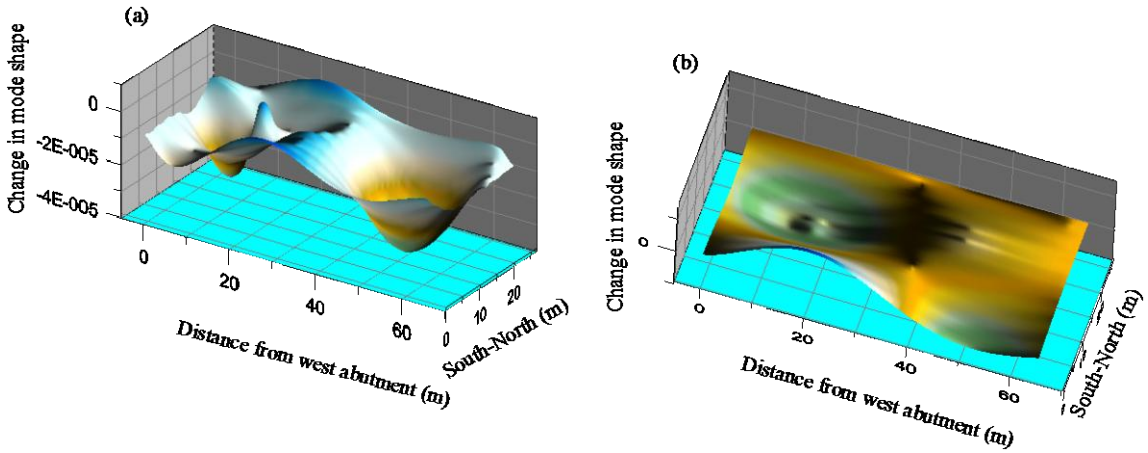

Figure 6.13. Spatial distributions of changes in mode shape caused by damage state 6 at an ambient temperature of 20°C: (a) calculated using line-by-line normalization; and (b) surface normalization.

Figure 6.14a and Figure 6.14b show the distributions of the change in mode shape along three longitudinal lines (north barrier wall, south barrier wall, and median) for damage state 6, which is located immediately adjacent to the median line. As seen in Figure 6.14a, when line-by-line normalization is used, the mode shape change curve plotted along the median exhibits a distinct peak at the centre of the damage location, along with adjacent negative depressions that are characteristic of damage scenarios situated away

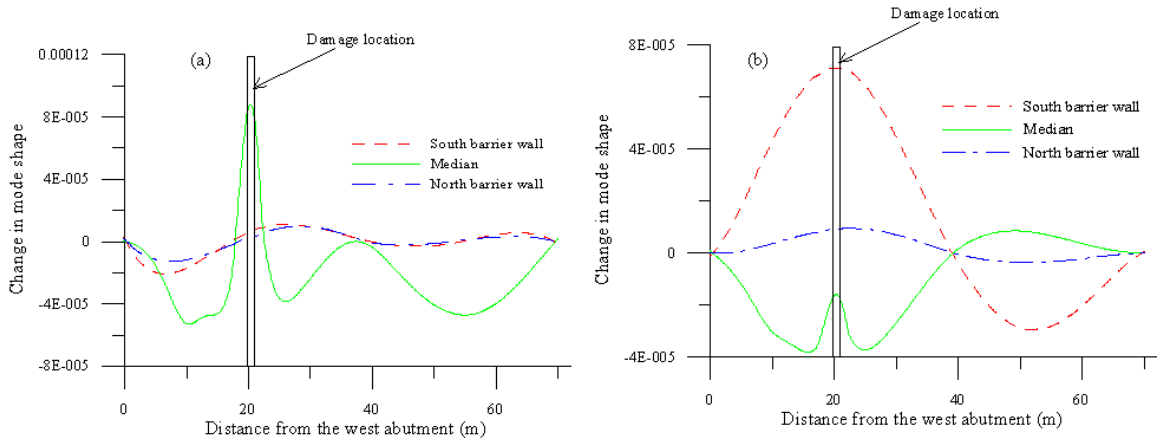

Figure 6.14. Distributions of changes in mode shape caused by damage state 6 at an ambient temperature of 20°C along selected longitudinal lines: (a) calculated using line-by-line normalization; and (b) surface normalization.

from abutments and piers. The distributions of mode shape change along the north and south barrier walls exhibit smoothly varying patterns with lower magnitudes that do not provide any apparent indication of the damage location. It is clearly evident in Figure 6.14a that when line-by-line normalization is used, the mode shape changes can successfully detect and locate the damage providing that the damage site is in close proximity to sensor locations. As seen in Figure 6.14b, a small peak at the damage location is also observed in the median distribution line obtained using surface normalization.

Similarly, for damage state 1, the spatial distribution using line-by-line normalization (Figure 6.15a) shows a distinctive negative peak at the location of damage. This characteristic negative peak was observed for all damage cases located near the pier and abutments. The surface normalization plot (Figure 6.15b) exhibits a smooth pattern without any sharp change in mode shape in the vicinity of the damage.

The longitudinal line plots for damage state 1 at 20°C are presented in Figure 6.16. In Figure 6.16a, the mode shape change curve plotted along the south barrier wall exhibits a negative peak at the location of damage state 1. The lateral location of the damage (adjacent to the south barrier wall), though, is not immediately obvious (Figure 6.16a) since there is a higher magnitude peak in the median line plot than along the south barrier wall. Therefore, when the location of damage is not known in advance,

Figure 6.16a provides an indication of the longitudinal damage location, but does not clearly show its lateral position. Figure 6.16b, on the other hand, does not provide any clear indication of the location of damage, although the existence of damage might be inferred from the smoothly varying changes observed in general.

A similar set of analyses was performed when both the baseline and the damaged mode shapes were obtained at a simulated temperature of -25°C. Figures 6.17, 6.18 and 6.19 show the resulting change in mode shape distributions for damage states 8, 6 and 1, respectively, along the three measurement lines. It is apparent that the same patterns of

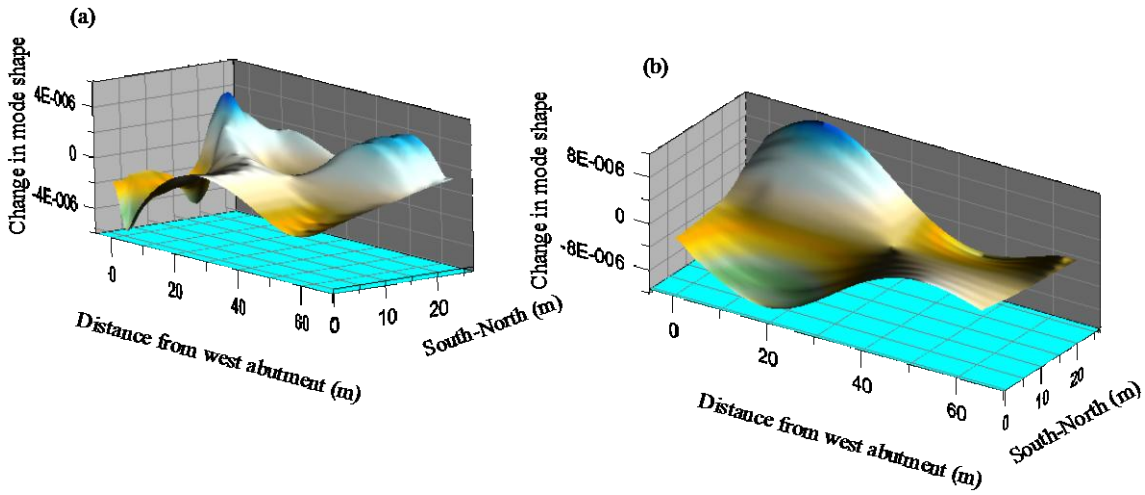

Figure 6.15. Spatial distributions of changes in mode shape caused by damage state 1 at an ambient temperature of 20°C: (a) calculated using line-by-line normalization; and (b) surface normalization.

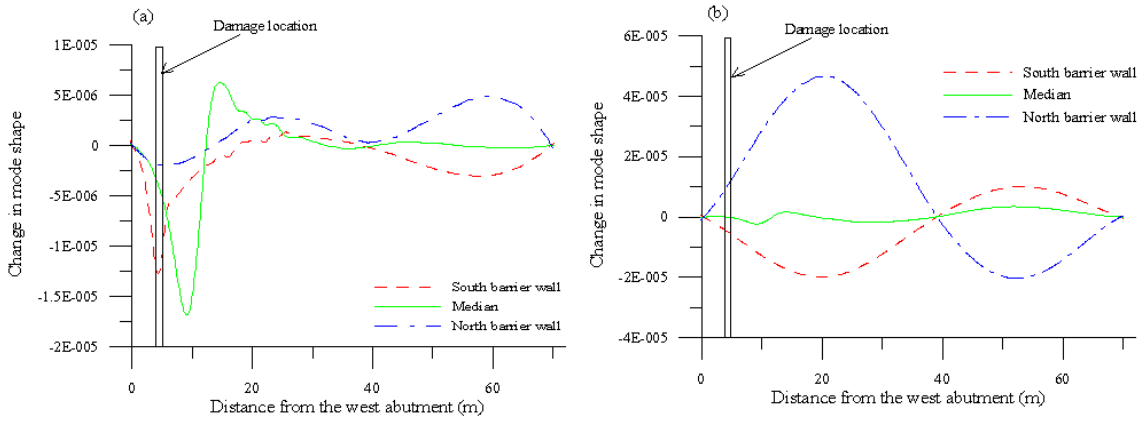

Figure 6.16. Distributions of changes in mode shape caused by damage state 1 at an ambient temperature of 20°C along selected longitudinal lines: (a) calculated using line-by-line normalization; and (b) surface normalization.

mode shape changes were obtained at this temperature using line-by-line normalization as were obtained at 20°C. However, in contrast to the results at 20°C, as seen in Figure 6.19b, the south barrier wall mode shape change plot displays a distinct peak at the centre of the missing elements for damage case 1, which is located adjacent to the south barrier wall; this peak was absent in the 20°C results (Fig. 6.16b). For damage case 6, the median mode shape change plot (Figure 6.18b) exhibits a high magnitude positive peak centered at the damage location, while further away from the damage, the mode

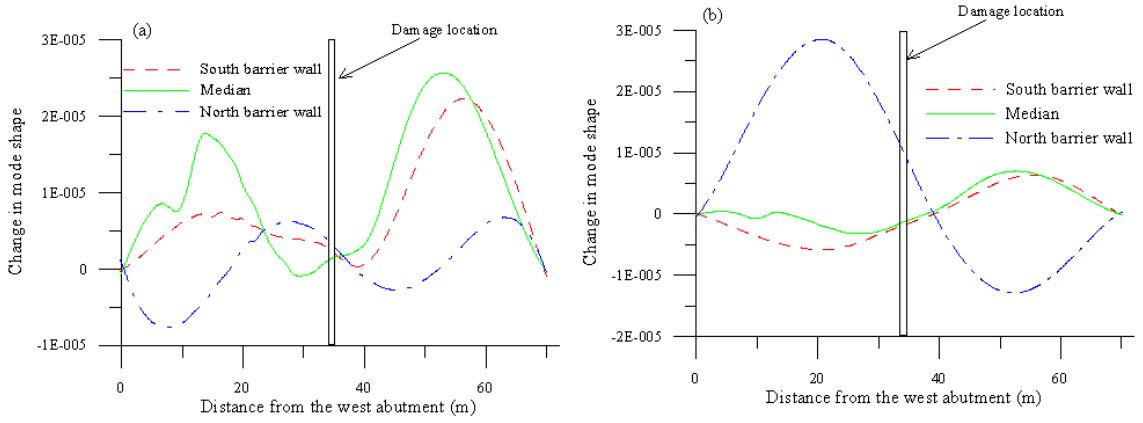

Figure 6.17. Distributions of changes in mode shape caused by damage state 8 at a temperature of -25°C for both baseline and damaged measurements along selected longitudinal lines: (a) calculated using line-by-line normalization; and (b) surface normalization.

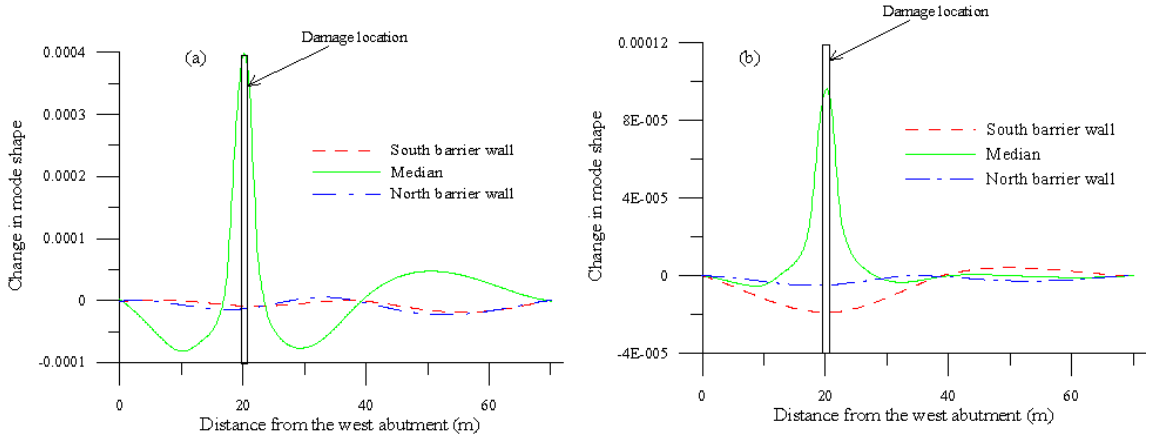

Figure 6.18. Distributions of changes in mode shape caused by damage state 6 at an ambient temperature of -25°C for both baseline and damaged measurements along selected longitudinal lines: (a) calculated using line-by-line normalization; and (b) surface normalization.

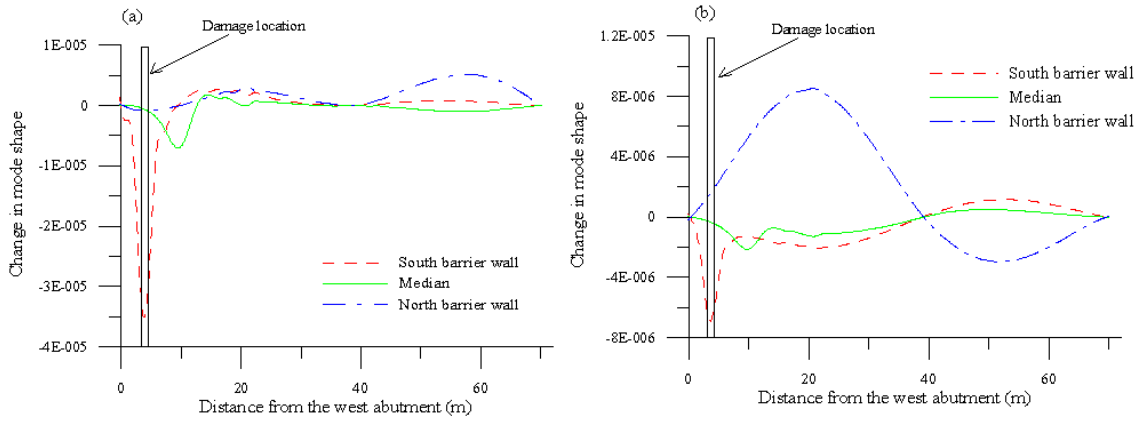

Figure 6.19. Distributions of changes in mode shape caused by damage state 1 at an ambient temperature of -25°C for both baseline and damaged measurements along selected longitudinal lines: (a) calculated using line-by-line normalization; and (b) surface normalization.

shape change exhibits a smoothly varying pattern with a much lower magnitude. Thus, surface normalization appears to be effective for localizing damage located adjacent to the sensor locations.

In summary, it was found that localised damage to the wearing surface and concrete deck slab of the bridge could be reliably detected and located if the sensors were located sufficiently close to the damage location. Line-by-line normalization provided a more reliable indication of damage location than surface normalization. It appears that these results apply at different ambient temperatures, as long as both baseline and subsequent measurements are made at the same temperature.

6.5 COMBINED INFLUENCE OF DAMAGE AND TEMPERATURE ON CHANGES IN MODAL PARAMETERS

In the previous sections, the effects of temperature and damage on the dynamic properties of the bridge were examined separately. In this section, the combined effect of both temperature variation and damage on the modal parameters of the overpass is considered when the measurements are made at a different temperature than those at which baseline measurements were made.

For this study, modal properties for the damaged structure were generated at an ambient temperature of -25°C while the undamaged baseline properties were obtained at an

ambient temperature of 20°C. The spatial distributions of mode shape changes corresponding to damage states 8, 6 and 1 are shown in Figure 6.20, 6.21 and 6.22, respectively. The corresponding distributions along the three longitudinal lines (possible sensor locations) are shown in Figure 6.23, 6.24 and 6.25.

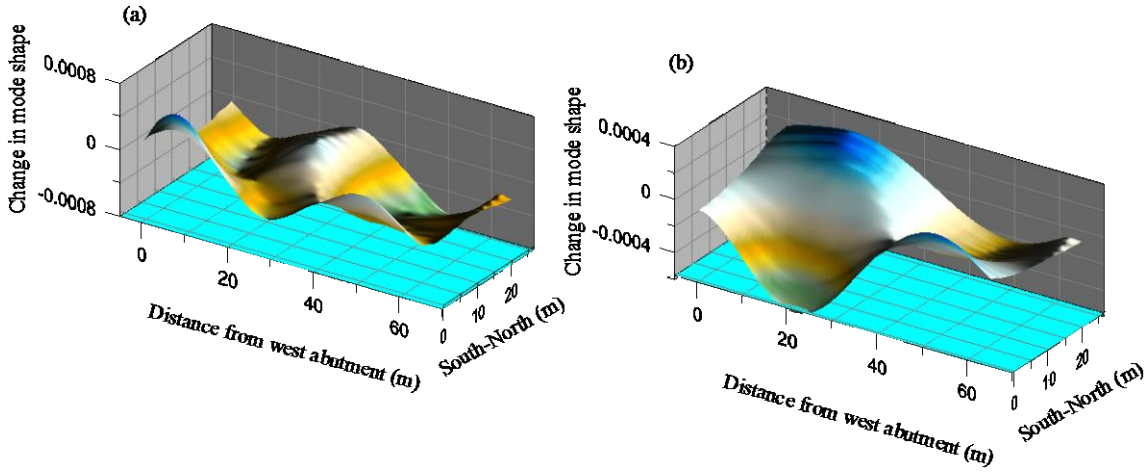

Figure 6.20. Spatial distributions of changes in mode shape caused by damage state 8 at an ambient temperature of -25°C compared to the baseline undamaged case at 20°C: (a) calculated using line-by-line normalization; and (b) surface normalization.

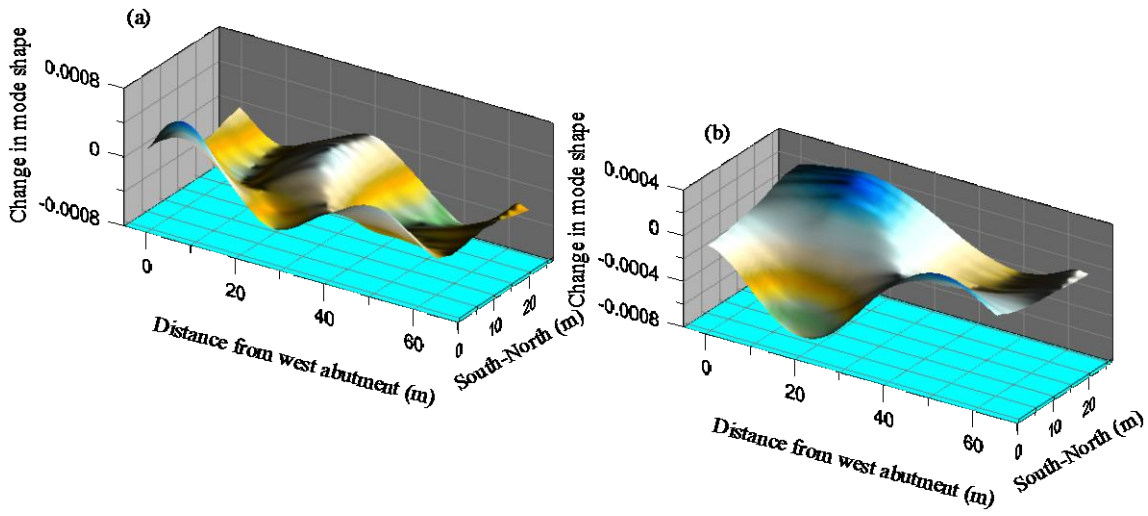

Figure 6.21. Spatial distributions of changes in mode shape caused by damage state 6 at an ambient temperature of -25°C compared to the baseline undamaged case at 20°C: (a) calculated using line-by-line normalization; and (b) surface normalization.

As seen by comparing Figures 6.20, 6.21, 6.22 with Figure 6.5, as well as comparing Figures 6.23, 6.24 and 6.25 with Figure 6.7, both the spatial distributions and those along the three lines are similar to those obtained as a result of temperature changes

alone. The only exception was for damage state 6, for which a small upward peak is apparent along the median line (Figure 6.24a and Figure 6.24b) at the location of damage.

Therefore, it can be concluded that the changes in mode shapes caused by damage are relatively small and are almost completely masked by the temperature-induced mode shape changes.

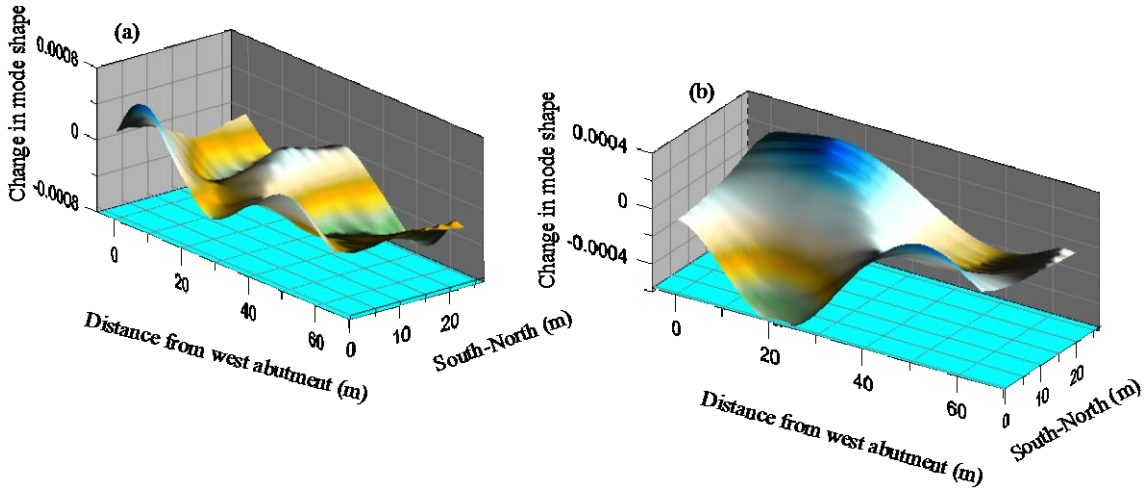

Figure 6.22. Spatial distributions of changes in mode shape caused by damage state 1 at an ambient temperature of -25°C compared to the baseline undamaged case at 20°C: (a) calculated using line-by-line normalization; and (b) surface normalization.

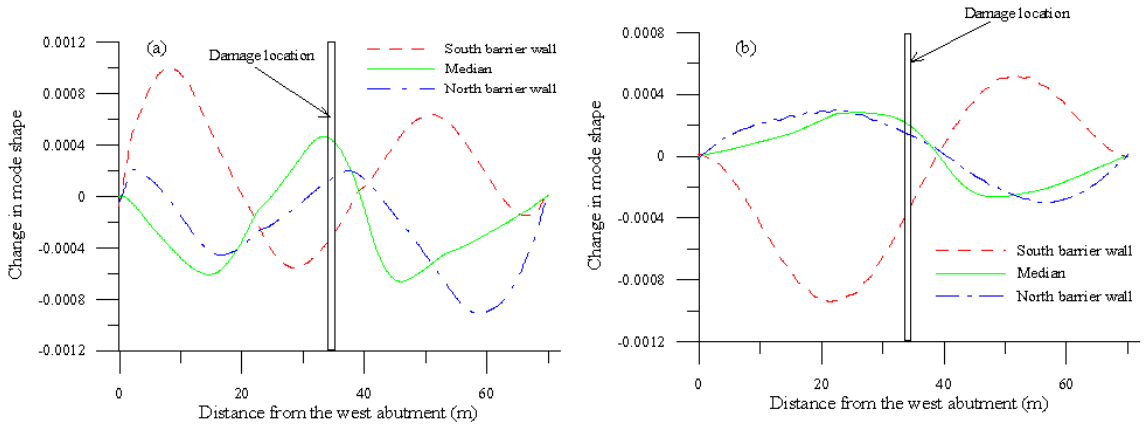

Figure 6.23. Distributions of changes in mode shape caused by damage state 8 at an ambient temperature of -25°C compared to the baseline undamaged case at 20°C along three longitudinal lines: (a) calculated using line-by-line normalization; and (b) surface normalization.

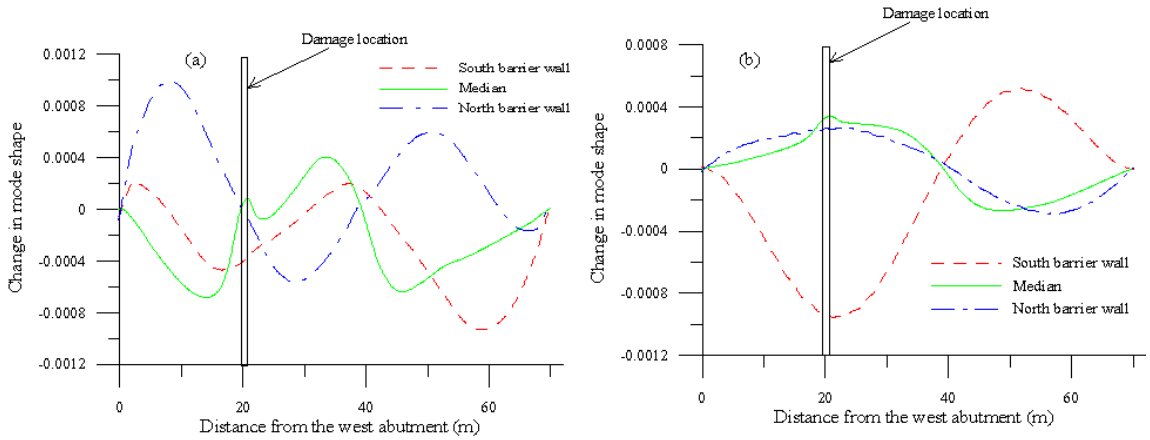

Figure 6.24. Distributions of changes in mode shape caused by damage state 6 at an ambient temperature of -25°C compared to the baseline undamaged case at 20°C along three longitudinal lines: (a) calculated using line-by-line normalization; and (b) surface normalization.

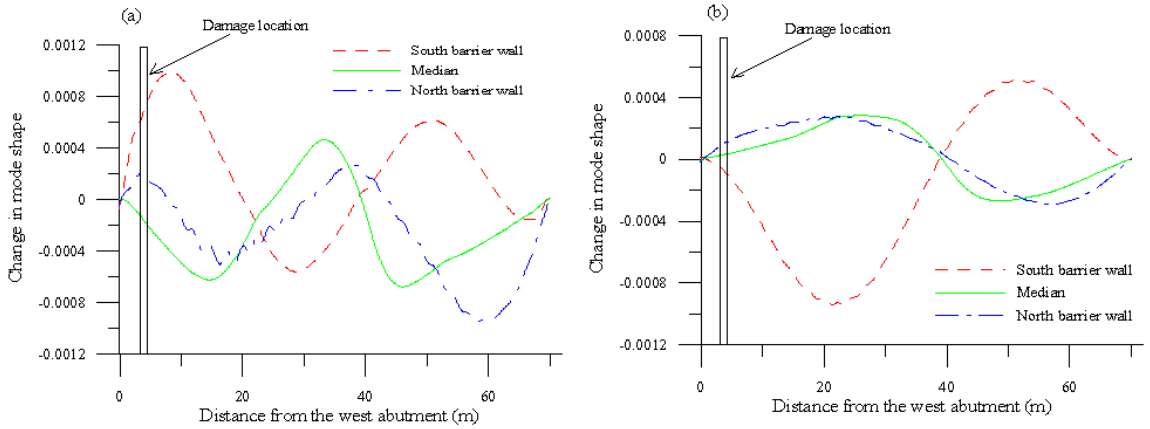

Figure 6.25. Distributions of changes in mode shape caused by damage state 1 at an ambient temperature of -25°C compared to the baseline undamaged case at 20°C along three longitudinal lines: (a) calculated using line-by-line normalization; and (b) surface normalization.

6.6 DIFFERENTIATION OF DAMAGE- AND TEMPERATURE-INDUCED MODE SHAPE CHANGES

As seen by comparing Figure 6.4a, Figure 6.5a, Figure 6.11a, Figure 6.13a, and Figure 6.15a, the magnitudes of mode shape changes caused by temperature changes were considerably higher than those caused by damage. It was also found that the damage-induced mode shape changes exhibited a prominent peak at the damage location when line-by-line normalization was used, while the temperature-induced mode shapes varied smoothly over the bridge deck surface.

In addition, when sensors were restricted to three longitudinal lines (north barrier wall, south barrier wall, and median), the mode shape changes exhibited distinct and unambiguous peaks near the damage when damage was in close proximity to one of the sensor lines (Figure 6.14a, Figure 6.16a, Figure 6.18a, and Figure 6.19a). On the other hand, when the damage site was located far from any of the sensor lines, the patterns of damage-induced mode shape changes were similar to those corresponding to temperature-induced mode shape changes (Figure 6.12a and Figure 6.17a). It is therefore concluded that the change in mode shape can only be used to locate damage sites which lie in close proximity to sensors and that changes caused by temperature variations will make even this very difficult.

In order to distinguish mode shapes changes caused by temperature changes from those caused by damage states which are located at a distance from the sensor lines, four VBDD methods were used. These methods included the change in mode shape curvature, change in flexibility, change in uniform flexibility curvature, and damage index methods, which were described in Section 4.6.

The results of the implementation of the four VBDD methods for damage state 8 at a temperature of 20°C along three sensor lines are shown in Figure 6.26. It is evident that none of the methods provide a clear indication of the location of damage. The mode shape curvature, damage index and change in uniform flexibility curvature plots (Figure 26a, 26b, and 26d, respectively) exhibit near-zero amplitudes on the east span of the bridge and around the damage location. The change in flexibility method shows humps with different magnitude across the two spans of the bridge.

Figure 6.27 shows the VBDD plots resulting from a drop in temperature from 20°C to -25°C without damage. Figure 27a, 27b, and 27d exhibit peaks located at the west and east abutments and vary with an irregular pattern of small amplitude bumps along the bridge. Again, the change in flexibility method shows single smooth humps across each span of the bridge.

The same pattern was observed in Figures 6.28 and 6.29, which resulted when the four methods were applied, respectively, to an increase in ambient temperature from 20°C to 35°C, and to the case of inducing damage state 8 at -25°C using a baseline at 20°C.

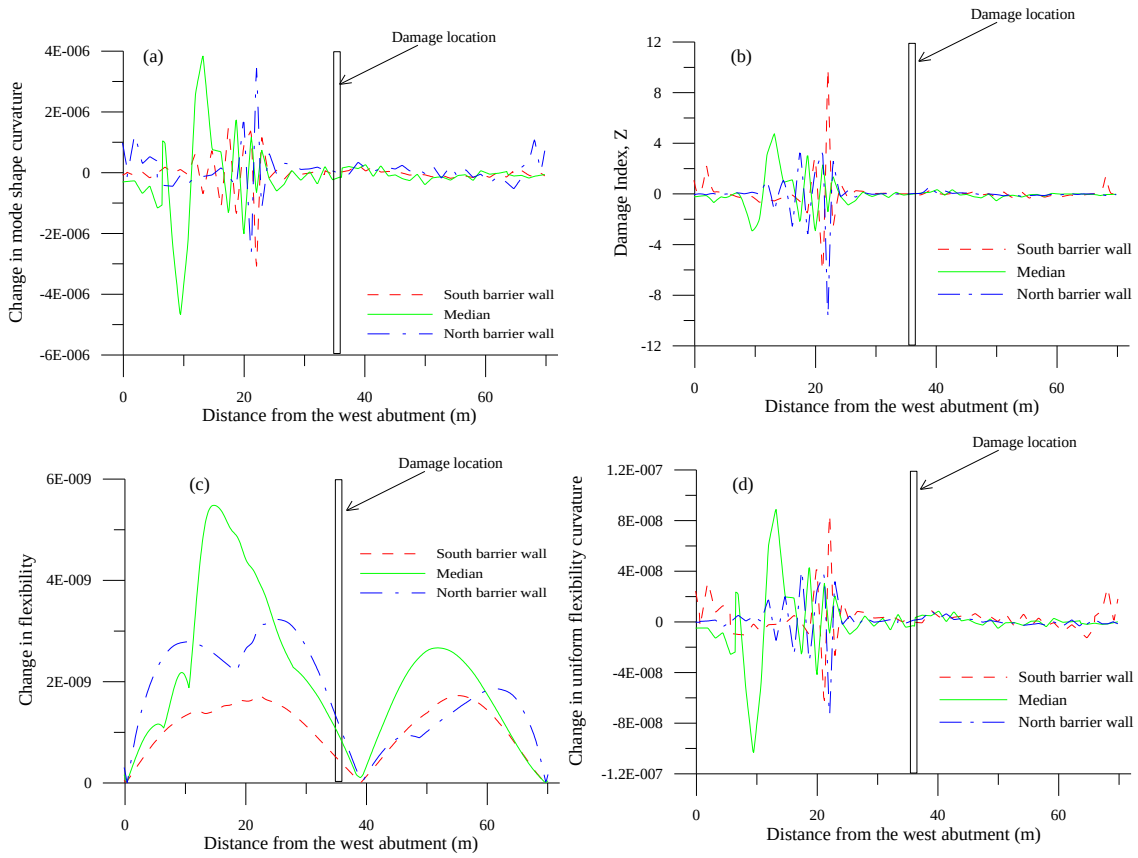

Figure 6.26. Distributions of VBDD parameters using line-by-line normalization for damage case 8 at a temperature of 20°C along selected longitudinal lines: (a) change in mode shape curvature; (b) normalised damage index; (c) change in flexibility; and (d) uniform flexibility curvature.

It can be seen from the Figure 6.26, 6.27, 6.28, and 6.29 that the distributions of the four VBDD parameters caused by a change in temperature without damage may be somewhat different in pattern to those produced by damage located at some distance from the sensor locations. However, these differences cannot be clearly identified by simple observation. One possible exception is the pattern associated with the change in flexibility parameter; while temperature induced changes result in single smooth humps across each span (Figure 6.27c and 6.28c), damage appears to superimpose additional smaller bumps of shorter wavelength on the broader humps (Figs. 6.26c and 6.29c).

In an attempt to better understand the differences between temperature-induced mode shape changes and mode shape changes caused by damage at some distance from the sensor, a more quantitative analysis was implemented. The mode shape change

distributions along each of the three sensor lines were analyzed to determine their spatial frequency components using a FFT. The distance along the bridge was substituted for the time variable normally used in a Fourier analysis, while the change in mode shape was substituted for the signal amplitude. The mode shape changes along three sensor lines were sampled at a rate of 500 samples per meter for the bridge length.

The resulting FFT spectra for both damage-induced changes (damage state 8 at a temperature of 20°C) and temperature-induced changes (a reduction in temperature from 20°C to -25°C and an increase in temperature from 20°C to 35°C) corresponding to each longitudinal line (north barrier wall, median, and south barrier wall) are shown in Figure 6.30.

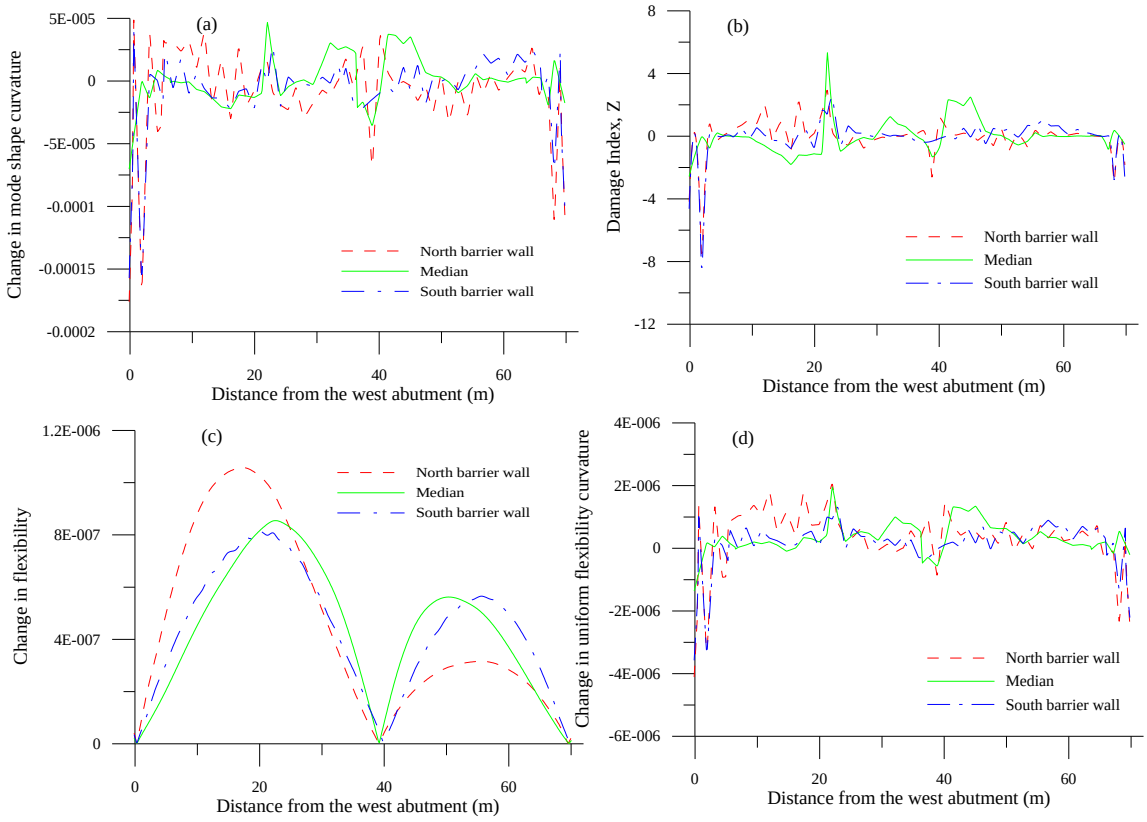

Figure 6.27. Distributions of VBDD parameters using line-by-line normalization corresponding to temperature decrease from 20°C to -25°C without damage along selected longitudinal lines: (a) change in mode shape curvature; (b) normalised damage index; (c) change in flexibility; and (d) uniform flexibility curvature.

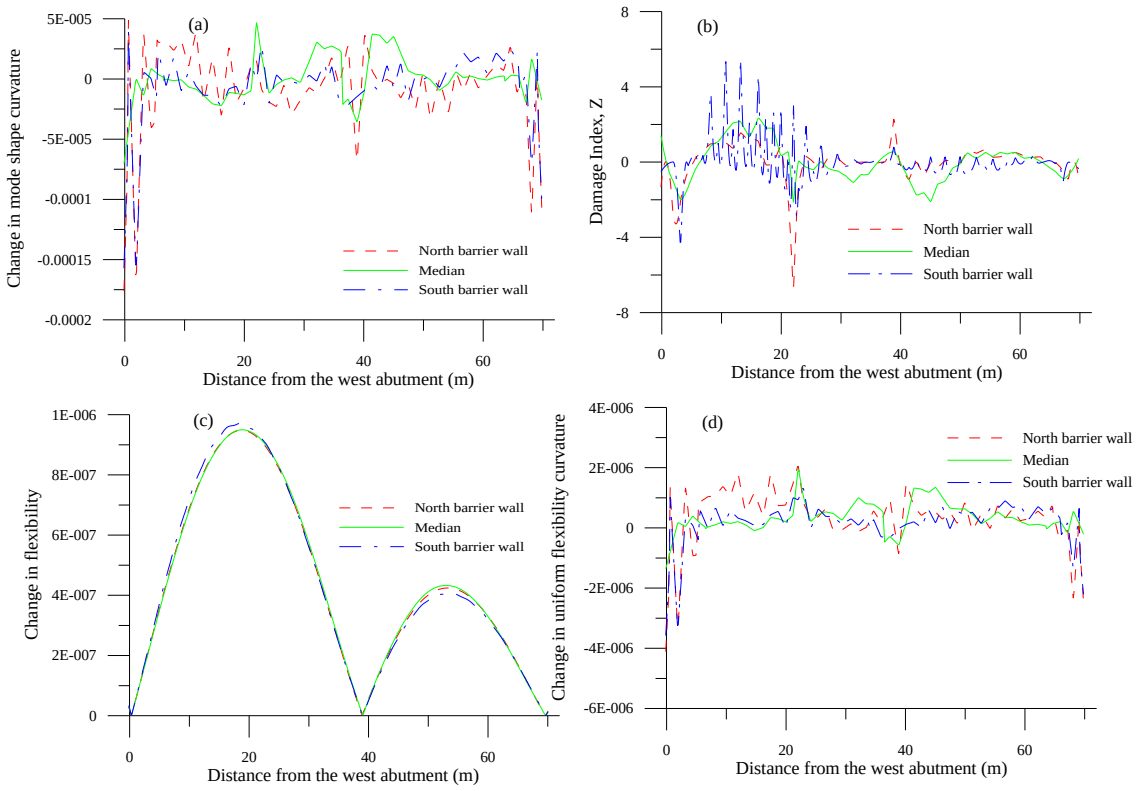

Figure 6.28. Distributions of VBDD parameters using line-by-line normalization corresponding to a temperature increase from 20°C to 35°C without damage along selected longitudinal lines: (a) change in mode shape curvature; (b) normalised damage index; (c) change in flexibility; and (d) uniform flexibility curvature.

Figure 6.30 presents the wavelength components contributing to calculated mode shape changes. As seen in Figure 6.30a, 6.30b and 6.30c, all FFT spectra are dominated by larger wavelengths on the order of the span length. By visual comparison, there is no obvious difference in the wavelength content of mode shape changes associated with damage and temperature changes.

By observing the previously presented distributions, including those describing the four VBDD parameters as well as the FFT analysis results for the mode shape change curves, it becomes apparent that patterns of temperature-induced mode shape changes were quite similar to those produced by damage located at some distance from sensor locations. It is, therefore, not a simple exercise to distinguish between the two sources of mode shape changes by simple observation. If there are differences, more sophisticated pattern recognition algorithms will likely be required to identify them.

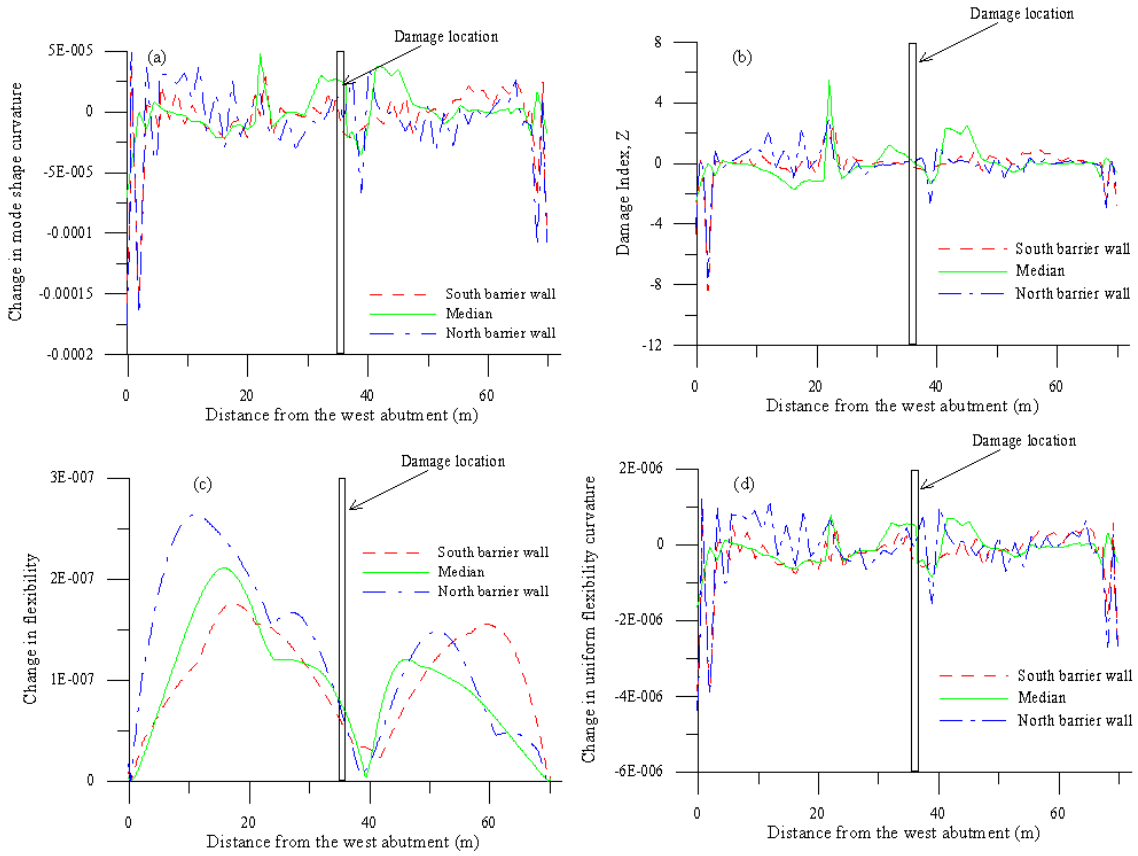

Figure 6.29. Distributions of VBDD parameters using line-by-line normalization along three longitudinal lines caused by damage state 8 at an ambient temperature -25°C compared to the baseline undamaged case at 20°C: (a) change in mode shape curvature; (b) normalised damage index; (c) change in flexibility; and (d) uniform flexibility curvature.

In summary, it was found that ambient temperature variations produced significant changes in both the natural frequencies and mode shapes of the structure. Although the patterns of mode shape changes due to temperature effects differed to some degree from those caused by low levels of damage to the bridge deck, the considerably larger temperature-induced changes were shown to be capable of effectively masking the effects of such damage.

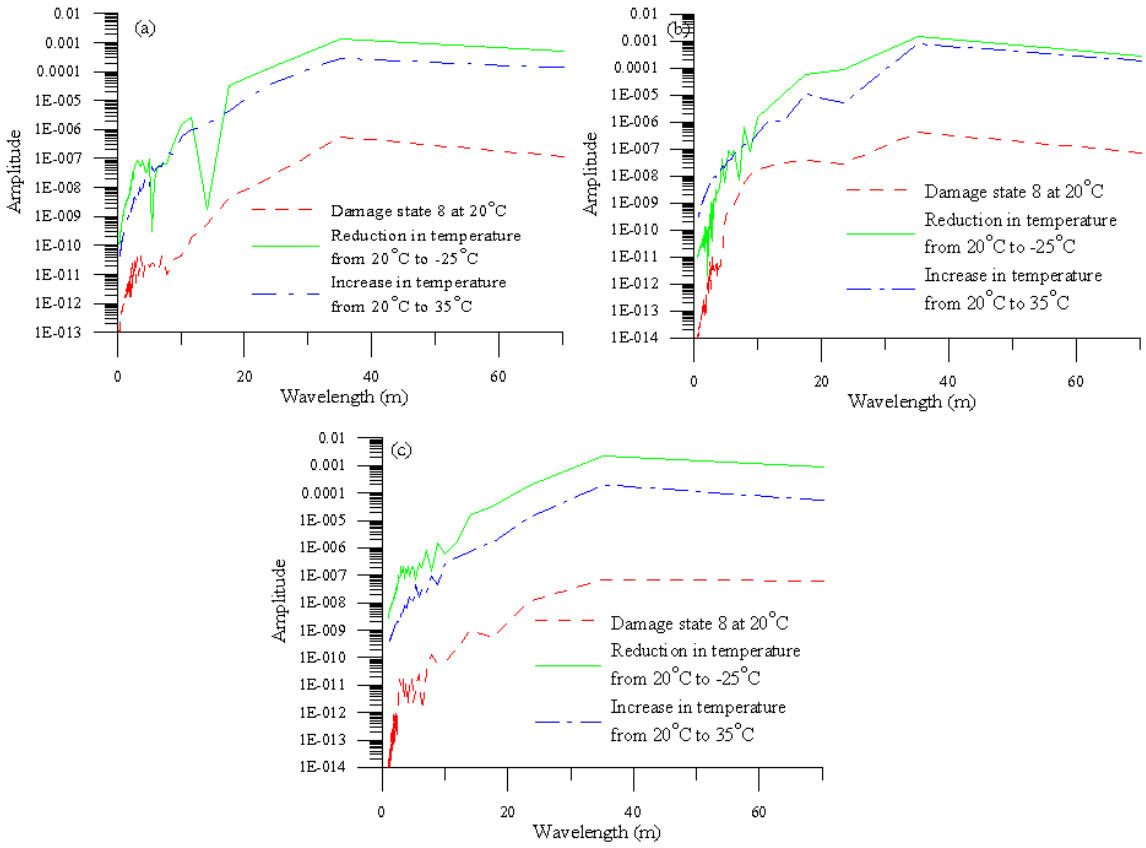

Figure 6.30. Comparison of FFT spectra between damage-induced mode shape changes and temperature-induced mode shape changes using line-by-line normalization: (a) along the north barrier wall; (b) along median; and (c) along the south barrier wall.

CHAPTER 7 . CONCLUSIONS AND RECOMMENDATIONS

7.1 SUMMARY

The influence of thermal effects on the structural health monitoring of the Attridge Drive overpass was experimentally and numerically studied. Field experiments were conducted over a wide range of temperatures. The recorded dynamic response of the bridge revealed a relationship between natural frequencies and ambient temperature. Three-dimensional finite element models of the overpass, based on an earlier version, were revised and calibrated to field measurements to accurately predict the structure's behaviour with varying temperature. Finite element and field measurement results were used to study how temperature change affected the structure's dynamic characteristics. Finite element analysis was also used to compare the changes in dynamic properties resulting from imposing damage on the bridge deck with those resulting from changing temperature.

This chapter presents the main conclusions. It should be recognized that the conclusions are restricted to the conditions considered in this study. More research is needed to confirm and extend the conclusions to more general situations. Some recommendations for future studies are also presented.

7.2 CONCLUSIONS

It was found that ambient temperature variations produced substantial changes in measured natural frequencies. The lowest three measured natural frequencies of the bridge decreased by 8.3 %, 12.3 %, and 12 %, respectively, as the ambient temperature

increased from -12°C to 40°C. These changes were mainly caused by the reduction of the modulus of elasticity of the asphalt and concrete with increasing temperature. It was found that the natural frequencies can be approximately described as being bilinearly dependent on measured temperature. The changes in natural frequencies caused by damage to the surface of the deck covering an area of approximately 6.25 m^2 was much lower (in the order of 10^{-4} Hz) compared to the changes in natural frequencies due to temperature changes.

The first three measured mode shapes were found to be relatively insensitive to temperature change. Compared to normalized modal amplitudes obtained at 20°C to 26°C, differences in normalized modal amplitudes measured in all other temperatures ranges were found not to be statistically significant at a 95 percent confident level. Rather, the differences between mode shapes obtained in any given temperature range were mainly due to the variability in the mode shape measurements.

Finite element simulations of large scale temperature variations (a drop from 20°C to -25°C and an increase from 20°C to 35°C) were found to induce notable changes in the fundamental mode shape, manifested by fairly smooth undulations in the mode shape change distributions, with wavelengths approximately corresponding to the bridge spans. On the other hand, mode shape changes caused by damage, when baseline and damaged measurements were taken at the same temperature, showed a local peak at the location of damage. However, these local peaks were generally only apparent if a line-by-line normalization approach was used and a sensor line was located close to the damage.

As was mentioned, when there was no change in temperature, damage could be detected and located as long as the damage location lay in close proximity to sensors. When baseline and damaged measurements were taken at different temperatures, the mode shape changes caused by small-scale damage were masked by those caused by temperature variations.

When the effects of temperature and damage on mode shapes were studied separately, it was found that the patterns of mode shape changes caused by damage in the immediate vicinity of the sensors were easily distinguished from those due to ambient temperature

change. A distinct local peak in mode shape changes caused by damage was generally apparent, while smoothly varying curves appeared in those due to temperature change.

In the case when damage was located some distance from the sensors, both the distributions of the four vibration-based damage detection (VBDD) parameters investigated and the patterns of mode shape changes caused by damage differed to some degree from those caused by temperature changes. However, these changes could generally not be clearly identified by simple observation. An attempt was also made to identify the spatial frequency content in the mode shape changes by performing a Fast Fourier Transform (FFT) on the changes. No considerable differences were seen between the FFT spectra of the mode shape changes caused by damage and those caused by temperature changes.

The normalization methods used to scale mode shapes had a substantial influence on the distributions of VBDD parameters. Line-by-line normalization increased the differences between damaged and undamaged mode shapes, thereby emphasizing local changes in mode shape and increasing the precision of damage localization, as compared to surface normalization.

7.3 RECOMMENDATIONS FOR FUTURE STUDIES

It is recommended that the baseline dynamic properties of the bridge be taken at several additional ambient temperatures. Ongoing field measurements should be conducted at temperatures close to the temperatures at which baseline properties were measured to reduce the effect of temperature change on the application of vibration-based damage detection.

It is suggested that more research on the application of pattern recognition be done in order to differentiate between the patterns of mode shape parameters caused by small-scale damage and those caused by temperature effects.

It is also recommended that continuous monitoring with embedded sensors be used instead of intermittent monitoring. The purpose of using continuous monitoring is to record more data, thereby providing more consistency in results.

If possible, more sensors should be used to record other environmental parameters such as the concrete temperature at the top, middle and bottom of the deck, soil temperature behind the abutment walls, humidity, and wind characteristics to account for the effects of these factors on vibration-based damage detection.

More accelerometers should be used to reduce the distance between damage location and sensor position, thereby enhancing the application of vibration damage detection to the bridge.

It is recommended that a proper test protocol be developed to ensure the reliability of the field instrumentation, and minimize the error in measurement, thus providing higher quality field data.

REFERENCES

ADINA. 2002. ADINA Version 8.0.2. ADINA R&D, Inc., Watertown, Massachusetts.

Alampalli, S., Dillon, E.W., and Fu, G. 1997. Signal versus noise in damage detection by experimental modal analysis. Journal of Structural Engineering, **123**(2): 237-245.

Alampalli, S. 1998. Influence of in-service environment on modal parameters. Proceedings of the 16th International Modal Analysis Conference, Society of Experimental Mechanics, Santa Barbara, California, pp. 111-116.

Alwash, M., Sparling, B.F., and Wegner, L.D. 2005. Excitation sources for vibration-based damage detection on the Red Deer River Bridge. Proceedings of 1st Canadian Society of Civil Engineering (CSCE) Specialty Conference on Infrastructure Technologies, Management and Policy. Toronto, Ontario, paper FR-124.

Alwash, M., Sparling, B.F. and Wegner, L.D. 2006. Influence of the excitation source on modal parameter estimation for the Red Deer River Bridge. Proceedings of the 1st Canadian Society of Civil Engineering (CSCE) International Structural Specialty Conference, Calgary, Alberta, Paper No. ST-028.

Alwash, M., Sparling, B.F., and Wegner, L.D. Submitted 2009. Influence of Excitation Dynamic System Identification for a Multi-span Reinforced Concrete Bridge. Submitted to Journal of Advances in Civil Engineering.

Bangash, M.Y.H. 1989. Concrete and concrete structures: numerical modelling and applications. Elsevier Science Publishers LTD, Crow House, Linton Road, Banking, Esseex, England.

Brownjohn, J. M., Lu, Y., Moyo, P., and Omenzetter, P. 2003. Assessment of Highway Bridge upgrading by dynamic testing and finite-element model updating. Journal of Bridge Engineering, American Society of Civil Engineers, **8**(3): 162-172.

Casas, J.R., and Aparicio, A.C. 1994. Structural damage identification from dynamic-test data. Journal of Structural Engineering, American Society of Civil Engineers, **120**(8): 2437-2450.

Cawley, P., and Adams, R.D. 1979. The location of defects in structures from measurements of natural frequencies. Journal of Strain Analysis, **14**(2): 49-57.

Chen, J., Young, B., and Uy, B. 2006. Behavior of High Strength Structural Steel at Elevated Temperatures. ASCE Journal of Structural Engineering, **132**(12): 1948-1954.

Cornwell, P.J., Doebling, S.W., Farrar, C.R., and Sohn, H. 1999. Environmental variability of modal properties. Journal of Experimental Techniques, **23**: 45-48.

CSA. 2004. Design of concrete structures. CSA standard CSA-A23.3-04, Canadian Standards Association, Mississauga, Ontario.

Doebling, S.W., Farrar, C.R., Prime, M.B., and Shevitz, D.W. 1996. Damage identification and health monitoring of structural and mechanical systems from

changes in their vibration characteristics: A literature review. Report No. LA 13070-MS, Los Alamos National Laboratory, Los Alamos, New Mexico.

Doebling, S.W., Farrar, C.R., and Goodman, R. 1997. Effects of measurement statistics on the detection of damage in the Alamosa Canyon Bridge. Proceedings of the 15th International Modal Analysis Conference, Orlando, Florida, pp. 919-929.

Doebling, S.W., Farrar, C.R., and Cornwell, P.J. 1997. A statistical comparison of impact and ambient test results from the Alamosa Canyon Bridge. Proceeding of the 15th International Modal Analysis Conference, Orlando, Florida, pp. 264-270.

Ewins, D.J. 2000. Modal testing: theory, practice and application, 2nd edition. Research Studies Press Ltd., Hertfordshire, England.

Farrar C.R., Doebling S.W., Cornwell P.J., and Straser E.G. 1997. Variability of modal parameters measured on the Alamosa Canyon Bridge. Proceeding of the 15th International Modal Analysis Conference, Orlando, Florida, pp. 257-263.

Farrar, C.R. and Duffey, T.A. 1999. Vibration-based damage detection in rotating machinery. Journal of Key Engineering Materials, **167-168**: 224-235.

Farrar, Charles R., Sohn, Hoon, Fugate, Michael L., and Czarnecki, Jerry J. 2001. Integrated Structural Health Monitoring. Proceedings of the International Society for Optical Engineering (SPIE): 8th Annual International Symposium on Smart Structures and Materials, Newport Beach, California.

Fox, C.H.J. 1992. The location of defects in structures: a comparison of the use of natural frequency and mode shape data. Proceedings of the 10th International Modal Analysis Conference, San Diego, California, pp. 522-528.

Fugate, M.L., Sohn, H., and Farrar, C.R. 2000. Unsupervised learning methods for vibration-based damage detection. Proceedings of the 18th International Modal Analysis Conference, San Antonio, Texas.

Glantz, S..A. 2005. Primer of Biostatistics. The McGraw-Hill Company, New York, New York.

Hajela, P., and Soeiro, F.J. 1990. Recent developments in damage detection based on system identification methods. Journal of Structural and Multidisciplinary Optimization, **2**(1): 1-10.

Halling, M.W., Muhammad, I., and Womack, K. C. 2001. Dynamic field testing for condition assessment of bridge bents. Journal of Structural Engineering, **127**(2): 161–167.

Hermans, L., and Van Der Auweraer, H. 1999. Modal testing and analysis of structures under operational conditions: Industrial applications. Journal of Mechanical Systems and Signal processing, **13**(2): 193-216.

Housner, G.W., Bergman, L.A., Caughey, T.K., Chassiakos, A.G., Claus,R.O., Masri, S.F., Skelton, R.E., Soong, T.T., Spencer, B.F., and Yao, J.T.P. 1997. Structural control: past, present, and future. Journal of Engineering Mechanics, American Society of Civil Engineers, **123**(9): 897 - 971.

Hu, N., Wang, X., Fukunaga, H., Yao, Z.H., Zhang, H.X., and Wu, Z.S. 2001. Damage assessment of structures using modal test data. International Journal of Solids and Structures, **38**(18): 3111-3126.

Kato, M., and Shimada, S. 1984.Vibration of PC bridge during failure process. Journal of Structural Engineering, **112**(7):1692–1703.

Kim, J.T., and Stubbs, N. 1995. Model uncertainty impact and damage-detection accuracy in plate girder. Journal of Structural Engineering, American Society of Civil Engineers, **121**(10): 1409-1417.

Kim, J.T., and Stubbs, N. 2003. Non-destructive crack detection algorithm for full-scale bridges. Journal of Structural Engineering, American Society of Civil Engineers, **129**(10): 1358-1366.

Kim, B.H., Stubbs, N., and Park, T. 2005. A new method to extract modal parameters using output-only responses. Journal of Sound and Vibration, **282**: 215–230.

Kinemetrics. 2002. EpiSensor force balance accelerometer model FBA ES-U manual. Kinemetrics, Inc., Pasadena, California.

LabView. 2000. LabViewTM - version 6i, National Instruments Corporation, Austin, Texas.

Lloyd, G.L., Singh, V., and Wang, M.L. 2000. Observed variations of mode frequencies of a pre-stressed concrete bridge with temperature. Proceedings of Condition Monitoring of Materials and Structures, Engineering Mechanics Conference, Austin, Texas, pp. 179-189.

Li, G.Q., Jiang, S.C., Yin, Y.Z., Chen, K. and Li, M.F. 2003. Experimental studies on the properties of constructional steel at elevated temperatures. ASCE Journal of Structural Engineering, **129**(12): 1717-1721.

Loland, O. and Dodds, J.C. 1976. Experience in developing and operating integrity monitoring system in North Sea. Proceedings of the 8th Annual Offshore Technology Conference, pp. 313-319.

Londoño, N.A., and Lau, D.T. 2006. Confederation Bridge vibration monitoring: implications for structural health monitoring. Proceedings of the 1st Canadian Society of Civil Engineering (CSCE) International Structural Specialty Conference, Calgary, Alberta.

Maeck, J., and De Roeck, G. 1999. Damage detection on a prestressed concrete bridge and RC beams using dynamic system identification, damage assessment of structures. Proceedings of the International Conference on Damage Assessment of Structures (DAMAS 99), Dublin, Ireland, pp. 320–327.

Marechal, J.C , 1972 . Variations in the modulus of elasticity and poisson's ratio with temperature. Concrete for nuclear reactors, ACI Special Publication SP-34, American Concrete Institute, Detroit, Michigan, Vol. 1, pp. 495-503.

Masri, S.F., Caughey, T.K., Nakamura, M., and Chassiakos, A.G. 1996. Neural network approach to detection of changes in structural parameters. Journal of Engineering Mechanics, American Society of Civil Engineers, **122**(4): 350-360.

MathCAD 14 User's Guide. Mathsoft, Inc. Cambridge, MA.

Mazurek, D.F., and DeWolf, J.T. 1990. Experimental study of bridge monitoring technique. Journal of Structural Engineering, American Society of Civil Engineers, **116**(9): 2532 - 2549.

Pandey, A.K., Biswas, M., and Samman, M.M. 1991. Damage detection from changes in curvature mode shapes. Journal of Sound and Vibration, **145**(2): 321-332.

Pandey, A.K., and Biswas, M. 1994. Damage detection in structures using changes in flexibility. Journal of Sound and Vibration, **169**(1): 3-17.

Peeters, B. 2000. System identification and damage detection in civil engineering. Ph.D. thesis, Department. of Civil Engineering, Katholieke Universiteit Leuven, Belgium.

Peeters, B., and De Roeck, G. 2000. One year monitoring of the Z24 bridge: environmental influences versus damage events. Proceeding of 18th International Modal Analysis Conference (IMAC), San Antonio, Texas, pp. 1570–1576.

Peeters, B., Maeck, J., and De Roeck, G. 2001. Vibration-based damage detection in civil engineering: excitation sources and temperature effects. Journal of Smart Materials and Structures, **10**: 518–527.

Proakis, J.G., and Manolakis, D.G. 1992. Digital signal processing-Principles, algorithms, and applications. Macmillan Publishing Company, New York.

Ramirez, R. 1985. The FFT: fundamentals and concepts. Prentice-Hall, Englewood Cliffs, New Jersey.

Rohrmann, R.G., Baessler, M., Said, S., Schmid, W., and Rucker, W.F. 2000. Structural causes of temperature affected modal data of civil structures obtained by long time monitoring. Proceeding of 18th International Modal Analysis Conference (IMAC), San Antonio, Texas, pp 1–7.

Rytter, A. 1993. Vibration based inspection of civil engineering structures. Ph.D. Dissertation, Department of Building Technology and Structural Engineering, Aalborg University, Denmark.

Salane, H.J., Baldwin, J.W., and Duffield, R.C. 1981. Dynamics approach for monitoring bridge deterioration. Transportation Research Record No. 832, National Academy of Sciences, Washington, District of Columbia, pp 21 - 28.

Salawu, O.S., and Williams, C. 1994. Damage location using vibration mode shapes. Proceedings of the 12th International Modal Analysis Conference, Society of Experimental Mechanics, Bethel, Connecticut, pp. 933-939.

Salawu O.S., and William, C. 1995. Bridge assessment using forced - vibration testing. Journal of Structural Engineering, American Society of Civil Engineers, **121**(2): 161- 173.

Salawu, O.S. 1997. Detection of structural damage through changes in frequency: a review. Journal of Engineering Structures, **19**(9): 718-723.

Samman, M.M., and Biswas, M. 1994a. Vibration testing for non-destructive evaluation of bridges. I: Theory. Journal of Structural Engineering, **120**(1): 269–289.

Samman, M.M., and Biswas, M. 1994b. Vibration testing for non-destructive evaluation of bridges. II: Results. Journal of Structural Engineering, **120**(1): 290–306.

Shah, S.P., and Ahmad, S.H. 1994. High performance concrete: properties and applications. McGraw-Hill, Inc., New York.

Shives, T.R. and Mertaugh, L.J. 1986. Detection, diagnosis and prognosis of rotating machinery to improve reliability, maintainability, and readiness through the application of new and innovative techniques. Cambridge University Press, Cambridge, UK.

Siddique, A.B., Wegner, L.D., and Sparling, B.F. 2005. Application of vibration-based damage detection to an integral abutment bridge. Proceedings of The International Society for Optical Engineering (SPIE) : Non-destructive Evaluation and Health Monitoring of Aerospace Materials, Composites, and Civil Infrastructure IV, San Diego, California, Vol. 5767, pp. 225-235.

Siddique, A.B., Wegner, L.D., and Sparling, B.F. 2006. Identifying damage on a bridge deck using vibration-based damage indices derived from limited measurements. Proceeding of The International Society for Optical Engineering (SPIE): Non-destructive Evaluation and Health Monitoring of Aerospace Materials, Composites, and Civil Infrastructure V, San Diego, California, Paper No. 6176-37.

Siddique, A B., Sparling, B. F., and Wegner, L. D. 2007. Assessment of vibration-based damage detection for an integral abutment bridge. Canadian Journal of Civil Engineering, **34**(3): 438-452.

Sohn, S., Dzonczyk, M., Straser, E.G., Kiremidjian, A.S., Law, K.H., and Meng, T. A. 1999. Experimental study of temperature effect on modal parameters of the Alamosa Canyon Bridge. Journal of Earthquake Engineering and Structural Dynamics, **28**: 879-897.

Sohn, H., Farrar, C. R., Hemez, F. M., Czarnecki, J. J., Shunk, D. D., Stinemates, D. W., and Nadler, B. R. 2003. A review of Structural Health Monitoring literature: 1996-2001. Report Number LA-13976-MS, Los Alamos National Laboratory, Los Alamos, New Mexico.

Srinivasan, M.G., and Kot, C.A. 1992. Effects of damage on the modal parameters of a cylindrical shell. Proceedings of the 10th International Modal Analysis Conference, Society of Experimental Mechanics, Bethel, Connecticut, pp. 529-535.

Stubbs, N., and Kim, Y.I. 1995. Field verification of a non-destructive damage localization and severity estimation algorithm. Proceedings of the 13th International Modal Analysis Conference, Society of Experimental Mechanics, Bethel, Connecticut, pp. 210-218.

Vining, G.G. 1998. Statistical methods for engineers. Brooks/Coles Publishing Company, Pacific Grove, California.

Wahab, M.A., and De Roeck, G.D. 1997. Effect of temperature on dynamic system parameters of a highway bridge. Journal of Structural Engineering International, **7**(4): 266–270.

Wang, M.L., Satpathi, D., and Heo, G. 1997. Damage detection of a model bridge using modal testing. Structural Health Monitoring: Current Status and Perspectives, CRC Press, F. K. Chang, pp. 589–602.

Watson, D.K., and Rajapakse, R.K.N.D. 2000. Seasonal variation in material properties of a flexible pavement. Canadian Journal of Civil Engineering, **27**(1): 44-54.

Wu, X., Ghaboussi, J., and Garrett, J.H. Jr. 1992. Use of neural networks in detection of structural damage. Journal of Computers and Structures, **42**(4): 649-659.

Yoder, E.J., and Witczak, M.W. 1975. Principles of Pavement Design, 2nd Edition, John Wiley and Sons, Inc., New York.

Zhang, Z., and Aktan, A.E. 1995. The damage indices for constructed facilities. Proceedings of the 13th International Modal Analysis Conference, Society of Experimental Mechanics, Bethel, Connecticut, pp. 1520-1529.

Zhou, Z., Wegner, L.D., and Sparling, B.F. 2003. Vibration-based damage detection on a steel-free bridge deck. Proceedings of the International Workshop on Structural Health Monitoring, Kitami, Japan, pp. 109-116.

Zhou, Z., Wegner, L.D., and Sparling, B.F. 2004.Vibration-based damage detection on a prestressed concrete girder. Proceedings of the 5th Canadian Society of Civil

Engineering Structural Specialty Conference, Saskatoon, Saskatchewan, paper ST-085.

Zhou, Z., Wegner, L.D., and Sparling, B.F. 2007. Vibration-based detection of small scale damage on a bridge deck. ASCE Journal of Structural Engineering, **133**(9): 1257-1267.

Zimmerman, D.C., and Kaouk, M. 1994. Structural damage detection using a minimum rank updates theory. Journal of Vibrations and Acoustics, American Society of Mechanical Engineers, **116**(2): 222-231.

APPENDIX A . MATERIAL PROPERTIES OF FINITE ELEMENT MODELS

Finite element models for the temperature ranges of 30°C to 40°C, 20°C to 26°C, 4°C to 7°C, -9°C to -7°C, and -12°C to -5°C were manually calibrated so that their natural frequencies and mode shapes matched those measured experimentally in the same temperature ranges. The values of material properties of the calibrated models in each temperature range are shown in Table A.1 through Table A.4. The material properties for the models at ambient temperatures of 35°C, 20°C, 5°C, -10°C, and -25°C are presented in Table A.5 through Table A.9.

Table A.1. Material properties for different structural elements of the FE model in temperature range of 30°C to 40°C.

Elements	Material	Material Model	Material Properties
Wearing Surface	Asphalt Concrete	Isotropic Linear Elastic	E^b=3.6 GPa, υ^c=0.34, ρ^d=2375 kg/m^3, α^e=2.5E-005 /°C
Bridge Deck	High Performance Reinforced Concrete	Orthotropic Linear Elastic	$E_1{}^a$= 22.85 GPa, E_2=3.16 GPa, E_3=22.85 GPa , $\upsilon_{12}{}^c$= 0.25, υ_{13}=0.21, υ_{23}=0.2, $G_{12}{}^b$=9.14 GPa, G_{13}=9.44 GPa, G_{23}=1.31 GPa, ρ^d=2400 kg/m^3
Median Deck and Barrier Walls	High Performance Reinforced Concrete	Isotropic Linear Elastic	E^b=26.88 GPa, υ^c=0.2, ρ^d=2400 kg/m^3, α^e=1.2E-005 /°C
Abutments	Normal Strength Reinforced Concrete	Isotropic Linear Elastic	E^b=24.68 GPa, υ^c=0.2, ρ^d =2400 kg/m^3, α^e=1.2E-005 /°C
Girders and Diaphragms	Mild Steel	Isotropic Linear Elastic	E^b=200 GPa, υ^c=0.3, ρ^d =7800 kg/m^3, α^e=1.24E-005 /°C
Pile Supports		Spring Element	$K_t{}^f$ = 4.46 N/m $K_\theta{}^f$= 90 N.m/rad.
Backfill Pressure		Spring Element	$K_t{}^f$ = 4.5x106 N/m

[a]Direction 1 = Along the width of the overpass
Direction 2 = Along the length of the overpass
Direction 3 = Along the vertical direction of the overpass
[b]E= Young's modulus of elasticity; G= Shear modulus
[e]α= Coefficient of thermal expansion
[c]υ= Poisson's ratio; [d]ρ= Density
[f]K_t= Translational stiffness; [f]K_θ = Rotational stiffness

Table A.2. Material properties for different structural elements of the FE model in temperature range of 4°C to 7°C.

Elements	Material	Material Model	Material Properties
Wearing Surface	Asphalt Concrete	Isotropic Linear Elastic	E^b=12.8 GPa, υ^c=0.24, ρ^d=2375 kg/m^3, α^e=2.5E-005 /°C
Bridge Deck	High Performance Reinforced Concrete	Orthotropic Linear Elastic	$E_1{}^a$= 26.82 GPa, E_2=3.7 GPa, E_3=26.82 GPa , $\upsilon_{12}{}^c$= 0.25, υ_{13}=0.21, υ_{23}=0.2, $G_{12}{}^b$=10.73 GPa, G_{13}=11.08 GPa, G_{23}=1.54 GPa, ρ^d=2400 kg/m^3
Median Deck and Barrier Walls	High Performance Reinforced Concrete	Isotropic Linear Elastic	E^b=31.56 GPa, υ^c=0.2, ρ^d=2400 kg/m^3, α^e=1.2E-005 /°C
Abutments	Normal Strength Reinforced Concrete	Isotropic Linear Elastic	E^b=28.87 GPa, υ^c=0.2, ρ^d =2400 kg/m^3, α^e=1.2E-005 /°C
Girders and Diaphragms	Mild Steel	Isotropic Linear Elastic	E^b=200 GPa, υ^c=0.3, ρ^d =7800 kg/m^3, α^e=1.24E-005 /°C
Pile Supports		Spring Element	$K_t{}^f$ = 4.46 N/m $K_\theta{}^f$= 90 N.m/rad.
Backfill Pressure		Spring Element	$K_t{}^f$ = 4.5x106 N/m

[a]Direction 1 = Along the width of the overpass
Direction 2 = Along the length of the overpass
Direction 3 = Along the vertical direction of the overpass
[b]E= Young's modulus of elasticity; G= Shear modulus
[e]α= Coefficient of thermal expansion
[c]υ= Poisson's ratio; [d]ρ= Density
[f]K_t= Translational stiffness; [f]K_θ = Rotational stiffness

Table A.3. Material properties for different structural elements of the FE model in temperature range of -9°C to -7°C.

Elements	Material	Material Model	Material Properties
Wearing Surface	Asphalt Concrete	Isotropic Linear Elastic	E^b=36 GPa, υ^c=0.15, ρ^d=2375 kg/m^3, α^e=2.5E-005 /°C
Bridge Deck	High Performance Reinforced Concrete	Orthotropic Linear Elastic	$E_1{}^a$= 27.66 GPa, E_2=3.82 GPa, E_3=27.66 GPa , $\upsilon_{12}{}^c$= 0.25, υ_{13}=0.21, υ_{23}=0.2, $G_{12}{}^b$=11.07 GPa, G_{13}=11.43 GPa, G_{23}=1.59 GPa, ρ^d=2400 kg/m^3
Median Deck and Barrier Walls	High Performance Reinforced Concrete	Isotropic Linear Elastic	E^b=32.55 GPa, υ^c=0.2, ρ^d=2400 kg/m^3, α^e=1.2E-005 /°C
Abutments	Normal Strength Reinforced Concrete	Isotropic Linear Elastic	E^b=30.45 GPa, υ^c=0.2, ρ^d =2400 kg/m^3, α^e=1.2E-005 /°C
Girders and Diaphragms	Mild Steel	Isotropic Linear Elastic	E^b=200 GPa, υ^c=0.3, ρ^d =7800 kg/m^3, α^e=1.24E-005 /°C
Pile Supports		Spring Element	$K_t{}^f$ = 4.46 N/m $K_\theta{}^f$= 90 N.m/rad.
Backfill Pressure		Spring Element	$K_t{}^f$ = 4.5x106 N/m

[a]Direction 1 = Along the width of the overpass
Direction 2 = Along the length of the overpass
Direction 3 = Along the vertical direction of the overpass
[b]E= Young's modulus of elasticity; G= Shear modulus
[e]α= Coefficient of thermal expansion
[c]υ= Poisson's ratio; [d]ρ= Density
[f]K_t= Translational stiffness; [f]K_θ = Rotational stiffness

Table A.4. Material properties for different structural elements of the FE model in temperature range of -12°C to -5°C.

Elements	Material	Material Model	Material Properties
Wearing Surface	Asphalt Concrete	Isotropic Linear Elastic	E^b=45 GPa, υ^c=0.14, ρ^d=2375 kg/m^3, α^e=2.5E-005 /°C
Bridge Deck	High Performance Reinforced Concrete	Orthotropic Linear Elastic	$E_1{}^a$= 27.8 GPa, E_2=3.84 GPa, E_3=27.8 GPa , $\upsilon_{12}{}^c$= 0.25, υ_{13}=0.21, υ_{23}=0.2, $G_{12}{}^b$=11.12 GPa, G_{13}=11.49 GPa, G_{23}=1.6 GPa, ρ^d=2400 kg/m^3
Median Deck and Barrier Walls	High Performance Reinforced Concrete	Isotropic Linear Elastic	E^b=32.71 GPa, υ^c=0.2, ρ^d=2400 kg/m^3, α^e=1.2E-005 /°C
Abutments	Normal Strength Reinforced Concrete	Isotropic Linear Elastic	E^b=30.7 GPa, υ^c=0.2, ρ^d =2400 kg/m^3, α^e=1.2E-005 /°C
Girders and Diaphragms	Mild Steel	Isotropic Linear Elastic	E^b=200 GPa, υ^c=0.3, ρ^d =7800 kg/m^3, α^e=1.24E-005 /°C
Pile Supports		Spring Element	$K_t{}^f$ = 4.46 N/m $K_\theta{}^f$= 90 N.m/rad.
Backfill Pressure		Spring Element	$K_t{}^f$ = 4.5x106 N/m

[a]Direction 1 = Along the width of the overpass
Direction 2 = Along the length of the overpass
Direction 3 = Along the vertical direction of the overpass
[b]E= Young's modulus of elasticity; G= Shear modulus
[e]α= Coefficient of thermal expansion
[c]υ= Poisson's ratio; [d]ρ= Density
[f]K_t= Translational stiffness; [f]K_θ = Rotational stiffness

Table A.5. Material properties for different structural elements of the FE model at 35°C.

Elements	Material	Material Model	Material Properties
Wearing Surface	Asphalt Concrete	Isotropic Linear Elastic	E^b=3.2 GPa, υ^c=0.37, ρ^d=2375 kg/m^3, α^e=2.5E-005 /°C
Bridge Deck	High Performance Reinforced Concrete	Orthotropic Linear Elastic	$E_1{}^a$= 21.44 GPa, E_2=2.97 GPa, E_3=21.44 GPa , $\upsilon_{12}{}^c$= 0.25, υ_{13}=0.21, υ_{23}=0.2, $G_{12}{}^b$=8.57 GPa, G_{13}=8.86 GPa, G_{23}=1.23 GPa, ρ^d=2400 kg/m^3
Median Deck and Barrier Walls	High Performance Reinforced Concrete	Isotropic Linear Elastic	E^b=25.23 GPa, υ^c=0.2, ρ^d=2400 kg/m^3, α^e=1.2E-005 /°C
Abutments	Normal Strength Reinforced Concrete	Isotropic Linear Elastic	E^b=23.71 GPa, υ^c=0.2, ρ^d =2400 kg/m^3, α^e=1.2E-005 /°C
Girders and Diaphragms	Mild Steel	Isotropic Linear Elastic	E^b=200 GPa, υ^c=0.3, ρ^d =7800 kg/m^3, α^e=1.24E-005 /°C
Pile Supports		Spring Element	$K_t{}^f$ = 4.46 N/m $K_\theta{}^f$= 90 N.m/rad.
Backfill Pressure		Spring Element	$K_t{}^f$ = 4.5x106 N/m

[a]Direction 1 = Along the width of the overpass
Direction 2 = Along the length of the overpass
Direction 3 = Along the vertical direction of the overpass
[b]E= Young's modulus of elasticity; G= Shear modulus
[e]α= Coefficient of thermal expansion
[c]υ= Poisson's ratio; [d]ρ= Density
[f]K_t= Translational stiffness; [f]K_θ = Rotational stiffness

Table A.6. Material properties for different structural elements of the FE model at 20°C.

Elements	Material	Material Model	Material Properties
Wearing Surface	Asphalt Concrete	Isotropic Linear Elastic	E^b=4.1 GPa, υ^c=0.31, ρ^d=2375 kg/m^3, α^e=2.5E-005 /°C
Bridge Deck	High Performance Reinforced Concrete	Orthotropic Linear Elastic	$E_1{}^a$= 25.66 GPa, E_2=3.54 GPa, E_3=25.66 GPa , $\upsilon_{12}{}^c$= 0.25, υ_{13}=0.21, υ_{23}=0.2, $G_{12}{}^b$=10.26 GPa, G_{13}=10.6 GPa, G_{23}=1.48 GPa, ρ^d=2400 kg/m^3
Median Deck and Barrier Walls	High Performance Reinforced Concrete	Isotropic Linear Elastic	E^b=30.19 GPa, υ^c=0.2, ρ^d=2400 kg/m^3, α^e=1.2E-005 /°C
Abutments	Normal Strength Reinforced Concrete	Isotropic Linear Elastic	E^b=26.62 GPa, υ^c=0.2, ρ^d =2400 kg/m^3, α^e=1.2E-005 /°C
Girders and Diaphragms	Mild Steel	Isotropic Linear Elastic	E^b=200 GPa, υ^c=0.3, ρ^d =7800 kg/m^3, α^e=1.24E-005 /°C
Pile Supports		Spring Element	$K_t{}^f$ = 4.46 N/m $K_\theta{}^f$= 90 N.m/rad.
Backfill Pressure		Spring Element	$K_t{}^f$ = 4.5x106 N/m

[a]Direction 1 = Along the width of the overpass
Direction 2 = Along the length of the overpass
Direction 3 = Along the vertical direction of the overpass
[b]E= Young's modulus of elasticity; G= Shear modulus
[e]α= Coefficient of thermal expansion
[c]υ= Poisson's ratio; [d]ρ= Density
[f]K_t= Translational stiffness; [f]K_θ = Rotational stiffness

Table A.7. Material properties for different structural elements of the FE model at 5°C.

Elements	Material	Material Model	Material Properties
Wearing Surface	Asphalt Concrete	Isotropic Linear Elastic	E^b=11.8 GPa, υ^c=0.24, ρ^d=2375 kg/m^3, α^e=2.5E-005 /°C
Bridge Deck	High Performance Reinforced Concrete	Orthotropic Linear Elastic	$E_1{}^a$= 26.75 GPa, E_2=3.67 GPa, E_3=26.75 GPa , $\upsilon_{12}{}^c$= 0.25, υ_{13}=0.21, υ_{23}=0.2, $G_{12}{}^b$=10.7 GPa, G_{13}=10.05 GPa, G_{23}=1.54 GPa, ρ^d=2400 kg/m^3
Median Deck and Barrier Walls	High Performance Reinforced Concrete	Isotropic Linear Elastic	E^b=31.74 GPa, υ^c=0.2, ρ^d=2400 kg/m^3, α^e=1.2E-005 /°C
Abutments	Normal Strength Reinforced Concrete	Isotropic Linear Elastic	E^b=28.73 GPa, υ^c=0.2, ρ^d =2400 kg/m^3, α^e=1.2E-005 /°C
Girders and Diaphragms	Mild Steel	Isotropic Linear Elastic	E^b=200 GPa, υ^c=0.3, ρ^d =7800 kg/m^3, α^e=1.24E-005 /°C
Pile Supports		Spring Element	$K_t{}^f$ = 4.46 N/m $K_\theta{}^f$= 90 N.m/rad.
Backfill Pressure		Spring Element	$K_t{}^f$ = 4.5x106 N/m

[a]Direction 1 = Along the width of the overpass
Direction 2 = Along the length of the overpass
Direction 3 = Along the vertical direction of the overpass
[b]E= Young's modulus of elasticity; G= Shear modulus
[e]α= Coefficient of thermal expansion
[c]υ= Poisson's ratio; [d]ρ= Density
[f]K_t= Translational stiffness; [f]K_θ = Rotational stiffness

Table A.8. Material properties for different structural elements of the FE model at -10°C.

Elements	Material	Material Model	Material Properties
Wearing Surface	Asphalt Concrete	Isotropic Linear Elastic	E^b=45 GPa, υ^c=0.14, ρ^d=2375 kg/m^3, α^e=2.5E-005 /°C
Bridge Deck	High Performance Reinforced Concrete	Orthotropic Linear Elastic	$E_1{}^a$= 27.8 GPa, E_2=3.84 GPa, E_3=27.8 GPa , $\upsilon_{12}{}^c$= 0.25, υ_{13}=0.21, υ_{23}=0.2, $G_{12}{}^b$=11.12 GPa, G_{13}=11.49 GPa, G_{23}=1.6 GPa, ρ^d=2400 kg/m^3
Median Deck and Barrier Walls	High Performance Reinforced Concrete	Isotropic Linear Elastic	E^b=32.71 GPa, υ^c=0.2, ρ^d=2400 kg/m^3, α^e=1.2E-005 /°C
Abutments	Normal Strength Reinforced Concrete	Isotropic Linear Elastic	E^b=30.7 GPa, υ^c=0.2, ρ^d =2400 kg/m^3, α^e=1.2E-005 /°C
Girders and Diaphragms	Mild Steel	Isotropic Linear Elastic	E^b=200 GPa, υ^c=0.3, ρ^d =7800 kg/m^3, α^e=1.24E-005 /°C
Pile Supports		Spring Element	$K_t{}^f$ = 4.46 N/m $K_\theta{}^f$= 90 N.m/rad.
Backfill Pressure		Spring Element	$K_t{}^f$ = 4.5x106 N/m

[a]Direction 1 = Along the width of the overpass
Direction 2 = Along the length of the overpass
Direction 3 = Along the vertical direction of the overpass
[b]E= Young's modulus of elasticity; G= Shear modulus
[e]α= Coefficient of thermal expansion
[c]υ= Poisson's ratio; [d]ρ= Density
[f]K_t= Translational stiffness; [f]K_θ = Rotational stiffness

Table A.9. Material properties for different structural elements of the FE model at -25°C.

Elements	Material	Material Model	Material Properties
Wearing Surface	Asphalt Concrete	Isotropic Linear Elastic	E^b=93 GPa, υ^c=0.125, ρ^d=2375 kg/m^3, α^e=2.5E-005 /°C
Bridge Deck	High Performance Reinforced Concrete	Orthotropic Linear Elastic	$E_1{}^a$= 28.81 GPa, E_2=3.98 GPa, E_3=28.81 GPa , $\upsilon_{12}{}^c$= 0.25, υ_{13}=0.21, υ_{23}=0.2, $G_{12}{}^b$=11.53 GPa, G_{13}=11.9 GPa, G_{23}=1.66 GPa, ρ^d=2400 kg/m^3
Median Deck and Barrier Walls	High Performance Reinforced Concrete	Isotropic Linear Elastic	E^b=33.9 GPa, υ^c=0.2, ρ^d=2400 kg/m^3, α^e=1.2E-005 /°C
Abutments	Normal Strength Reinforced Concrete	Isotropic Linear Elastic	E^b=32.55 GPa, υ^c=0.2, ρ^d =2400 kg/m^3, α^e=1.2E-005 /°C
Girders and Diaphragms	Mild Steel	Isotropic Linear Elastic	E^b=200 GPa, υ^c=0.3, ρ^d =7800 kg/m^3, α^e=1.24E-005 /°C
Pile Supports		Spring Element	$K_t{}^f$ = 4.46 N/m $K_\theta{}^f$= 90 N.m/rad.
Backfill Pressure		Spring Element	$K_t{}^f$ = 4.5x106 N/m

[a]Direction 1 = Along the width of the overpass
Direction 2 = Along the length of the overpass
Direction 3 = Along the vertical direction of the overpass
[b]E= Young's modulus of elasticity; G= Shear modulus
[e]α= Coefficient of thermal expansion
[c]υ= Poisson's ratio; [d]ρ= Density
[f]K_t= Translational stiffness; [f]K_θ = Rotational stiffness

APPENDIX B . MEASURED MODE SHAPES OF ATTRIDGE DRIVE OVERPASS

The second and third measured mode shapes for every temperature range are shown in Figure B.1 and B.2, respectively.

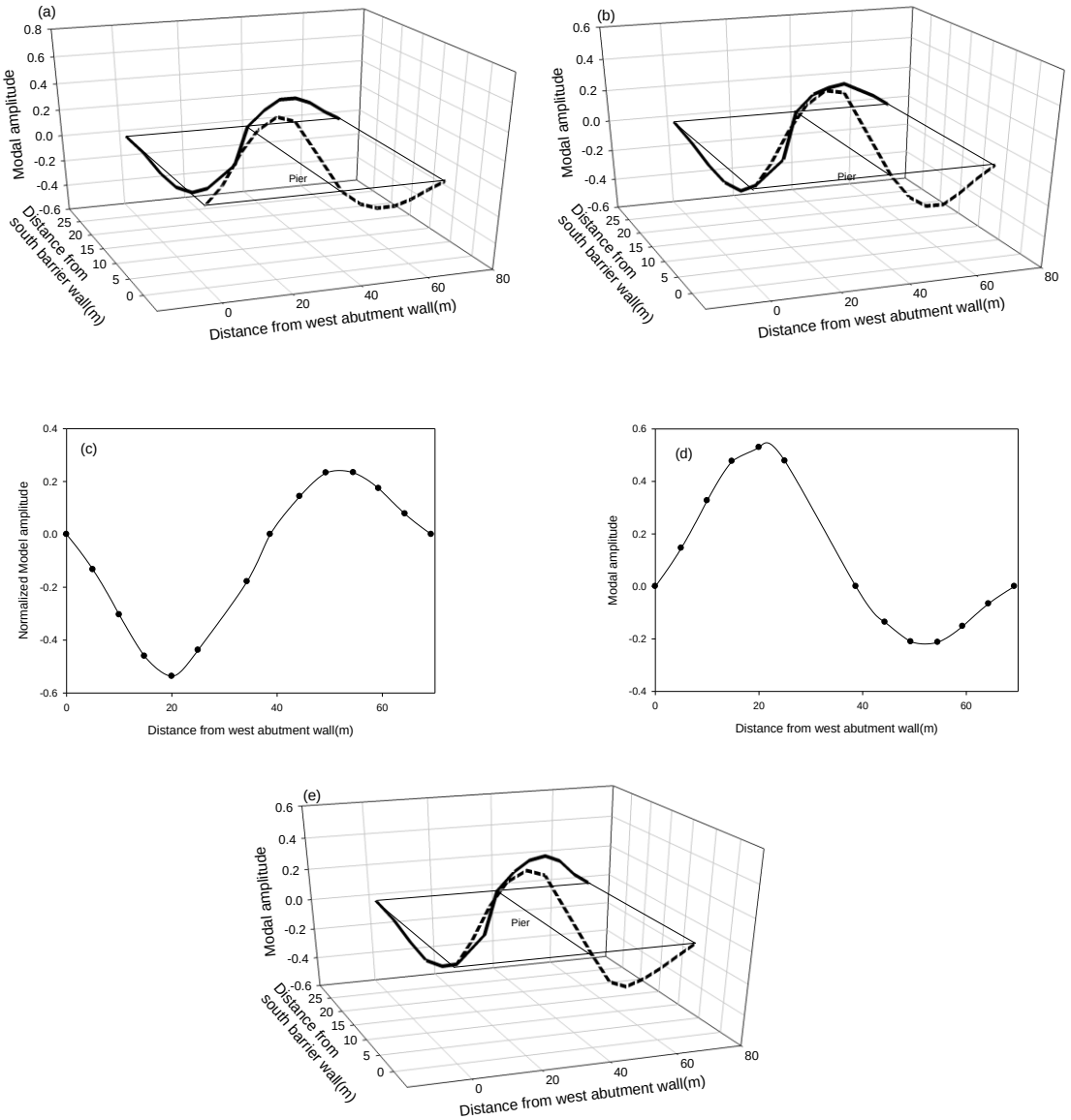

Figure B.1. Second experimental mode shapes of the bridge in the ambient temperature ranges of: (a) 20°C to 26°C; (b) - 9°C to -7°C; (c) 4°C to 7°C (north side of overpass); (d) 30°C to 40°C (south side of overpass); and (e) -12°C to -5°C.

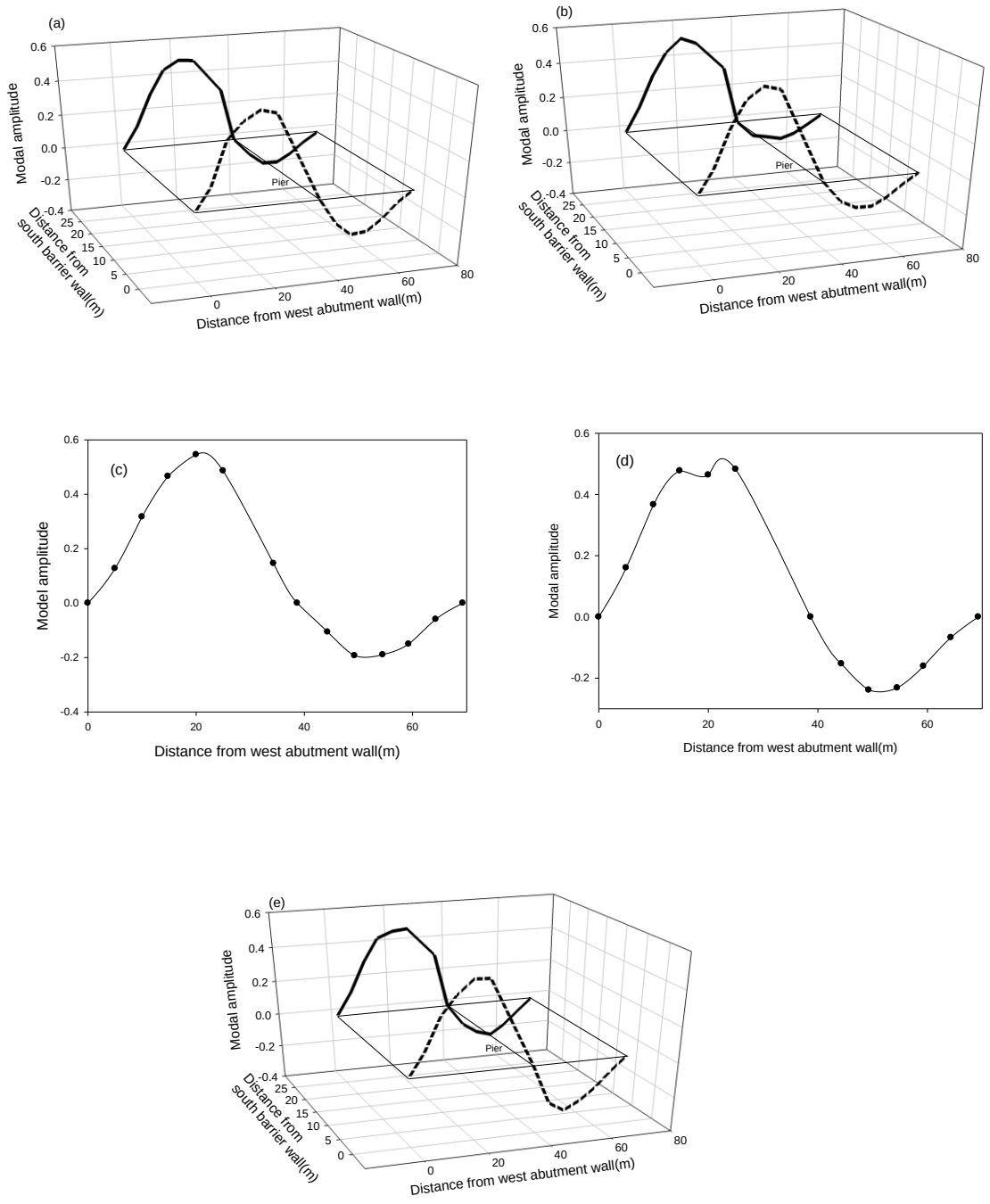

Figure B.2. Third experimental mode shapes of the bridge in the ambient temperature ranges of: (a) 20°C to 26°C; (b) - 9°C to -7°C; (c) 4°C to 7°C (north side of overpass); (d) 30°C to 40°C (south side of overpass); and (e) -12°C to -5°C.

APPENDIX C . VARIABILITY IN MEASURED MODE SHAPES

The means and standard deviations of the measured mode shape amplitudes at each sensor location of the first three modes of the bridge for the temperature ranges of -12°C to -5°C, -9°C to -7°C, 4°C to 7°C, and 30°C to 40°C are shown in Table C.1 through Table C.4. The means and standard deviations of the measured mode shapes are also shown in Figure C.1 through Figure C.4.

Table C.1. Variability in the first three measured mode shapes in the temperature range of -12°C to -5°C.

Mode			Sensor location from the west abutment (m)									
no.			5	10	14.8	20	25	44.3	49.3	54.5	59.3	64.3
1st	North Side	Avg	0.463	1.032	1.501	N/A	1.710	-0.439	N/A	-0.682	-0.520	-0.263
		SD	0.027	0.027	0.104	N/A	0.092	0.146	N/A	0.237	0.167	0.086
	South Side	Avg	0.274	0.620	0.829	N/A	0.988	-0.302	N/A	-0.334	-0.225	-0.135
		SD	0.090	0.175	0.290	N/A	0.200	0.186	N/A	0.169	0.124	0.057
2nd	North Side	Avg	-0.448	-1.006	-1.471	N/A	-1.635	0.396	N/A	0.695	0.560	0.225
		SD	0.074	0.162	0.290	N/A	0.341	0.118	N/A	0.070	0.033	0.087
	South Side	Avg	-0.523	-1.195	-1.646	N/A	-1.714	0.651	N/A	0.663	0.472	0.232
		SD	0.065	0.148	0.252	N/A	0.206	0.108	N/A	0.115	0.082	0.043
3rd	North Side	Avg	0.423	0.976	1.383	N/A	1.518	-0.399	N/A	-0.660	-0.488	-0.237
		SD	0.035	0.058	0.065	N/A	0.148	0.098	N/A	0.126	0.086	0.053
	South Side	Avg	0.389	0.924	1.223	N/A	1.437	-0.676	N/A	-0.687	-0.494	-0.231
		SD	0.089	0.176	0.252	N/A	0.208	0.218	N/A	0.224	0.155	0.072

Avg = Average; SD= Standard Deviation.

Table C.2. Variability in the first three measured mode shapes in the temperature range of -9°C to -7°C.

Mode no.			Sensor location from the west abutment (m)									
			5	10	14.8	20	25	44.3	49.3	54.5	59.3	64.3
1st	North Side	Avg	0.500	1.048	1.450	N/A	1.593	-0.404	N/A	-0.612	-0.492	-0.268
		SD	0.065	0.180	0.340	N/A	0.288	0.009	N/A	0.031	0.016	0.002
	South Side	Avg	0.430	0.972	1.378	N/A	1.524	-0.478	N/A	-0.678	-0.499	-0.245
		SD	0.094	0.203	0.303	N/A	0.397	0.116	N/A	0.145	0.120	0.078
2nd	North Side	Avg	-0.459	-0.972	-1.374	N/A	-1.507	0.341	N/A	0.511	0.362	0.209
		SD	0.080	0.178	0.334	N/A	0.279	0.084	N/A	0.103	0.064	0.045
	South Side	Avg	0.505	1.162	1.652	N/A	1.847	-0.525	N/A	-0.777	-0.549	-0.252
		SD	0.081	0.163	0.244	N/A	0.325	0.145	N/A	0.276	0.158	0.055
3rd	North Side	Avg	0.429	0.959	1.343	N/A	1.468	-0.281	N/A	-0.387	-0.309	-0.161
		SD	0.101	0.164	0.367	N/A	0.273	0.071	N/A	0.117	0.068	0.050
	South Side	Avg	0.415	1.026	1.453	N/A	1.573	-0.358	N/A	-0.507	-0.374	-0.175
		SD	0.094	0.210	0.295	N/A	0.323	0.051	N/A	0.089	0.072	0.026

Avg = Average; SD= Standard Deviation.

Table C.3. Variability in the first three measured mode shapes in the temperature range of 4°C to 7°C.

Mode no.			Sensor location from the west abutment (m)									
			5	10	14.8	20	25	44.3	49.3	54.5	59.3	64.3
1st	North	Avg	0.533	1.596	2.376	2.974	2.106	-0.603	-0.971	-0.958	-0.807	-0.382
	Side	SD	0.243	0.559	0.457	0.577	0.708	0.030	0.025	0.022	0.080	0.028
2nd	North	Avg	-0.547	-1.250	-1.895	-2.209	-1.801	0.590	0.957	0.961	0.715	0.320
	Side	SD	0.162	0.356	0.552	0.680	0.498	0.022	0.016	0.021	0.041	0.009
3rd	North	Avg	0.642	1.598	2.350	2.751	2.450	-0.535	-0.973	-0.956	-0.758	-0.299
	Side	SD	0.192	0.498	0.722	0.749	0.774	0.055	0.010	0.059	0.147	0.032

Avg = Average; SD= Standard Deviation.

Table C.4. Variability in the first three measured mode shapes in the temperature range of 30°C to 40°C.

Mode no.			Sensor location from the west abutment (m)									
			5	10	14.8	20	25	44.3	49.3	54.5	59.3	64.3
1st	South	Avg	0.428	0.934	1.156	1.023	1.146	-0.400	-0.616	-0.630	-0.469	-0.228
	Side	SD	0.068	0.157	0.111	0.418	0.179	0.067	0.099	0.100	0.079	0.041
2nd	South	Avg	0.547	1.226	1.789	1.987	1.794	-0.511	-0.791	-0.799	-0.571	-0.248
	Side	SD	0.070	0.195	0.368	0.548	0.461	0.025	0.080	0.100	0.052	0.032
3rd	South	Avg	0.434	0.991	1.291	1.255	1.306	-0.414	-0.646	-0.627	-0.436	-0.183
	Side	SD	0.077	0.177	0.157	0.295	0.178	0.056	0.079	0.064	0.067	0.037

Avg = Average; SD= Standard Deviation.

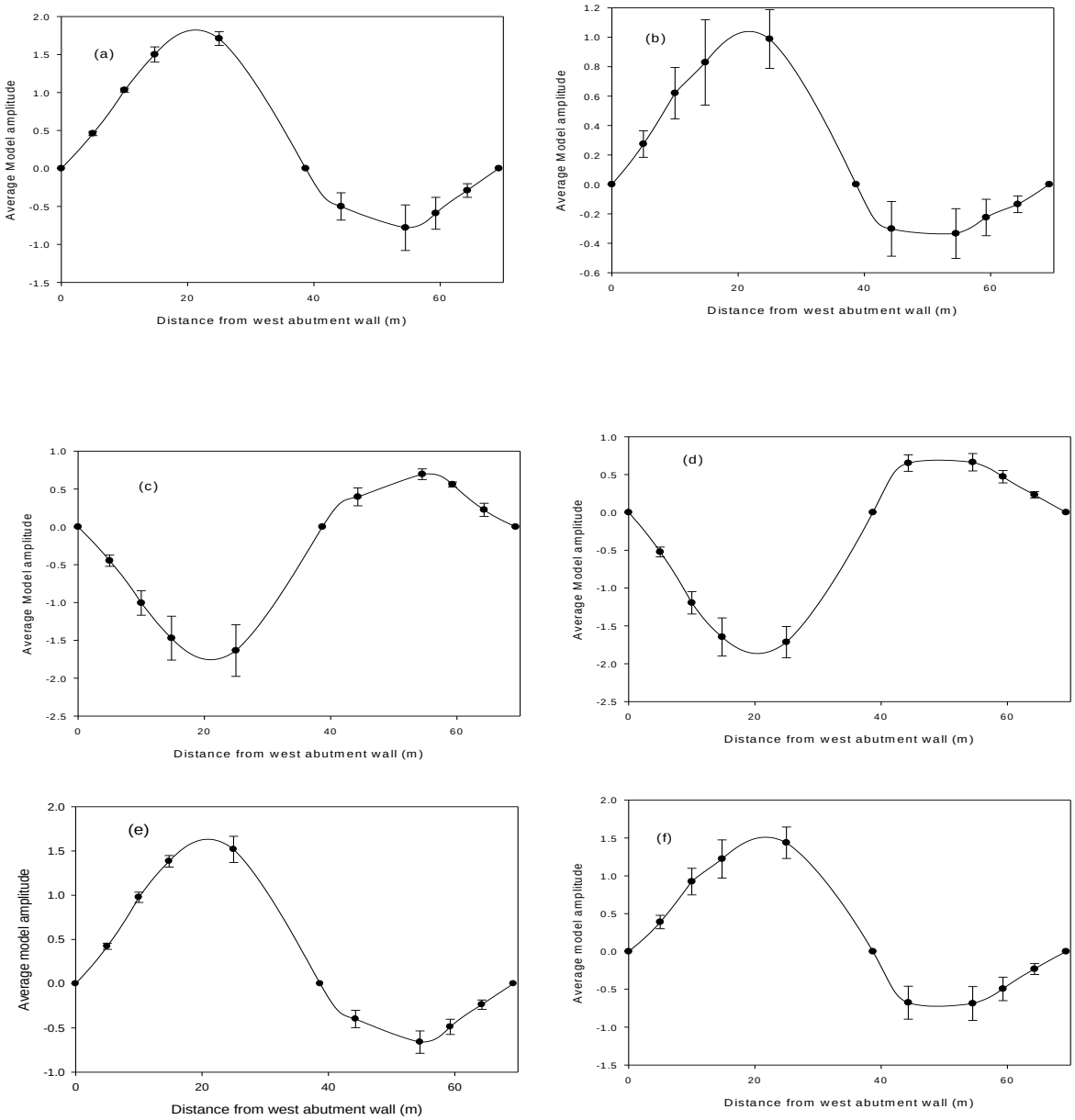

Figure C.1. Mode shape variability at individual sensor locations of the bridge for the temperature range of -12°C to -5°C: (a) 1st mode shape along the north side; (b) 1st mode shape along the south side; (c) 2nd mode shape along the north side; (d) 2nd mode shape along the south side; (e) 3rd mode shape along the north side; and (f) 3rd mode shape along the south side.

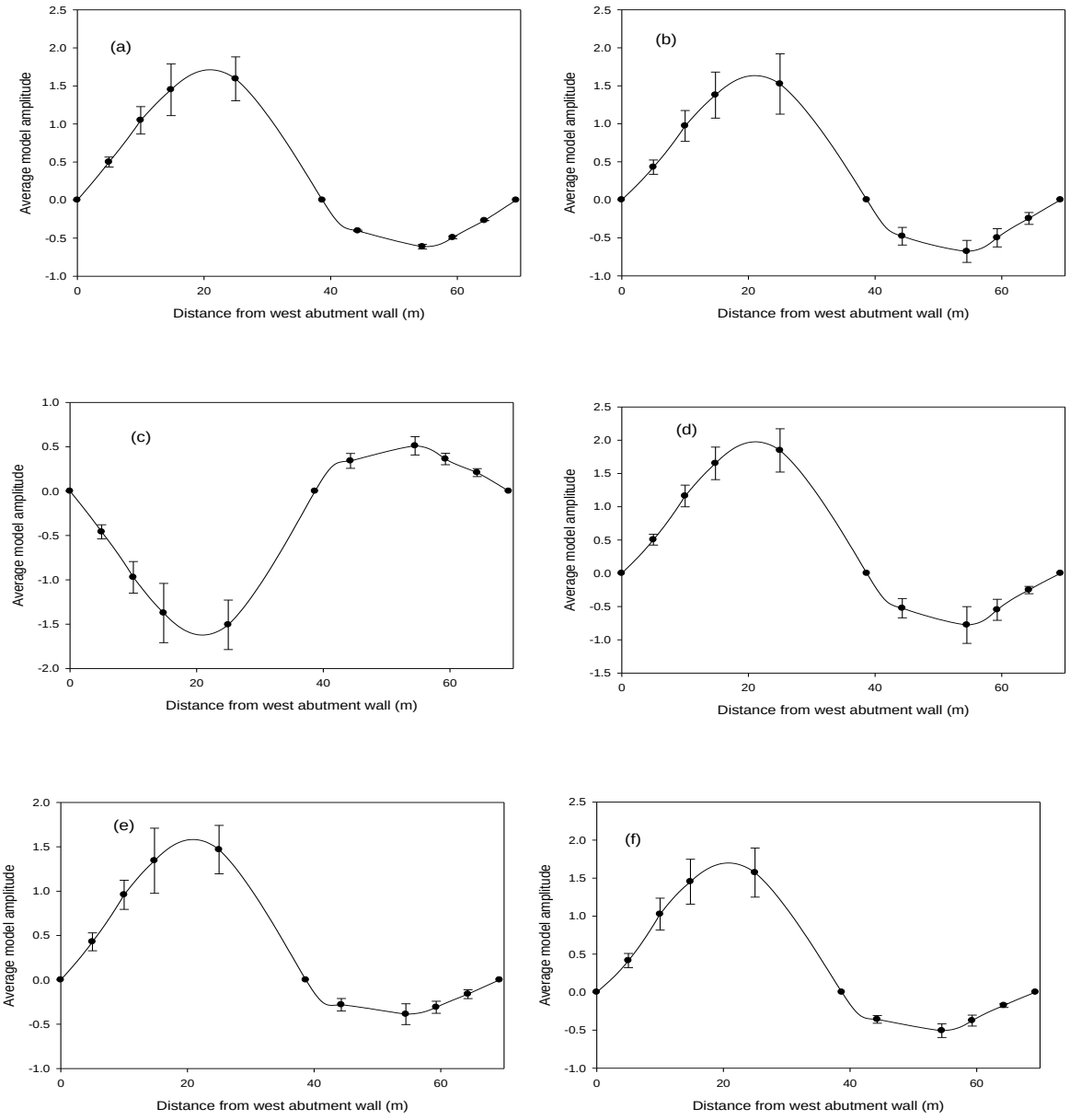

Figure C.2. Mode shape variability at individual sensor locations of the bridge for the temperature range of -9°C to -7°C: (a) 1st mode shape along the north side; (b) 1st mode shape along the south side; (c) 2nd mode shape along the north side; (d) 2nd mode shape along the south side; (e) 3rd mode shape along the north side; and (f) 3rd mode shape along the south side.

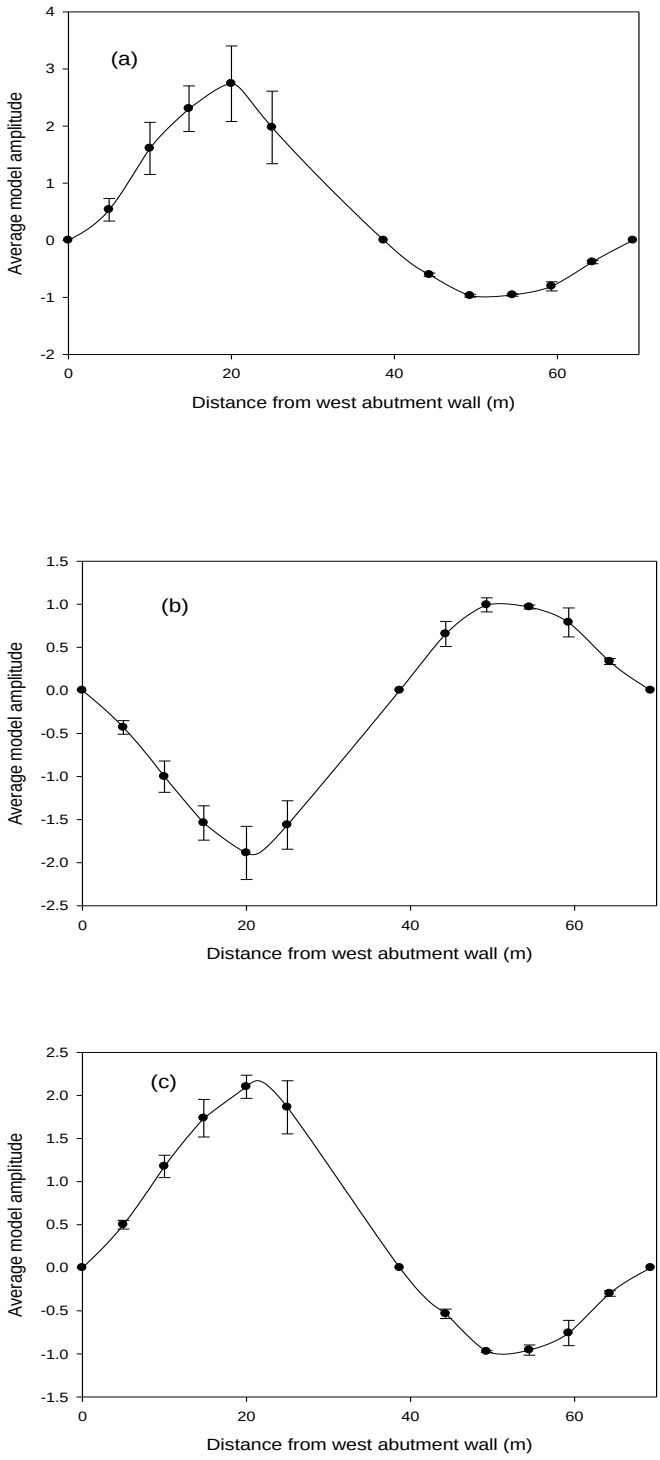

Figure C.3. Mode shape variability at individual sensor locations of the bridge for the temperature range of 4°C to 7°C: (a) 1st mode shape along the north side; (b) 2nd mode shape along the north side; and (c) 3rd mode shape along the north side.

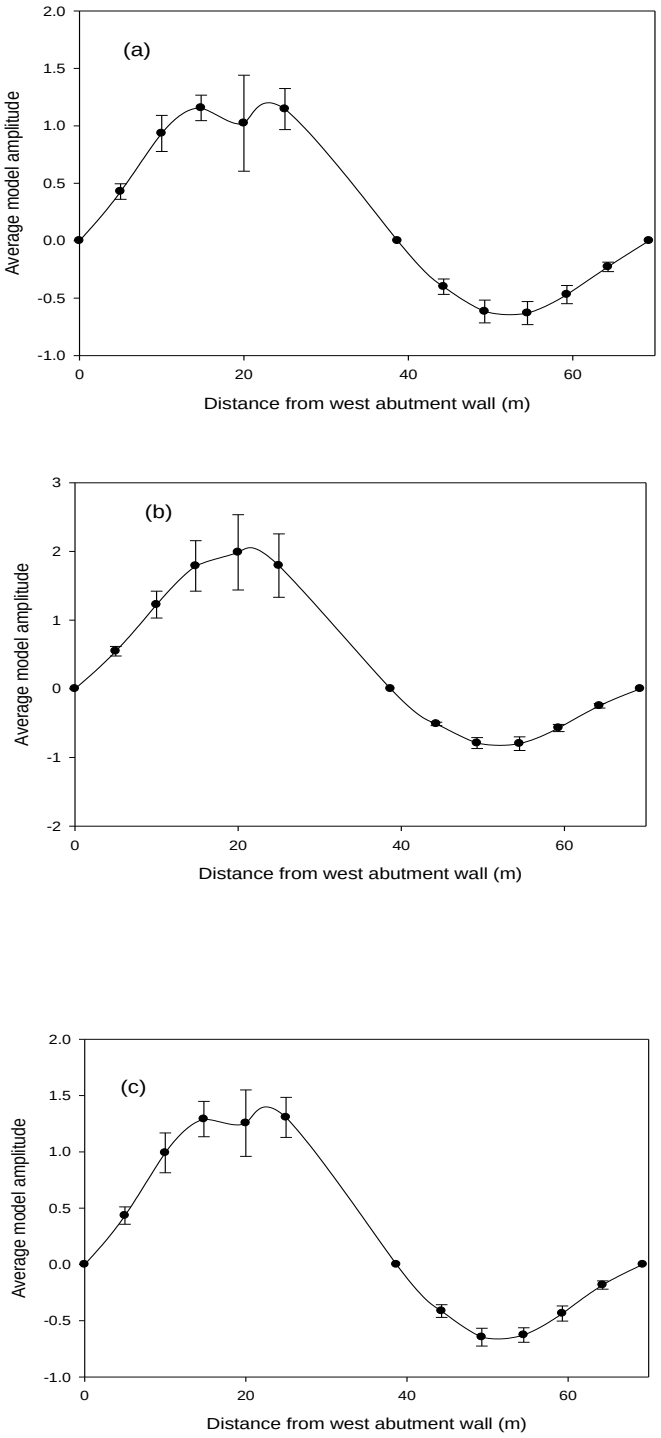

Figure C.4. Mode shape variability at individual sensor locations of the bridge for the temperature range of 30°C to 40°C: (a) 1st mode shape along the south side; (b) 2nd mode shape along the south side; and (c) 3rd mode shape along the south side.

APPENDIX D . STUDENT'S T-TEST CALCULATION AND RESULTS

This is an example of Student's t-test on mean values of first mode shape amplitudes in the temperature range of 20^{o}C to 26^{o}C in comparison to mean values of fundamental mode shape amplitudes in the temperature range of 30^{o}C to 40^{o}C. The data used in this calculation were taken from Table 5.2 and Table C.4. Calculations were performed using MathCAD (version 14).

The sensor locations, mean values, and standard deviations of mode shape amplitudes, and the number of readings at a given sensor for the temperature ranges of 20^{o}C to 26^{o}C and 30^{o}C to 40^{o}C are presented in the respective rows of the matrices shown.

Data for first mode shape (south side) in the temperature range of 30^{o}C to 40^{o}C:

$$a1 := \begin{pmatrix} 5 & 10 & 14.8 & 20 & 25 & 44.3 & 49.3 & 54.5 & 59.3 & 64.3 \\ 0.428 & 0.934 & 1.156 & 1.023 & 1.146 & -0.4 & -0.616 & -0.63 & -0.469 & -0.228 \\ 0.068 & 0.157 & 0.111 & 0.418 & 0.179 & 0.067 & 0.099 & 0.1 & 0.079 & 0.041 \\ 3 & 3 & 3 & 3 & 3 & 7 & 7 & 7 & 7 & 7 \end{pmatrix}$$

Data for first mode shape (south side) in the temperature range 20^{o}C to 26^{o}C:

$$b1 := \begin{pmatrix} 5 & 10 & 14.8 & 20 & 25 & 44.3 & 49.3 & 54.5 & 59.3 & 64.3 \\ 0.375 & 0.856 & 1.178 & 1.28 & 1.194 & -0.375 & -0.515 & -0.524 & -0.407 & -0.22 \\ 0.061 & 0.148 & 0.209 & 0.277 & 0.219 & 0.095 & 0.132 & 0.151 & 0.105 & 0.056 \\ 5 & 5 & 5 & 5 & 5 & 5 & 5 & 5 & 5 & 5 \end{pmatrix}$$

The two-tailed significance level:

$\alpha := 0.0125$

Standard deviations of mode shape amplitudes at each sensor location for temperature ranges of 20^{o}C to 26^{o}C and 30^{o}C to 40^{o}C:

$$\left(a1^{T}\right)^{\langle 2\rangle} =$$

	0
0	0.068
1	0.157
2	0.111
3	0.418
4	0.179
5	0.067
6	0.099
7	0.1
8	0.079
9	0.041

$$\left(b1^{T}\right)^{\langle 2\rangle} =$$

	0
0	0.061
1	0.148
2	0.209
3	0.277
4	0.219
5	0.095
6	0.132
7	0.151
8	0.105
9	0.056

Degrees of freedom:

$$\nu 1 := \left(a1^{T}\right)^{\langle 3\rangle} + \left(b1^{T}\right)^{\langle 3\rangle} - 2$$

$$\nu 1 =$$

	0
0	6
1	6
2	6
3	6
4	6
5	10
6	10
7	10
8	10
9	10

Standard error of the difference between mean values:

$$s1 := \left| \begin{array}{l} \text{for } i \in 0 .. \text{length}(\nu 1) - 1 \\ s1_i \leftarrow \sqrt{\dfrac{\left[\left[\left(a1^{T}\right)^{\langle 3\rangle}\right]_i - 1\right] \cdot \left[\left[\left(a1^{T}\right)^{\langle 2\rangle}\right]_i\right]^2 \ldots + \left[\left[\left(b1^{T}\right)^{\langle 3\rangle}\right]_i - 1\right] \cdot \left[\left[\left(b1^{T}\right)^{\langle 2\rangle}\right]_i\right]^2}{\nu 1_i} \cdot \left[\dfrac{1}{\left[\left(a1^{T}\right)^{\langle 3\rangle}\right]_i} + \dfrac{1}{\left[\left(b1^{T}\right)^{\langle 3\rangle}\right]_i}\right]} \\ s1 \end{array} \right.$$

$s1 =$

	0
0	0.046
1	0.11
2	0.133
3	0.242
4	0.151
5	0.046
6	0.066
7	0.072
8	0.053
9	0.028

The variable t in t-test:

$$t1 := \left| \begin{array}{l} \text{for } i \in 0..\text{length}(v1) - 1 \\ \quad t1_i \leftarrow \dfrac{\left[\left(a1^T\right)^{\langle 1 \rangle}\right]_i - \left[\left(b1^T\right)^{\langle 1 \rangle}\right]_i}{s1_i} \\ t1 \end{array} \right.$$

$t1 =$

	0
0	1.144
1	0.707
2	-0.165
3	-1.064
4	-0.318
5	-0.538
6	-1.522
7	-1.472
8	-1.173
9	-0.287

P-value P(|T|>|t|):

$$P1 := \left| \begin{array}{l} \text{for } i \in 0..\text{length}(v1) - 1 \\ \quad p1_i \leftarrow 2 \cdot \left(1 - pt\left(\left|t1_i\right|, v1_i\right)\right) \\ p1 \end{array} \right.$$

$P1 =$

	0
0	0.296
1	0.506
2	0.874
3	0.328
4	0.761
5	0.602
6	0.159
7	0.172
8	0.268
9	0.78

α/2 percentage point:

$$T1 := \left| \begin{array}{l} \text{for } i \in 0..\text{length}(\nu 1) - 1 \\ \quad T1_i \leftarrow \left| qt\left(\frac{\alpha}{2}, \nu 1_i\right)\right| \\ T1 \end{array} \right.$$

$T1 =$

	0
0	3.521
1	3.521
2	3.521
3	3.521
4	3.521
5	3.038
6	3.038
7	3.038
8	3.038
9	3.038

Reject the null hypothesis if |t| > T.

$$Del1 := \left| \begin{array}{l} \text{for } i \in 0..\text{length}(\nu 1) - 1 \\ \quad Del1_i \leftarrow |t1_i| - T1_i \\ Del1 \end{array} \right.$$

Result1 := for $i \in 0 .. length(v1) - 1$

$Result1_i \leftarrow$ "Significant Difference" if $Del1_i > 0$

$Result1_i \leftarrow$ "No Significant Difference" otherwise

Result1

$augment\left[\left(a1^{T}\right)^{\langle 0 \rangle}, Result1\right] =$

	0	1
0	5	"No Significant Difference"
1	10	"No Significant Difference"
2	14.8	"No Significant Difference"
3	20	"No Significant Difference"
4	25	"No Significant Difference"
5	44.3	"No Significant Difference"
6	49.3	"No Significant Difference"
7	54.5	"No Significant Difference"
8	59.3	"No Significant Difference"
9	64.3	"No Significant Difference"

Table D.1. Comparison of 2nd mode shapes at various temperature ranges using a t-test analysis.

Temp. Range (°C)			Sensor location from the west abutment (m)									
			5.0	10.0	14.8	20.0	25.0	44.3	49.3	54.5	59.3	64.3
30 to 40	South Side	t-value	0.03	-1.2	-0.91	-1.04	-1.25	-1.3	-1.96	-1.97	-1.73	-1
		P-value	0.97	0.26	0.38	0.32	0.24	0.21	0.08	0.07	0.11	0.32
		DOF	9	9	9	9	9	11	11	11	11	11
4 to 7	North Side	t-value	-2.36	-2.41	-3.09	-3.06	-1.76	-7.5	-7.4	-6.3	-6.25	-4.7
		P-value	0.03	0.026	**0.006**	**0.006**	0.09	**0**	**0**	**0**	**0**	**0**
		DOF	18	18	18	18	18	12	12	12	12	12
-9 to -7	North Side	t-value	-0.33	1.37	0.79	N/A	0.71	-1.5	N/A	-2.1	-3.24	-0.39
		P-value	0.74	0.18	0.44	N/A	0.49	0.16	N/A	0.058	**0.007**	0.7
		DOF	20	20	20	N/A	20	12	N/A	12	12	12
	South Side	t-value	-0.65	-1.92	-1.87	N/A	-1.37	-1.08	N/A	-1.17	-1.03	-1.03
		P-value	0.53	0.08	0.09	N/A	0.2	0.3	N/A	0.26	0.32	0.32
		DOF	11	11	11	N/A	11	12	N/A	12	12	12
-12 to -5	North Side	t-value	0.2	0.69	-0.26	N/A	-0.69	0.04	N/A	0.78	1.43	0.17
		P-value	0.84	0.5	0.8	N/A	0.5	0.97	N/A	0.45	0.18	0.87
		DOF	19	19	19	N/A	19	10	N/A	10	10	10
	South Side	t-value	-0.36	-1.62	-1.78	N/A	-2.06	-2.87	N/A	-0.15	0.19	-0.1
		P-value	0.72	0.13	0.1	N/A	0.06	**0.01**	N/A	0.88	0.84	0.91
		DOF	10	10	10	N/A	10	12	N/A	12	12	12

DOF=Degrees of freedom.

P-values in bold denote statistical significance at the 95% level.

Table D.2. Comparison of 3rd mode shapes at various temperature ranges using a t-test analysis.

Temp. Range (°C)			Sensor location from the west abutment (m)									
			5.0	10.0	14.8	20.0	25.0	44.3	49.3	54.5	59.3	64.3
30 to 40	South Side	t-value	1.12	-0.74	-0.46	-1.26	-0.99	0.96	0.2	0.05	0.26	0.13
		P-value	0.3	0.48	0.66	0.25	0.36	0.35	0.83	0.96	0.8	0.9
		DOF	7	7	7	7	7	13	13	13	13	13
4 to 7	North Side	t-value	3.2	3.4	3.6	4.4	3.2	-6.34	-11.1	-8.65	-7.3	-6.2
		P-value	**0.006**	**0.004**	**0.002**	**0.001**	**0.005**	**0**	**0**	**0**	**0**	**0**
		DOF	15	15	15	15	15	14	14	14	14	14
-9 to -7	North Side	t-value	-0.01	-1.21	-0.93	N/A	-1.36	1.31	N/A	2.7	2.28	0.74
		P-value	0.99	0.2	0.37	N/A	0.2	0.21	N/A	0.02	0.04	0.47
		DOF	14	14	14	N/A	14	13	N/A	13	13	13
	South Side	t-value	0.89	-0.85	-0.22	N/A	0.41	-0.74	N/A	-0.7	-0.84	-1.52
		P-value	0.39	0.41	0.82	N/A	0.69	0.48	N/A	0.5	0.42	0.16
		DOF	11	11	11	N/A	11	9	N/A	9	9	9
-12 to -5	North Side	t-value	-0.3	-1.95	-1.44	N/A	-1.28	-1.66	N/A	-1.85	-2.25	-2.5
		P-value	0.76	0.07	0.17	N/A	0.22	0.12	N/A	0.08	0.04	0.03
		DOF	13	13	13	N/A	13	13	N/A	13	13	13
	South Side	t-value	0.2	-1.4	-0.75	N/A	0.09	-2.96	N/A	-0.67	-0.77	-1.42
		P-value	0.84	0.18	0.47	N/A	0.93	**0.01**	N/A	0.51	0.46	0.18
		DOF	13	13	13	N/A	13	13	N/A	13	13	13

DOF=Degrees of freedom.

P-values in bold denote statistical significance at the 95% level.

APPENDIX E . MODEL CALIBRATION

Comparisons of the first experimental and FE mode shape in temperature ranges of -12°C to -5°C, 4°C to 7°C, and 30°C to 40°C are presented in Figure E.1 and Figure E.2

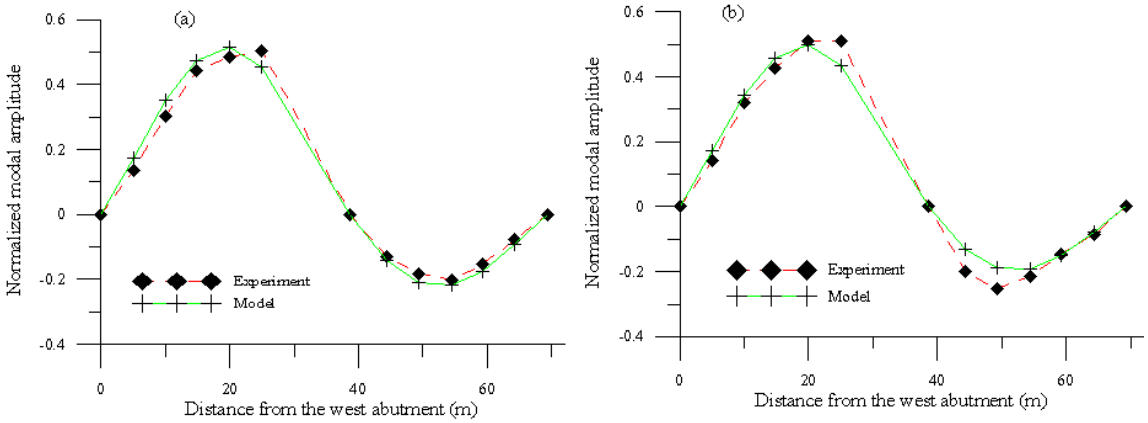

Table E.1. Comparison of measured and numerical fundamental mode shapes for the temperature range of -12°C to -5°C: (a) along the north barrier wall; and (b) along the south barrier wall.

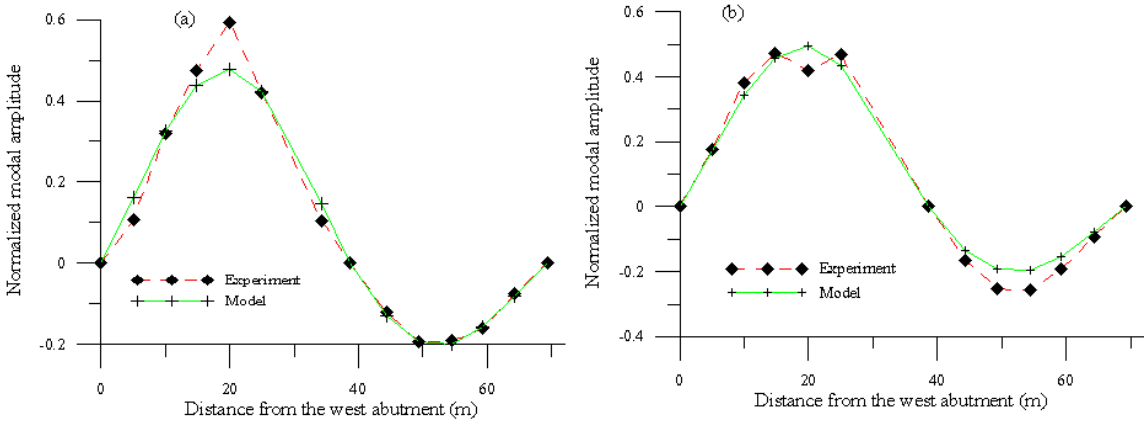

Table E.2. Comparison of measured and numerical fundamental mode shapes for the: (a) temperature range of 4°C to -7°C along the north barrier wall; and (b) temperature range of 30°C to 40°C along the south barrier wall.

APPENDIX F . INFLUENCE OF TEMPERATURE ON MODE SHAPES

Spatial distributions of change in fundamental mode shape over the surface of the deck caused by a decrease in temperature from 20°C to 5°C are shown in Figure F.1. Distributions of changes in fundamental mode shape along three longitudinal lines corresponding to an increase in temperature from 20°C to 35°C, a decrease in temperature from 20°C to 5°C, and a decrease in temperature from 20°C to -25°C are presented in Figure F.2 through F4, respectively.

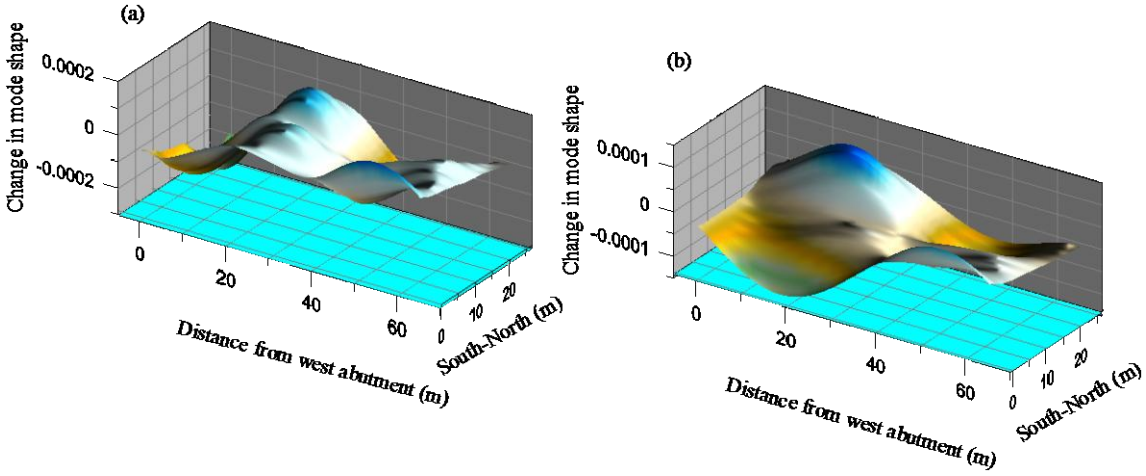

Figure F.1. Distributions of the change in fundamental mode shape over the surface of the deck caused by a decrease in temperature from 20°C to 5°C: (a) using line-by-line normalization; and (b) using surface normalization.

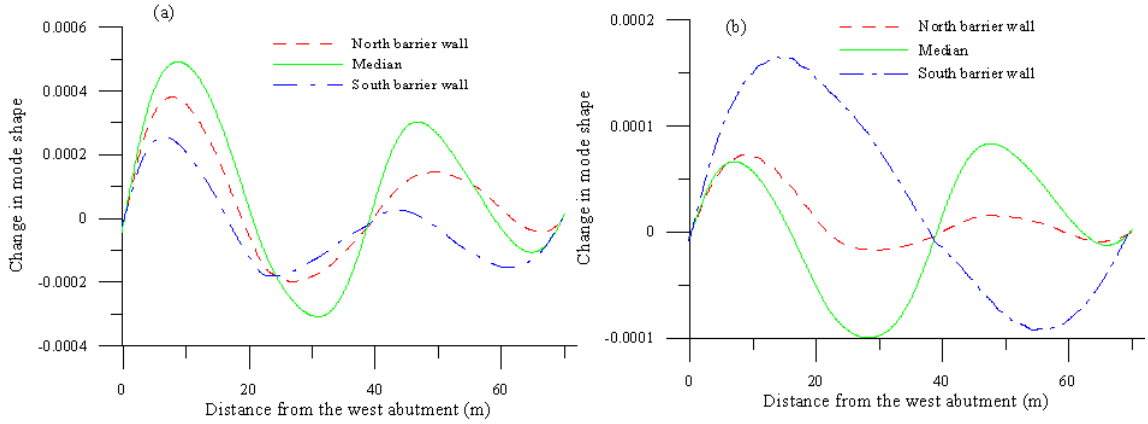

Figure F.2. Distributions of changes in fundamental mode shape along three longitudinal lines, corresponding to an increase in temperature from 20°C to 35°C: (a) using line-by-line normalization; and (b) surface normalization.

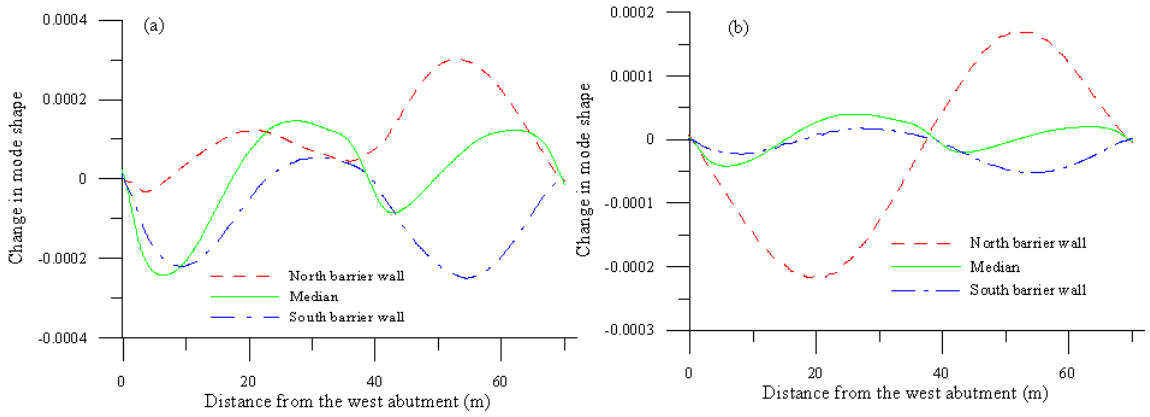

Figure F.3. Distributions of changes in fundamental mode shape along three longitudinal lines, corresponding to a decrease in temperature from 20°C to 5°C: (a) using line-by-line normalization; and (b) surface normalization.

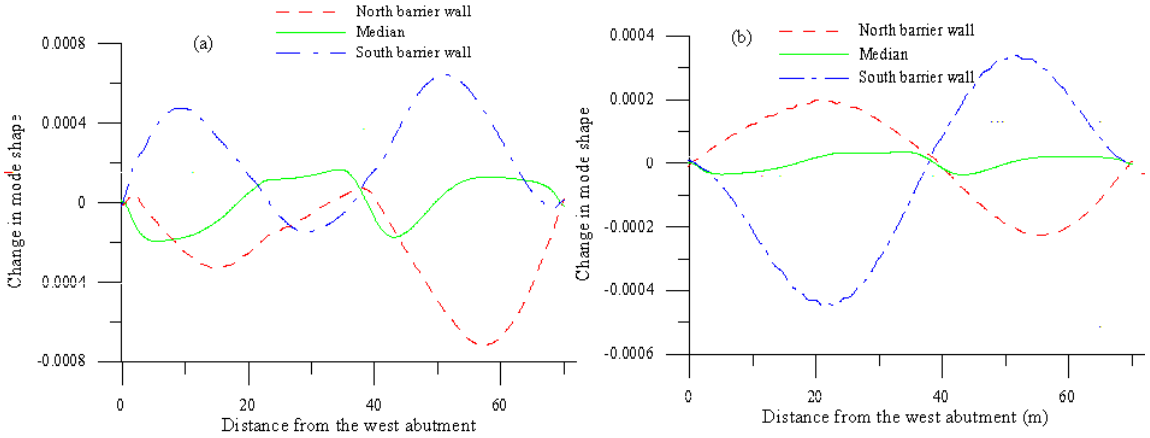

Figure F.4. Distributions of changes in fundamental mode shape along three longitudinal lines, corresponding to a decrease in temperature from 20°C to -10°C: (a) using line-by-line normalization; and (b) surface normalization.

APPENDIX G . DAMAGE-INDUCED CHANGES IN FUNDAMENTAL MODE SHAPES

Spatial distributions of changes in fundamental mode shape caused by damage states 8, 6, and 1 at an ambient temperature of -25°C are shown in Figure G.1 through Figure G.3. Spatial and three longitudinal line distributions of changes in fundamental mode shape caused by damage states 2, 3, 4, 5, 7, and 9 at an ambient temperature of -20°C are shown in Figure G.4 through Figure G.15.

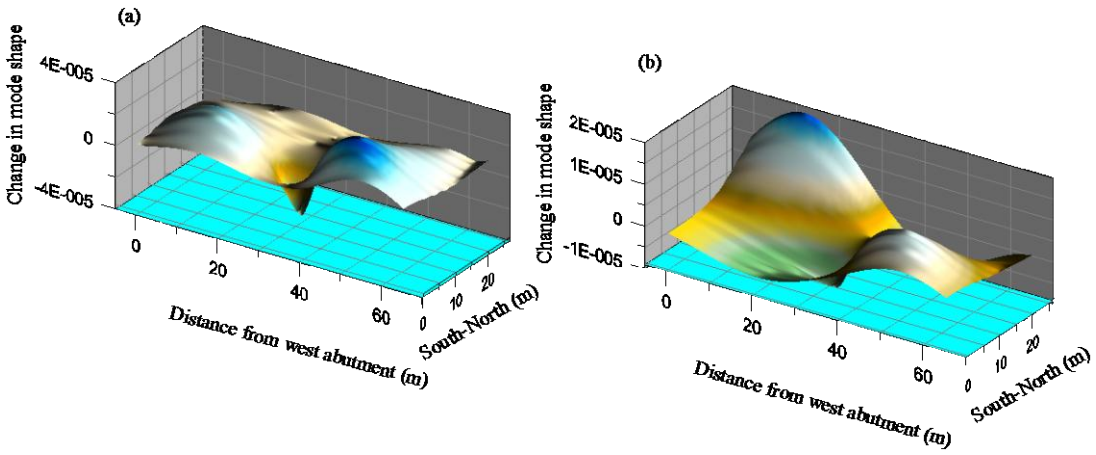

Figure G.1. Spatial distributions of changes in fundamental mode shape caused by damage state 8 at an ambient temperature of -25°C: (a) calculated using line-by-line normalization; and (b) surface normalization.

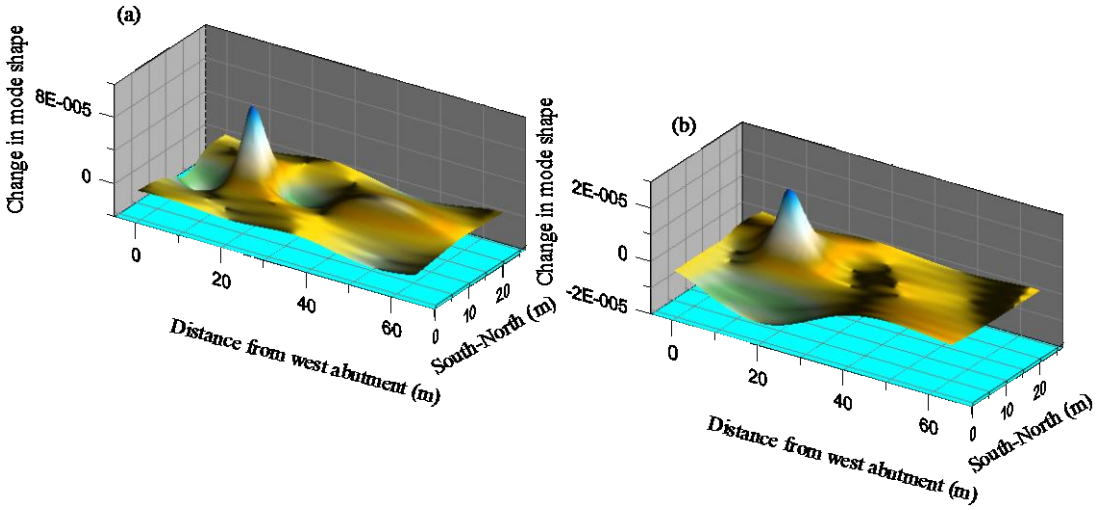

Figure G.2. Spatial distributions of changes in fundamental mode shape caused by damage state 6 at an ambient temperature of -25°C: (a) calculated using line-by-line normalization; and (b) surface normalization.

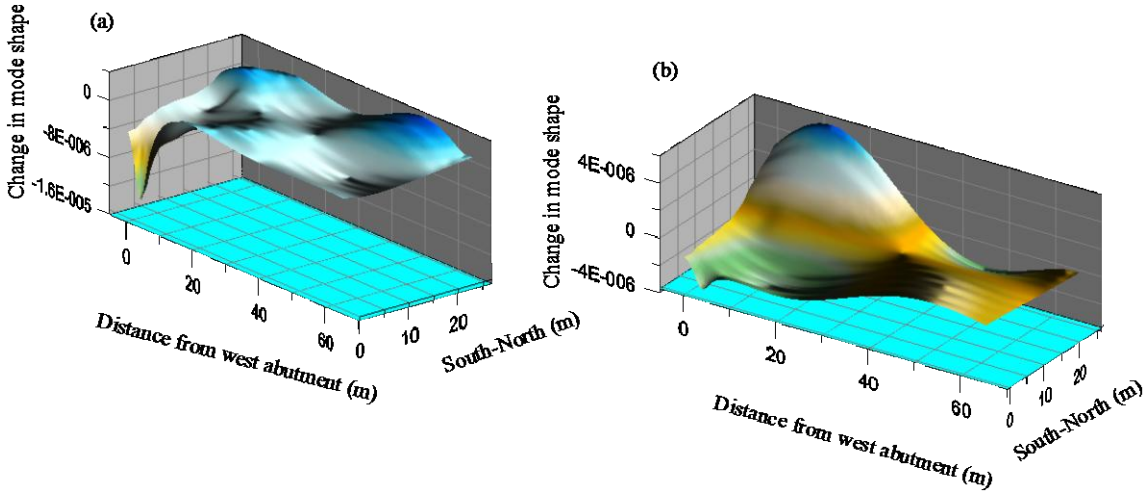

Figure G.3. Spatial distributions of changes in fundamental mode shape caused by damage state 1 at an ambient temperature of -25°C: (a) calculated using line-by-line normalization; and (b) surface normalization.

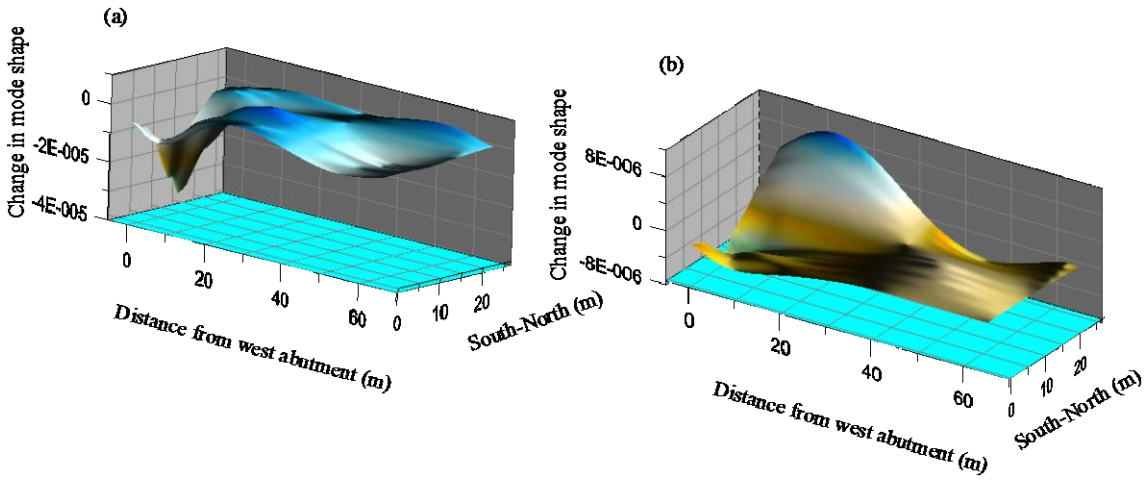

Figure G.4. Spatial distributions of changes in fundamental mode shape caused by damage state 2 at an ambient temperature of 20°C: (a) calculated using line-by-line normalization; and (b) surface normalization.

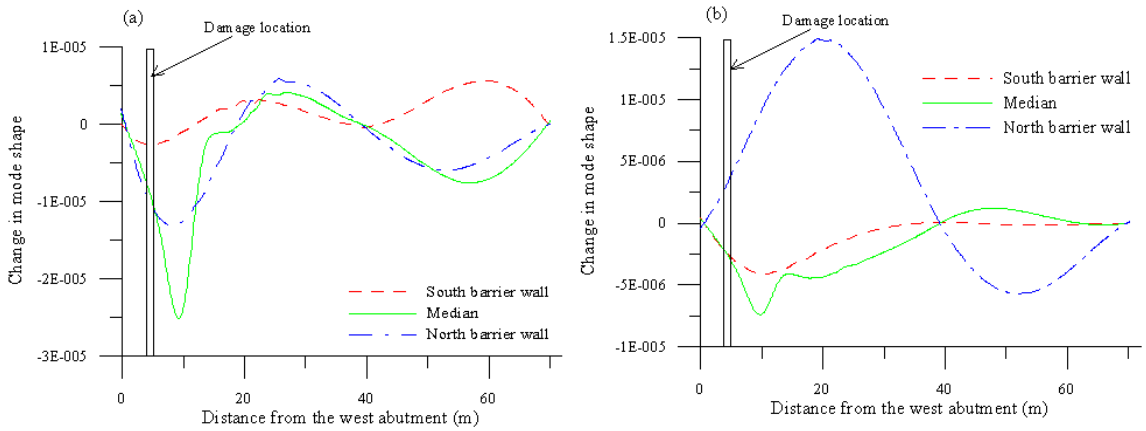

Figure G.5. Distributions of changes in fundamental mode shape caused by damage state 2 at an ambient temperature of 20°C along selected longitudinal lines: (a) calculated using line-by-line normalization; and (b) surface normalization.

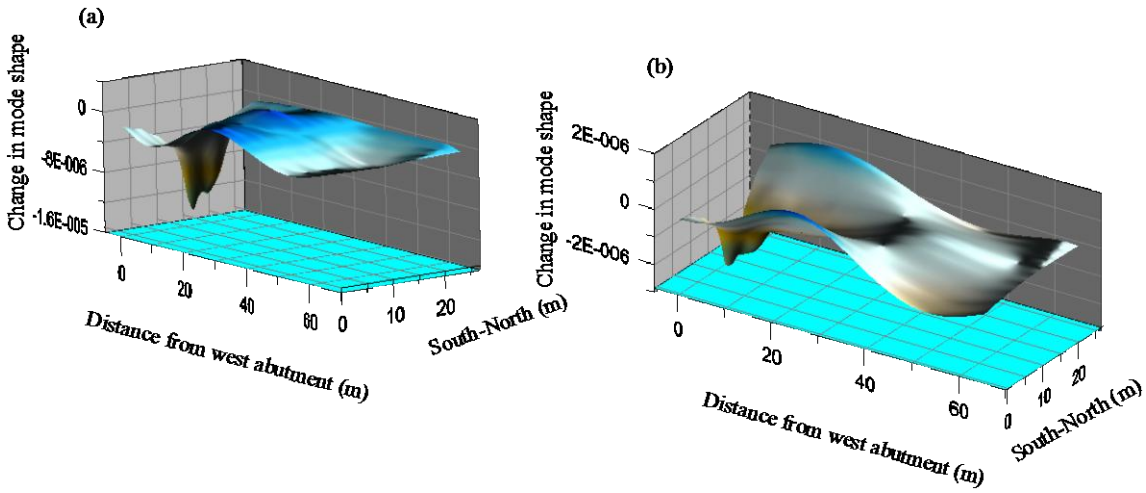

Figure G.6. Spatial distributions of changes in fundamental mode shape caused by damage state 3 at an ambient temperature of 20°C: (a) calculated using line-by-line normalization; and (b) surface normalization.

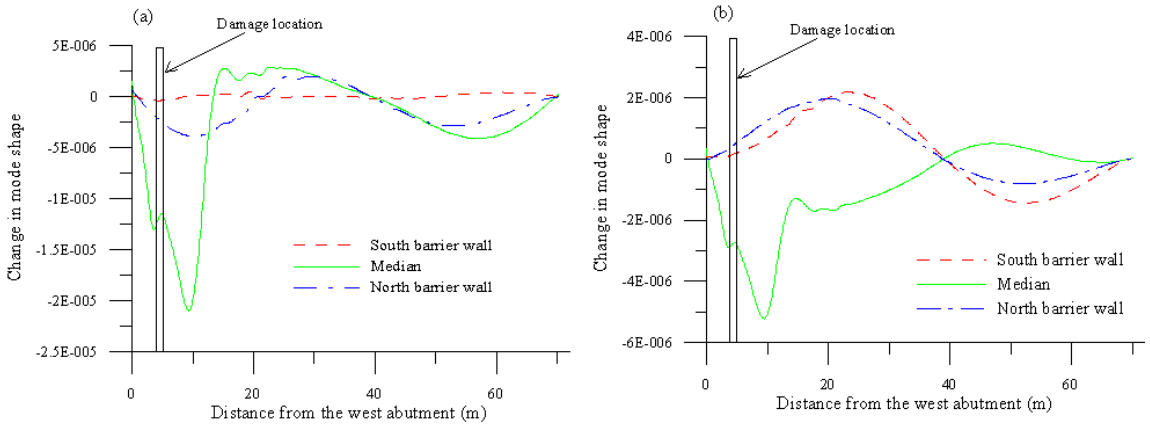

Figure G.7. Distributions of changes in fundamental mode shape caused by damage state 3 at an ambient temperature of 20°C along selected longitudinal lines: (a) calculated using line-by-line normalization; and (b) surface normalization.

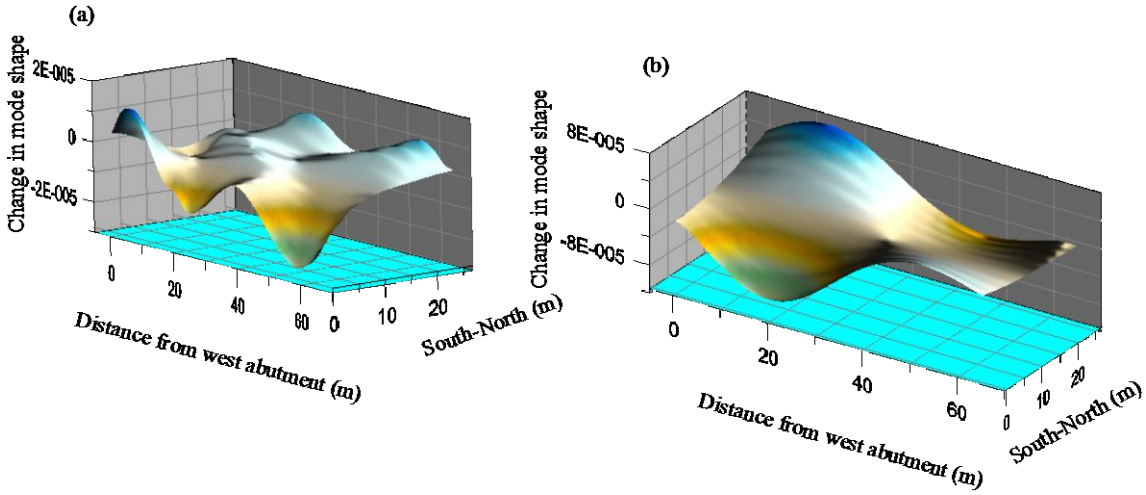

Figure G.8. Spatial distributions of changes in fundamental mode shape caused by damage state 4 at an ambient temperature of 20°C: (a) calculated using line-by-line normalization; and (b) surface normalization.

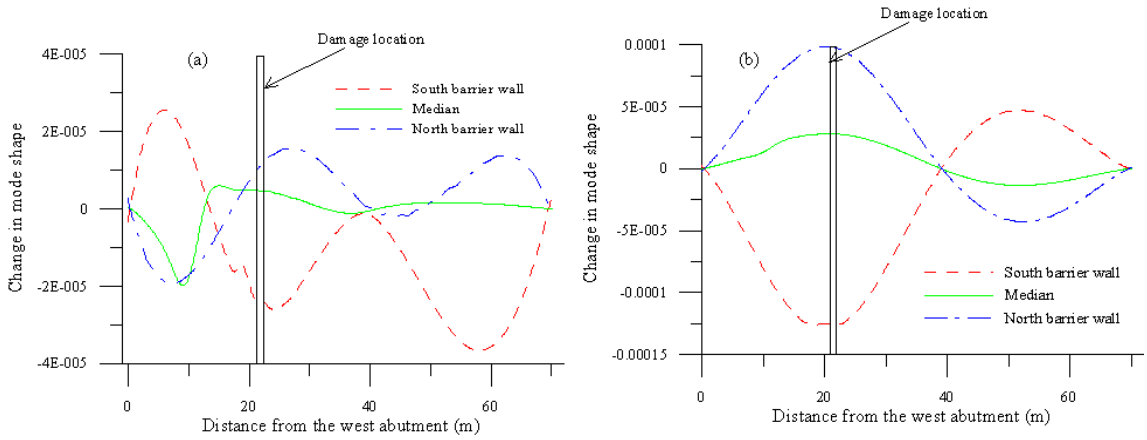

Figure G.9. Distributions of changes in fundamental mode shape caused by damage state 4 at an ambient temperature of 20°C along selected longitudinal lines: (a) calculated using line-by-line normalization; and (b) surface normalization.

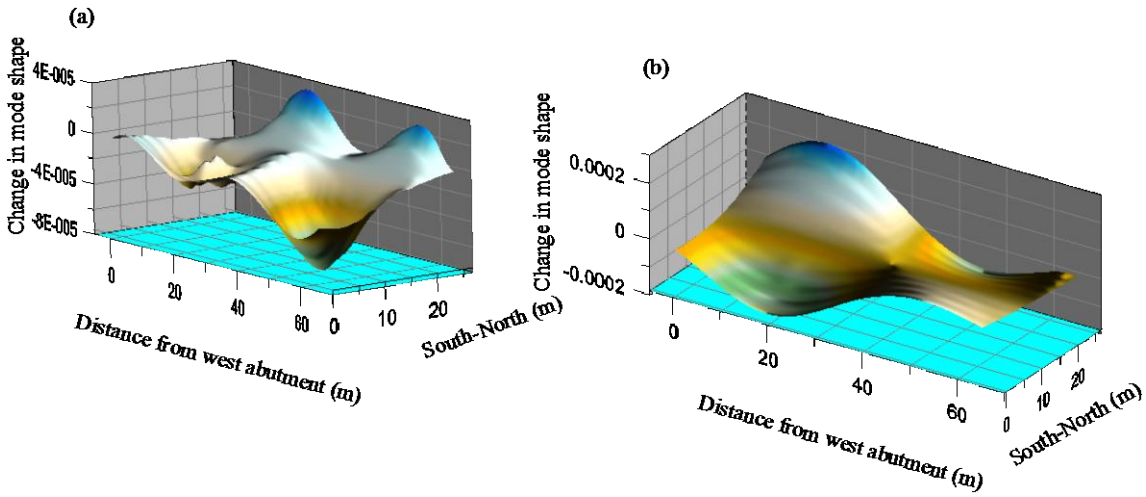

Figure G.10. Spatial distributions of changes in fundamental mode shape caused by damage state 5 at an ambient temperature of 20°C: (a) calculated using line-by-line normalization; and (b) surface normalization.

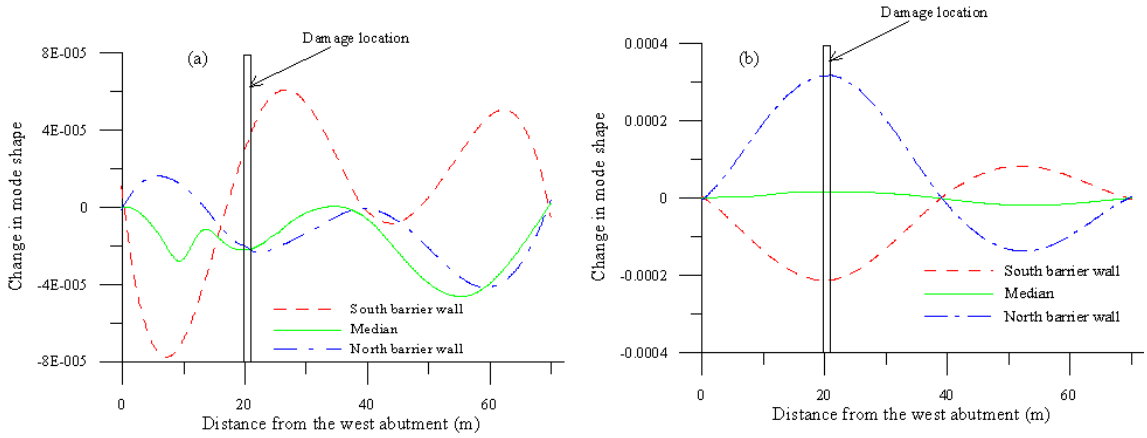

Figure G.11. Distributions of changes in fundamental mode shape caused by damage state 5 at an ambient temperature of 20°C along selected longitudinal lines: (a) calculated using line-by-line normalization; and (b) surface normalization.

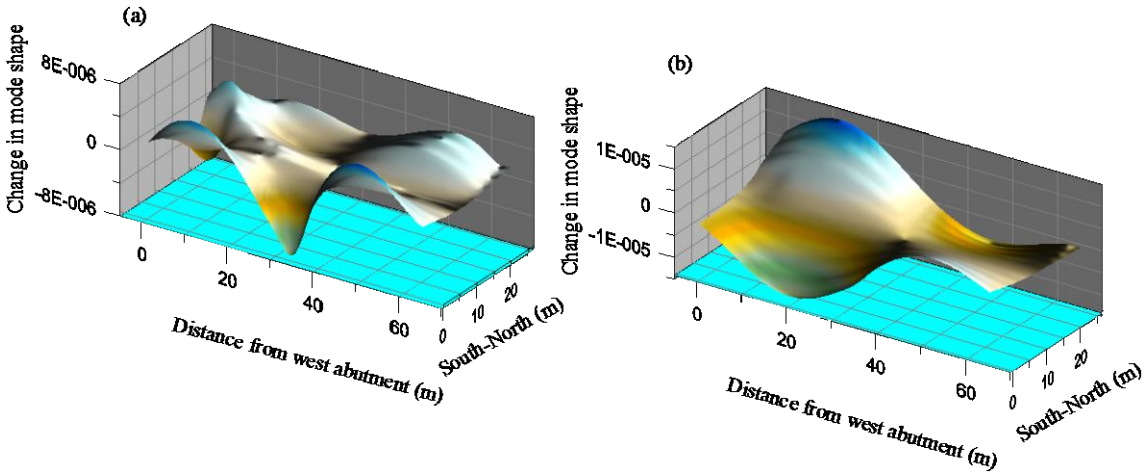

Figure G.12. Spatial distributions of changes in fundamental mode shape caused by damage state 7 at an ambient temperature of 20°C: (a) calculated using line-by-line normalization; and (b) surface normalization.

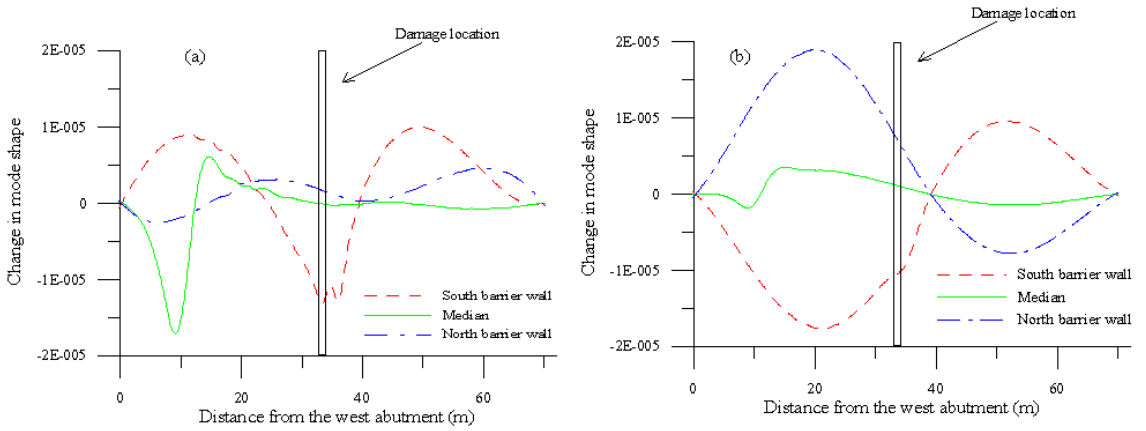

Figure G.13. Distributions of changes in fundamental mode shape caused by damage state 7 at an ambient temperature of 20°C along selected longitudinal lines: (a) calculated using line-by-line normalization; and (b) surface normalization.

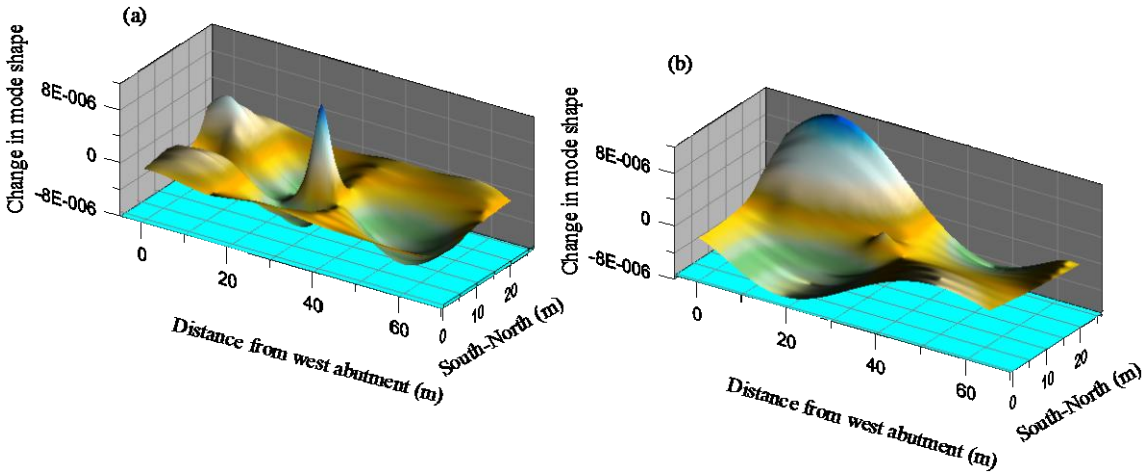

Figure G.14. Spatial distributions of changes in fundamental mode shape caused by damage state 9 at an ambient temperature of 20°C: (a) calculated using line-by-line normalization; and (b) surface normalization.

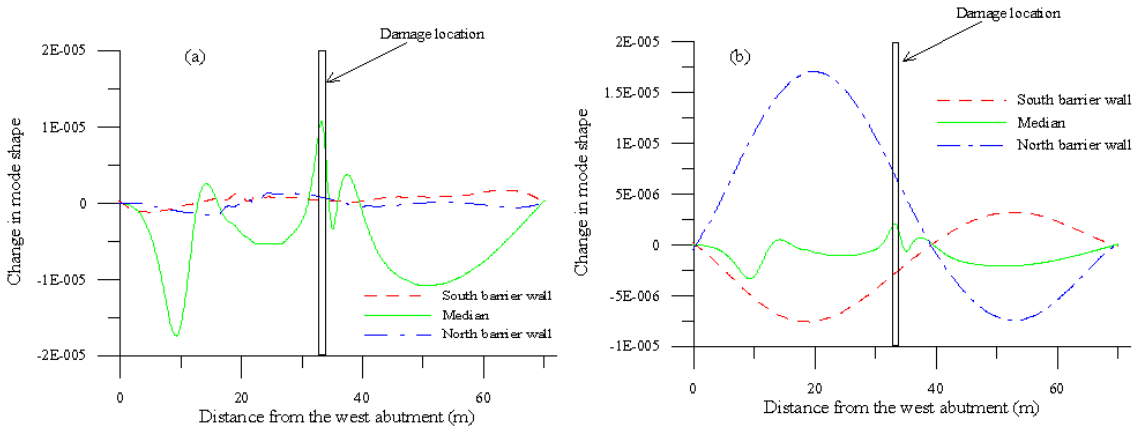

Figure G.15. Distributions of changes in fundamental mode shape caused by damage state 9 at an ambient temperature of 20°C along selected longitudinal lines: (a) calculated using line-by-line normalization; and (b) surface normalization.